Self-assembled structures with crystalline order in aqueous block polymer systems: Understanding nanoscale structure and material processing to achieve desirable properties.

Submitted in partial fulfillment of the requirements for

the degree of

Doctor of Philosophy

In

Chemical Engineering

Connor S. Valentine

B.S., Chemical Engineering, University of California at Santa Barbara

Carnegie Mellon University

Pittsburgh, PA

March 2022

Acknowledgements

My greatest appreciation goes to my wife, Jessica Valentine. She has supported my goal of achieving this degree since I signed the commitment letter while we still lived in Santa Barbara. Without her unwavering support I would not have had the staying power required to finish this program.

I would like to thank my advisor, Professor Lynn Walker. It is rare to find a mentor who is not only willing, but able to teach with patience. She has consistently set appropriate milestones to illuminate the path ahead. I have become proficient at approaching problems without known answers because of her teaching. In this research group I have been allowed the freedom to approach problems creatively, and the responsibility to make independent decisions in pursuit of unique ideas.

I would like to thank my parents, who have always supported my appetite for puzzles, science, logic, and debate – in hindsight, their patience for my bullheaded arguments is inspirational. Their sacrifice and long hours to create a stable life for me and my siblings allowed me the opportunity to work hard and achieve everything I have to this day.

I now thank the scientists, collaborators, and mentors who made much of the work in this thesis possible. Professor Mahesh Mahanthappa and Dr. Ashish Jayaraman at the University of Minnesota acted as open

collaborators for the Small Angle X-ray Scattering measurements in this work. In the early days of our collaboration, they provided open access to pre-print SAXS data. This initiated my qualifier exam work and resulted in a published manuscript in the Korea-Australia Rheology Journal. The Mahanthappa group invited us to join their team on several trips to Argonne National Lab, where I was able to learn a great deal about Small Angle Xray Scattering in a way that only hands on training can provide. Dr. Dylan Steer and the Mahanthappa group recorded SAXS measurements on our behalf during the COVID-19 quarantine. I thank all my graduate student friends at CMU who have help repair equipment, share ideas, and collaborate over measurements. It was a pleasure to go on this journey together.

I gratefully acknowledge the funding that has enabled my research over the past 4 years. I have received the honor of the Exxon Mobil Graduate Fellowship in Chemical Engineering, the PPG Fellowship in Chemical Engineering, in addition to the Dowd Fellows Program at CMU which is awarded to early-stage research with the potential to grow exponential and solve meaningful global problems. Finally, I want to thank my committee members - Anne Robinson, Bob Tilton, and Gordon Rule for their intellectual guidance through the journey to writing this thesis. I could not have completed this work without them.

Abstract

Block polymers dispersed into a solvent that prefers one block strongly over the other blocks can spontaneously arrange into nanoscale structures, such as spherical or cylindrical micelles. These nanoscale structures can pack into three dimensional crystalline grains. The final properties of a material with crystalline nanostructure are dependent on many factors including the thermal and shear history of the sample. Any additional components to the system may change the nanoscale structure which will consequently change the final mechanical properties. In this work a practical understanding of block polymer phases is established, along with useful processing techniques. Widely accessible rheological techniques are used to demonstrate a unique fingerprint between FCC and BCC crystalline phases. We then demonstrate the importance of shear processing by using large amplitude oscillatory shear to accelerate a crystalline order transition to occur within minutes rather than months. The mobility of proteins through the aqueous channels in block polymer crystals is quantified with a semi-autonomous Fluorescence Recovery After Photobleaching microscope built for this work. The outcome of this work is a set of guiding principles to allow for systematic design of a material with a crystalline block polymer structure.

Table Of Contents

List of Tables

List of Figures

Chapter 1 – Introduction

Block polymer molecules in a solvent that prefers one block over another can self-assemble into structures such as spherical micelles that can further pack and organize into materials with crystalline order. Remarkably, the crystals observed in these polymeric systems show many similarities to the crystals found in metallic systems. The mastery of metallic crystalline structure ushered in great technological achievements that changed the face of our world – from perfect silicone crystals for semiconductor fabrication to single crystal turbine blades with unparalleled fuel efficiency. As with metallic crystals, the useful mechanical and material properties in polymeric crystals arise from the nanoscale structures that compose the material. Unlike atomic crystals in metals, there are hierarchical length scales and forces controlling the formation and mechanical properties of polymeric crystals. Understanding the link between nanoscale structure and mechanical properties in polymeric crystals is a formidable task with much progress left to be made.

There have been drastic achievements over the past 40 years to achieve predictive theories that link the chemical composition of an individual polymer chain to the crystalline phases formed by those individual chains. However, there exists a nearly infinite design space for polymeric chains even when only considering the variables of chain length, composition of the chain, and chain structure. The accuracy of modern

predictive theories begins to fail when complexities are added to the system. The resulting materials are soft due to the weaker forces that drive assembly in comparison to metallic crystals. This makes possible a variety of processing techniques such as shear processing, thermal annealing, and extrusion commonly used with soft materials to achieve desirable properties. Engineers will need to understand the forces driving the self-assembly of block polymer chains into hierarchical structures. However, it is inevitable that deviations from predictive theories will be encountered during formulation and scale up attempts.

In this work we introduce a systematic approach to the design of materials with self-assembled crystalline structure. It is important that the engineer expects deviations from predicted results, embracing experimental techniques that quantify the nanoscale structure as thoroughly as possible.

1.1 Objectives and Goals

The goal of this work is to characterize macroscopic properties of lyotropic liquid crystals in diblock and triblock copolymer dispersions and to provide a comprehensive method to better characterize new materials, thermal history effects, and to guide processing to achieve desirable properties in the final material. Systems with PEO blocks that assemble in the aqueous phase are the primary focus. In Chapter 2, the limitations of predictive theories for block polymer crystalline phase formation are explored. These examples demonstrate the utility of existing literature data,

which should be leveraged at the start of any material design effort. Techniques such as rheological characterization and small angle scattering are used to map the crystalline phase space of several block polymer systems. This base knowledge is then used in Chapter 3 to demonstrate how rheological temperature and frequency sweeps can be used to successfully distinguish Face Centered Cubic and Body Centered Cubic crystalline phases in a diblock polymer system. In chapter 4, we demonstrate that oscillatory shear processing can accelerate phase transitions in block polymer systems. A phase transition that normally occurs on the timespan of months is successfully accelerated to occur within minutes. Processing techniques will be essential to many industrial and academic use cases where control of the nanoscale crystalline structure is crucial. In Chapters 5 and 6, our goal is to achieve a crystalline material with aqueous pockets tailored to the size of proteins. We hypothesized that the macromolecular crowding and confinement inside of the crystalline phases would protect proteins from thermal denaturation. In Chapter 5 we use the comprehensive approach to material design developed in Chapters 2-4 to successfully plan and execute a set of experiments to quantify the mobility of proteins throughout cubic block polymer crystalline networks. In Chapter 6, the systems with the most drastic reduction in protein mobility are tested for enhanced protection from denaturation. While we do not measure any quantifiable protection from thermal denaturation, we do observe a lack of protein aggregation.

1.2 Novelty of the Work

The breadth of existing literature data is an invaluable resource when developing formulations around self-assembled liquid crystalline lattices. However, complications arise from the addition of other components during formulations attempts. Predictive theories and models are useful when working with simple block polymer systems with a neat solvent. However, deviation from simple compositions and solvents is inevitable during attempts to build formulated materials centered around a self-assembled crystalline lattice. It is crucial that engineers and scientists understand how to determine the impact of these additional components via accessible techniques.

Aqueous block polymer crystalline lattices can be designed with aqueous spaces of varying size, with tunable polymer brush density surrounding these aqueous environments. In this work we demonstrate a set of guiding principles, new techniques, and protocols that can be used to leverage the unique qualities of the aqueous structures in block polymer materials. Understanding the effect of thermal and shear processing on the mechanical properties of block copolymer lyotropic liquid crystals is crucial to the application of these materials in academia and industry. The methods in this work can be used to rapidly probe mechanical properties, investigate the impact of processing, and gain structural insights in new systems before delegating resources to small angle scattering experiments. The tools

introduced and expanded in this work can be used by formulators to understand and leverage the nanoscale structures in block polymer crystalline lattices to achieve desirable material properties in this unique class of materials.

Chapter 2 Crystalline nanostructures in aqueous block polymer systems: characterization and processing

Block polymer molecules in a solvent that prefers one block over another can self-assemble into nanostructured soft materials with rich phase behavior.[1,2] The amphiphilic nature of a block polymer molecule drives assembly of micelles, where the insoluble blocks aggregate and form a core to minimize exposure to the solvent.[3] At sufficiently high concentrations, the self-assembled micelles begin to pack into liquid crystalline lattices. Included is a brief review of phase behavior of linear diblock (AB) and triblock (ABA) block polymers in solvents with selectivity for one of the blocks. Typical phase behavior for diblock and triblock polymers in a solvent which is selective to one of the blocks is outlined with an emphasis on the flow behavior of these phases. The primary focus is on systems where the block polymers are either dissolved in purified water or an organic solvent.

Formulations with multiple solvents, solvent additives such as salt, pH changes, or blends of block polymers will complicate the application of existing theoretical predictions. The addition of homopolymers, buffer salts, colloidal particles, small molecule drugs, and pH changes can lead to phase behavior that deviates substantially from predictions in the original two component block polymer and solvent system. The guiding principles available in literature may not be enough to predict the phase behavior with sufficient accuracy for a desired application. When exploring new

formulations, it is therefore often necessary to characterize phase behavior as a function of the formulation parameters.

An approach to characterize phase behavior during formulation attempts using Pluronic triblock polymers is demonstrated. Pluronic® triblock polymers with the formula PEO_m-PPO_n-PEO_m, (also known as Synperonic® or Polaxomer) have been extensively studied over the past 30 years due to their commercial availability and widespread use in cosmetics, pharmaceutical formulations, protein stabilization, cell culture formulations, and nanoscale templating materials.[4–7] Rheological studies are used to understand the concentration dependence of the order to disorder transitions in three Pluronic systems (P123, F127, and F87) where bicarbonate buffer at pH = 9 is used as the solvent. Small angle X-ray scattering is then used to accurately determine the crystalline phase and unit cell size in samples demonstrating favorable rheological properties.

2.1 Self-assembly in Diblock and Triblock polymer systems

Block polymer molecules in a solvent that prefers one block over another can self-assemble into nanostructured soft materials with rich phase behavior.[1] The amphiphilic nature of a diblock polymer molecule drives assembly of micelles in both the melt state and solvent-swollen state. For a given polymer architecture, concentration, temperature, and solvent quality, micelles will form crystalline lattices known as lyotropic liquid crystals (LLCs).[1,8] A single system can have multiple LLC packings accessible via concentration or temperature changes. Commonly seen phases include body-centered cubic (BCC), face-centered cubic (FCC), hexagonally close-packed spheres (HCP), hexagonally close-packed cylinders (H_I), and lamellar phases (L_α).[9] The phases formed are sometimes termed gels based on macroscopic observation even though the macroscopic properties arise from the packing of self-assembled structures into crystalline lattices as opposed to cross-linkages between polymer chains in a conventional gel.

Solvent selectivity for at least one of the polymer blocks often varies with temperature, broadening the accessible number and types of phases.[9] The thermo-reversible order-order transitions (OOTs) and order-disorder transitions (ODTs) between phases can be located using a number of structural (small angle scattering, birefringence) and macroscopic (jar inversion tests, rheological) techniques.[6,10] The mechanical properties, nanoscale crystalline structure, and phase transition boundaries are

dependent on sample history. For example, the thermal history of a sample can shift ODTs and OOTs and initiate metastable phases which are kinetically trapped, preventing a transition back to thermodynamic equilibrium.[11,12] Hysteresis, or a dependence of structure on thermal sample history, near OOTs has been observed in several block polymer systems.[11–13] The techniques outlined above can be used to better characterize new materials, thermal history effects, and to guide processing.

Block polymers can form incredibly complex structures, with new possibilities in various material classes still being uncovered. Complex low symmetry crystalline morphologies, including the Frank-Kasper (FK) σ phase, were described by Frank and Kasper almost 60 years ago.[14] FK phases are tetrahedrally closest-packed phases containing combinations of 12-,14-,15-, and 16-coordinate lattice sites.[14] FK phases have been studied in metallic systems and have more recently been observed in soft materials. The FK A15 phase was first seen in ionic surfactants and lipidic LLCs almost 30 years ago. Since then, A15 and σ phases have been found in wedge-shaped dendrons[15], linear diblocks [16], multiblock polymers [17], and giant shape amphiphiles.[18] In fact, these phases are more prevalent than initially expected and likely to appear in many block polymer and surfactant solutions.

2.2 Limitations Predicting Phase Behavior

Prediction of phase behavior in block polymer systems is complicated by even small modifications to system architecture. Incorporation/decoration of block polymers with structure directing blocks (increased hydrogen bonding, charged species) can have a drastic effect on self-assembly in these systems. Designing systems with decorated architectures is challenging because the understanding and accuracy of the Fluory-Huggins parameter degrades rapidly with system complexity. The theoretical definition of the Flory-Huggins parameter, χ, provides a straightforward definition of enthalpic consequences arising from interactions between like (A-A) and unlike (A-B) blocks. However, χ breaks down into χ_{eff} with only small deviations from simple A-B blends. To make matters worse the χ_{eff} measured in experiments is capturing a mixture of enthalpic and entropic effects and the interpretation of these values is muddled with poorly defined and understood non idealities.[19] Even chemically identical systems, but with different polymer block architecture, will demonstrate different values of χ_{eff}. The effects of χ_{eff}, polymer chemistry, architecture, and any sort of structure directing moieties is poorly understood except in the most basic systems. A clear example of this is the surprising discovery that the addition and subsequent deprotonation of a single end group in a PS-*b*-EO system transforms the lamellar phase into hexagonally packed cylinders.[19,20]

Bates and Bates go so far as to say the “mean field notion of χ is simply incapable of capturing the actual influence exerted by miniscule concentrations of structure-directing moieties”.[19] Modern advances in computational methods have brought us close to the realization of simulated phase behavior of block polymers with atomistic detail, providing hope for accurate prediction and effective application of χ to design new systems.[19] The phase behavior of block polymer melts and solutions is often assumed to be measured at equilibrium conditions. However recent studies of linear multiblock polymers and even simple diblock polymers have emphasized that non-equilibrium states are prevalent and potentially useful.[19]

In summary, experimental methods will be crucial to test and inform new predictive theories and models. Processing (e.g., thermal annealing, shear) of these systems will be necessary to trap non-equilibrium states and optimize useful macroscopic properties. Predictive theories and models are useful when working with simple block polymer systems with a neat solvent. However, deviation from simple compositions and solvents is inevitable as scientists attempt to build formulated materials centered around a self-assembled crystalline lattice. The addition of homopolymers, buffer salts, colloidal particles, small molecule drugs, and pH changes can lead to phase behavior that deviates substantially from predictions in the original binary block polymer and solvent system.

2.3 Methods for Phase Diagram Creation

A few techniques are commonly used to map phase behavior in new block polymer melts and solutions. Due to the tendency of ordered micellar phases to have either an apparent or true yield stress - jar tests, or inversion tests, can be used to estimate ODTs. From here polarized microscopy is often used to find anisotropic birefringent phases such as hexagonally packed cylinders or lamellar sheets. Rheological temperature sweeps at constant concentrations have been applied to study and refine the location of ODTs and OOTs.[12,21–23] For example, Mohan and Bandyopadhyay used small amplitude oscillations during temperature sweeps to construct a phase diagram of Pluronic F108.[24] They used frequency sweeps to identify three regions: a micellar fluid phase coexisting with dissolved unimers at low concentrations and temperature, a “soft solid” phase characterized by a modulus two orders of magnitude above the liquid phase and two orders of magnitude below the crystalline phase, and finally a polycrystalline phase with a storage modulus of 10 kPa.[24] Another paper determined a 0.54 g/cc solution (35 wt%) of Pluronic F108 at 25 °C to be FCC.[25] Unfortunately, this sample does not lie on the phase diagram made by Mohan and Bandyopadhyay and so the results cannot be compared easily. Combinations of the tests listed above are often used to provide regions of interest for SAXS or SANS studies. Regions of coexistence are often not included in these phase diagrams when they are extremely narrow.

2.4 Phase Behavior of PS-*b*-PI diblock polymers

The phase behavior of Polystyrene-PolyIsoprene (PS-*b*-PI) diblocks in selective and neutral solvents have been of particular focus in the literature.[3,26–28] The styrene selective solvents were di-*n*-butyl phthalate (DBP), diethyl phthalate (DEP), and dimethyl phthalate (DMP) in order of slightly to strongly selective.[3] A separate study outlines the phase behavior in a neutral solvent, dioctyl phthalate (DOP).[29] Here the authors use small angle x-ray scattering (SAXS) to assign phases and a combination of SAXS, rheological temperature sweeps, and static birefringence to locate order-disorder transitions (ODTs) and order-order transitions (OOTs). Highly asymmetric diblock polymers formed cubic close-packed structures, while cylindrical and gyroid phases were seen in more symmetric blocks and a lamellar phase in symmetric or nearly symmetric blocks.[1]

2.5 Phase Behavior of PEO-*b*-PPO-*b*-PEO triblocks

Pluronic (Synperonic or Polaxomer) systems (PEO-*b*-PPO-*b*-PEO) have been extensively studied over the past 30 years due to the commercial availability and use in cosmetics, pharmaceutical formulations, protein and cell culture studies, and nanoscale templating materials. Their commercial trade names are a combination of a letter and 2 or 3 numbers depending on the structure. The first letter of their commercial name denotes paste (P), liquid (L), or flakes (F). The last digit is roughly the percentage of ethylene oxide, and the middle number(s) when multiplied by 300 is roughly the molecular weight of the PPO block. It should be noted that the commercially

available samples can have broad block length distributions, in addition to the presence of un-reacted diblock chains, that vary between batches and manufacturers. These systems have characteristic thermo-reversible phase transitions, with a disordered phase often seen at temperatures below the structured gel-like phases. In these systems, it appears there are no ordered phases below MW ~ 2000 g/mol.[1,30] Phases seen include a disordered micellar liquid, hexagonally-packed cylindrical phases, body-centered cubic (BCC), face-centered cubic (FCC), bicontinuous cubic phases, and the reverse of each of these four in addition to a lamellar phase.[1,30] A study by Wanka *et. al.* found that the ratio of PEO to PPO controls the number of phases formed, with a larger ratio resulting in more phases.[1,31] As the molar mass of the PPO block increases the minimum concentration for an ordered phase to form decreases from 60 wt% (MW_{PPO}~1700g/mol) to 20 wt% (MW_{PPO}~4000 g/mol).

A comparison of different triblock structures L62, L64, and P105 in (Figure 2.1, RIGHT)[32] shows the effect of doubling PEO chain length while maintaining a constant PPO group (from a to b), in addition to the effect of roughly doubling the PPO and PEO chain lengths (from b to c). The relative size of the PEO and PPO blocks play a crucial role in the phase behavior. When the EO blocks have a larger apparent volume than the PPO blocks, there is a tendency to form spherical or cylindrical structures. Lamellar structures were found to be favored when the PPO blocks are comparably large to the PEO blocks. Here again the effect of temperature was explained

with the temperature dependence of the solvent selectivity. As temperature is increased, the PPO and PEO blocks become less soluble in water. On the other hand, the PEO-PPO interaction parameter will decrease with temperature.[32] The summation of these effects is a decreased swelling of the PEO blocks at higher temperatures, and thus lower curvature structures are favored.

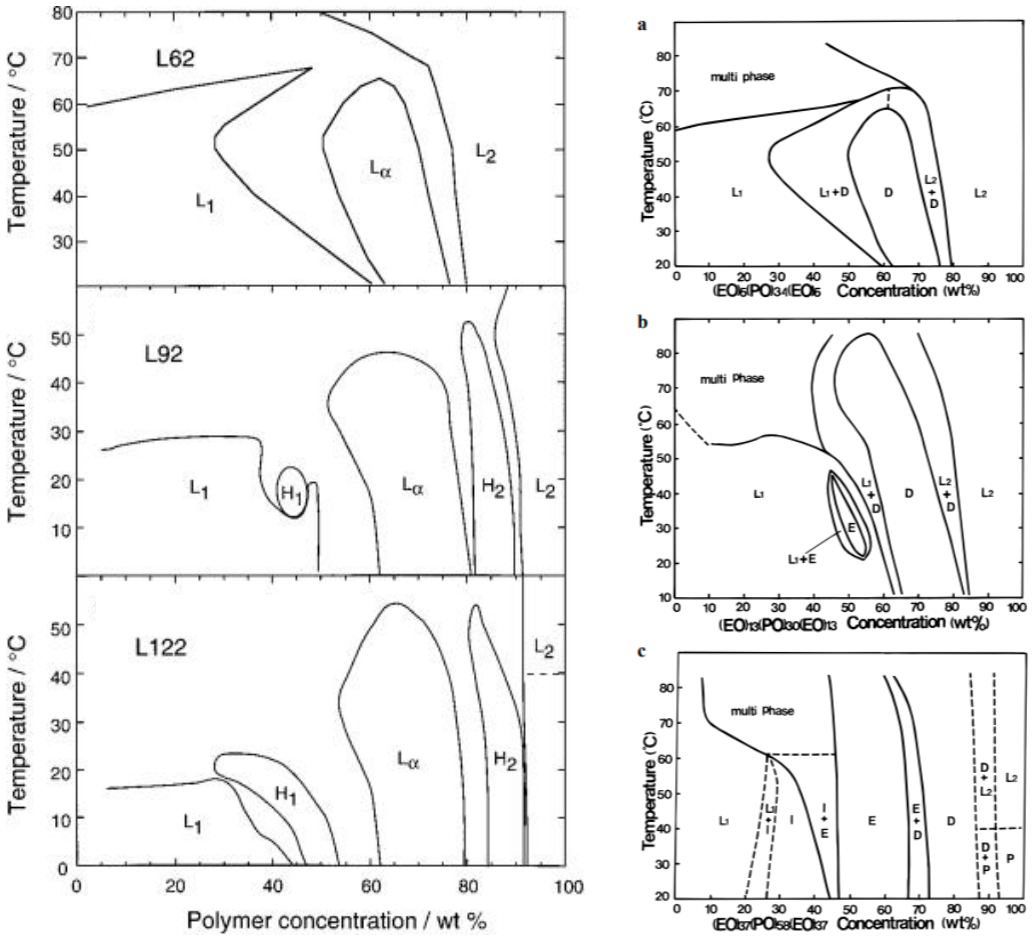

Figure 2.1: (LEFT) Phase behavior of L62 (EO_6-PPO_{34}-EO_6, 2500 g/mol), L92 (EO_8-PPO_{47}-EO_8, 3650 g/mol), and L122 (EO_{11}-PPO_{70}-EO_{11}, 5000 g/mol) in water by SAXS. L_1 = water rich disordered, L_2 = polymer rich disordered, H_1 = normal hex, H_2 = reverse hex, L_α = lamellar phase. Adapted from Svensson *et al.*[33] **(RIGHT)** Phase behavior of **[a]** L62 (EO_6-PPO_{34}-EO_6, 2500 g/mol), **[b]** L64 (EO_{13}-PPO_{30}-EO_{13}, 2900 g/mol), and **[c]** P105 (EO_{37}-PPO_{58}-EO_{37}, 6500 g/mol) in water by SAXS. I = cubic, L_1 = water rich disordered, L_2 = polymer rich disordered, E = hex, D = lamellar, P = paste-like polymer rich phase. Two phase regions are marked and dotted lines indicate uncertainty in phase boundaries. Adapted from Alexandridis *et al.*[34]

2.6 Processing crystalline phases in block polymer systems

Thermal and mechanical (shear) processing can drastically impact the resulting phase behavior and macroscopic properties. Currently the mechanisms behind ODT and OOT rates are not necessarily well understood for drastic thermal transitions. For example, the fusion and fission between spherical and cylindrical micelles does not require chain exchange. Conversely ODTs to spherical micelles are entirely controlled by chain diffusion and exchange.[19] Rapid cooling to ~30°C below the ODT can result in kinetically trapped non-equilibrium states that are stable on the order of months.[12] Parallels can be drawn between the complex Frank-Kasper phases seen in diblock or multiblock polymers and the phase behavior seen in metallic alloys due to processing. These parallels include vitrification upon cooling and diffusionless transitions between phases. Diffusionless transitions (also referred to as Martensitic or militaristic transformations) are characterized by a concerted movement of atoms (or micelles) less than one atomic spacing.[35] The local compositions do not change, only the crystalline structure.

Shear processing of block polymer crystalline lattices is possible due to their low modulus in comparison to metallic systems. Sufficiently high shear flows have been shown to align the liquid crystal structures seen in block polymer solutions.[1,36,37] Combinations of rheology and small angle scattering are well suited to study the influence of processing (shear), temperature effects, and time on block polymer phase behavior and the

resulting macroscopic properties.[13,24,27,38] Mastering the processing of metals and their alloys has produced materials with extremely desirable and useful properties. Similarly, processing of block polymer melts and solutions will be necessary to take full advantage of the accessible equilibrium and nonequilibrium phase behavior and resulting macroscopic properties. The processing in polymeric systems requires orders of magnitude less force, as the modulus is 3-4 orders of magnitude less than their metallic counterparts. However, the shear processing procedures are more complicated as the polymeric materials demonstrate non-linear strain responses. The impact of shear processing on crystalline phases and the resulting macroscopic properties will be explored in depth in Chapter 4.

2.7 Rheology of PEO-*b*-PPO-*b*-PEO aqueous triblock structures

The effect of concentration and temperature on the macroscopic properties of PEO-*b*-PPO-*b*-PEO triblocks is important when processing or using these materials. To demonstrate these trends, rheological data (storage modulus at a single frequency) from the literature are included in Table 2.1. Only systems with existing phase diagrams and rheological temperature sweeps were included (or rheological data at multiple concentrations and temperatures). Data was found for polymers with PEO content between ~30 and ~80% with molecular weights ranging from 5,000 to 15,000 g/mol. These systems have an order-to-disorder transition (ODT) below the structured cubic or hexagonal phases (References in Table 2.1). Here we apply a scaling law (Equations 1-2) that has been applied to

numerous polymeric gels,[39–43] including concentrated block polymer phases.[44]

$$G_e \propto \epsilon^B \tag{1}$$

Where ϵ is the relative distance of the gelling variable (p) from a critical gelation parameter (p_g) which could be temperature, time, or the critical gelation concentration. *B* is the scaling law index, which should be positive,

$$\epsilon = \frac{|p-p_g|}{p_g} \ . \tag{2}$$

Since the critical gelation concentration is difficult to measure in a rheometer, we use the ODT as our critical gelation parameter (Table 2.1). It should be noted that the transition from BCC to FCC is hard to detect from measurement of the elastic component of the complex modulus, G' alone.[28] Consequently the phase in Table 2.1 is often listed as "cubic" in literature unless a direct structural probe was available. This table makes no attempt to distinguish BCC or FCC.

Overall, this scaling law does not provide a good description of the gelation of the polymer samples described in Table 2.1 except for Pluronic F108. The scaling law fails to capture the rapid formation of the cubic phase above the ODT at small ϵ for P103, P123, F127, and F68 (figures 2.2a-2.2d). The scaling law provides an acceptable fit to the hexagonal phase (blue lines, figures 2.2a and 2.2b). You will notice that *B* for the hexagonal phases is negative. *B* is normally positive for this scaling relation because

it is used for gelation of polymer systems above $T_{gel.}$ This is a unique application of the scaling relation to a sample's behavior after an order-order transition. More data is necessary to confirm these trends to other hexagonal packings in other systems, but the application of scaled temperature (ϵ) is an idea worth considering when developing scaling relations for these phase changes.

These trends are included because when applied to the F108 data the scaling law captures the behavior quite nicely. In figure 2.2f all data points are taken at 70°C. The change in ϵ is achieved because T_{ODT} varies with concentration. The scaling law captures the gelation behavior for F108 when ϵ is replaced with wt%. Unfortunately, this was the only system found with enough data to test the scaling law for with respect to concentration. This could suggest that this scaling law only holds for *isothermal* trends in G'. There could be additional explanations that take into effect molecular weight and relative length of PPO to PEO tails, but there is not enough data to make such claims.

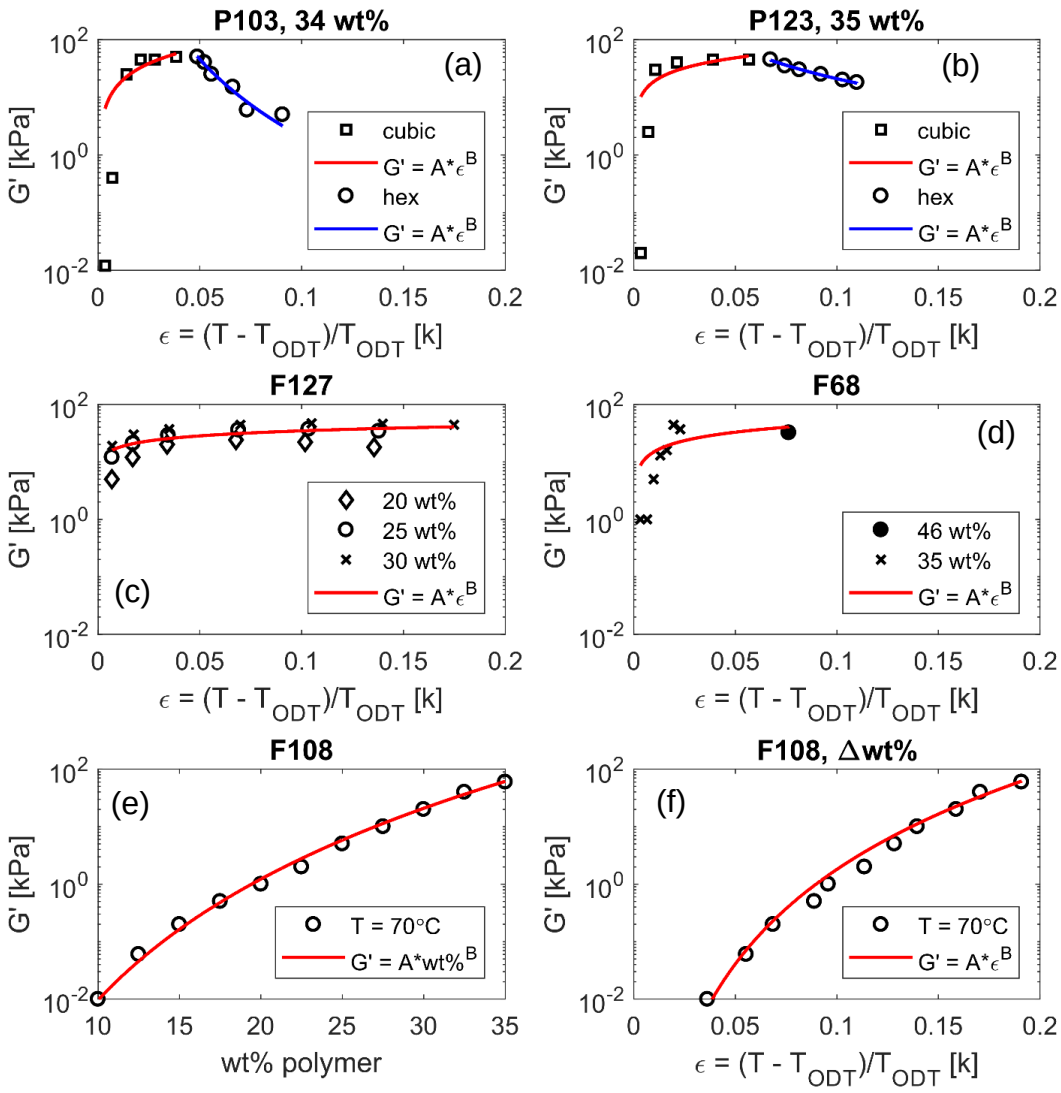

Figure 2.2: Effect of concentration and temperature difference from the order to disorder temperature (ODT) on the storage modulus (G'). Red lines are fits for cubic phase and blue lines are fits for the hexagonal phase using equations (1-2) (Parameters in Table 2.1). (a) G' in the cubic phase (squares) and hexagonal phase (circles) as a function of ε for 34 wt% P103. (b) G' in the cubic phase (squares) and hexagonal phase (circles) as a function of ε for 35 wt% P123. (c) G' in the cubic phase as a function of ε for 20 wt % (diamonds), 25 wt% (circles), and 30 wt% (Xs). (d) G' in the cubic phase as a function of ε for 35 wt% F68 (Xs) and 46 wt% (circle). (e) The effect of concentration on G' at constant temperature for F108 (f) The effect of concentration on the ODT is also captured with ε for F108.

Table 2.1: A summary of rheological data for concentrated PEO-PPO-PEO block polymer solutions. Data is for cubic phases (BCC or FCC). Blue shading denotes a hexagonal birefringent phase.

Notation: The first letter denotes paste (P), liquid (L), or flakes (F). The last digit is roughly the percentage of ethylene oxide, and the middle number(s) when multiplied by 300 is roughly the molecular weight of the PPO block.

Polymer	Solvent	(EO-PPO-EO)	MW (g/mol)	wt%	T_{ODT} (°C)	T (°C)	$\varepsilon = (T-T_{ODT})/T_{ODT}$	G' (kPa)	Figures Available & References
P103	water or heavy water	17-62-17	4950	34	14	15	0.003	0.012	Phase diagram [45], temperature sweeps, G* over time [13,46]
						16	0.007	0.4	
						18	0.014	25	
						20	0.021	45	
						22	0.028	45	
						25	0.038	50	
						28	0.049	50	
						29	0.052	40	
						30	0.056	25	
						33	0.066	15	
						35	0.073	6	
						40	0.091	5	
P123	water or heavy water	20-70-20	5750	35	9	10	0.004	0.02	phase diagram [13,31], Temperature Sweeps (35 wt%) [13,46], G* over time [13]
						11	0.007	2.5	
						12	0.011	30	
						15	0.021	40	
						20	0.039	45	
						25	0.057	45	
						28	0.067	45	
						30	0.074	35	
						32	0.082	30	
						35	0.092	25	
						38	0.103	20	
						40	0.110	18	
F127	water or heavy water	99-69-99	12600	20	22	24	0.007	5	phase diagram [31], temperature sweeps [47,48], amplitude sweeps [6], frequency sweeps [6]
						27	0.017	12	
						32	0.034	20	
						42	0.068	24	
						52	0.102	22	
						62	0.136	18	
				25	17	19	0.007	12	
						22	0.017	21	
						27	0.034	29	
						37	0.069	36	
						47	0.103	37	
						57	0.138	34	
				30	13	15	0.007	19	
						18	0.017	30	
						23	0.035	37	
						33	0.070	44	
						43	0.105	47	
						53	0.140	46	

						63	0.175	44	
F68	water	78-30-78	8350	35	33	34	0.003	1	phase diagram [31], temperature sweep [49], frequency sweeps [25,49], T_{ODT} at 46 wt% [50], creep and recovery, flow (steady state shear rate) [25]
						35	0.128	1	
						36	0.132	5	
						37	0.136	13	
						38	0.139	16	
						39	0.143	44	
						40	0.147	37	
				46	2	23	0.076	32	
F108	water	133-50-133	14600	10	58	70	0.036	0.01	phase diagram [24], temperature sweeps [44], frequency sweeps [24,25], creep and recovery, flow (steady state shear rate) [25]
				13	52		0.160	0.06	
				15	48		0.150	0.2	
				18	42		0.133	0.5	
				20	40		0.128	1	
				23	35		0.114	2	
				25	31		0.102	5	
				28	28		0.093	10	
				30	23		0.078	20	
				33	20		0.068	40	
				35	15		0.052	60	

2.8 Formulation of PEO-*b*-PPO-*b*-PEO triblock solutions – rheology and SAXS

Pluronic P123 [PEO_{20}-PPO_{70}-PEO_{20}] (Sigma Aldrich, lot# MKCH4375), F127 [PEO_{106}-PPO_{70}-PEO_{106}] (Sigma Aldrich, lot# BCBX9224), and F87 [PEO_{75}-PPO_{46}-PEO_{75}] (BASF, lot# 0008779132) were used as received. Bicarbonate buffer (pH = 9) was made with purified 18.2 MΩ·cm water. Triblock solutions were made with bicarbonate buffer and mixed end over end at 8°C for at least 24 hours to ensure sufficient dispersion and dissolution of the polymer.

While scattering data available in the literature provide an excellent starting point, it is worth noting that the crystalline unit cell size measurements did not often have the full concentration and temperature range of interest. Further complicating this, most available scattering data is with high-purity water as the solvent. The presence of buffer salts in the solvent will shift the phase transitions as detected by rheological studies.[51] Previous work has shown significant phase boundary shifts and even complete loss of solid-phase formation in F127 due to the addition of certain salts to the solvent.[52–54]

Samples demonstrating favorable macroscopic properties as determined by rheological studies were set aside for thorough structural classification via small angle X-ray scattering (SAXS). SAXS measurements were performed at the 12-ID-B beamline at the Argonne National Lab Advanced Photon Source (APS, Argonne, IL, U.S.A). Samples

were hermetically sealed into alodined aluminum DSC pans (TA instruments, Newcastle, DE). Samples were equilibrated for at least 5 minutes at the desired temperature prior to data collection. Typical exposure times were about 1 second. An incident beam energy of 13.3 keV (λ = 0.932 Å) was used. 2D-SAXS patterns were acquired on a Pilatus 2M detector with 172 μm x 172 μm resolution. The wavevector, $q = (4\pi/\lambda)\ \sin(\theta/2)$ was calibrated with a silver behenate standard.

The first step of this formulation process was to identify aqueous triblock systems with large cubic regions on their phase diagram. As described above, the literature is offers a breadth of data on aqueous systems to serve as an anchoring point for more complicated formulations. The goal of this formulation attempt was to find systems demonstrating BCC or FCC phases across a wide temperature range. These systems were then used to study protein diffusivity throughout the crystalline lattice in Chapter 5. An ideal material will be a solid-like gel within the temperature range of interest (25-55°C). Additionally, the material must experience a reversible order-disorder transition below room temperature but above the freezing point of water: between 15 and 0°C. Rheological temperature ramps were used to find triblock concentrations that meet this constraint. Three triblock polymers (Pluronic F87, F127, and P123) were chosen for initial investigation due to their reported phase diagrams showing ODTs in the region of interest.[6,55–57]

Figure 2.3 shows the magnitude of the complex modulus, |*G**|, and the phase angle, δ, for several concentrations of F87, F127, and P123 during temperature ramps between 0 and 60°C. All samples shown experience a disordered liquid-like state at 0°C as shown by δ ~ 90°. As temperature is increased, the block polymer micelles crystallize resulting in a sharp reduction in δ and 4-5 orders of magnitude increase in |*G**|. For P123 (Figure 2.3A) as the samples are heated from 0°C, there is an increase in modulus over a 1-5°C window as the material crystalizes through a lower ODT. As the samples are heated further a solid-like phase is observed. A subsequent upper ODT is observed with further heating for all concentrations of P123 tested. At the lowest concentration tested, 25 wt%, the upper ODT is only 15°C higher than the lower ODT. At an intermediate concentration of 30 wt% P123, a sharp lower and upper ODT with a consistent modulus from 14-38°C was observed. Significant changes in modulus with temperature were observed in this solid region, which could signify phase transitions with temperature.[21,22,58]

For F87 and F127 (Figures 2.3B and 2.3C), increasing Pluronic concentration results in a reduction in the ODT and increase of the modulus observed after crystallization. As the samples are heated from 0°C, there is a sharp increase in modulus over a 1-2°C window as the material solidifies through the ODT. As the samples are heated further into the solid-like phase, a plateau in modulus is observed. Increasing polymer concentration reduces the change in modulus with temperature above the ODT within this

plateau. F87 and F127 show only a lower ODT with a sharp transition in all samples tested. This reversible phase transition can be tuned to occur between 15 and 0°C by adjusting concentration, facilitating protein dispersion in the disordered phase via refrigeration. These samples form crystalline phases that show stable rheological properties within the temperature window of 25-55°C.

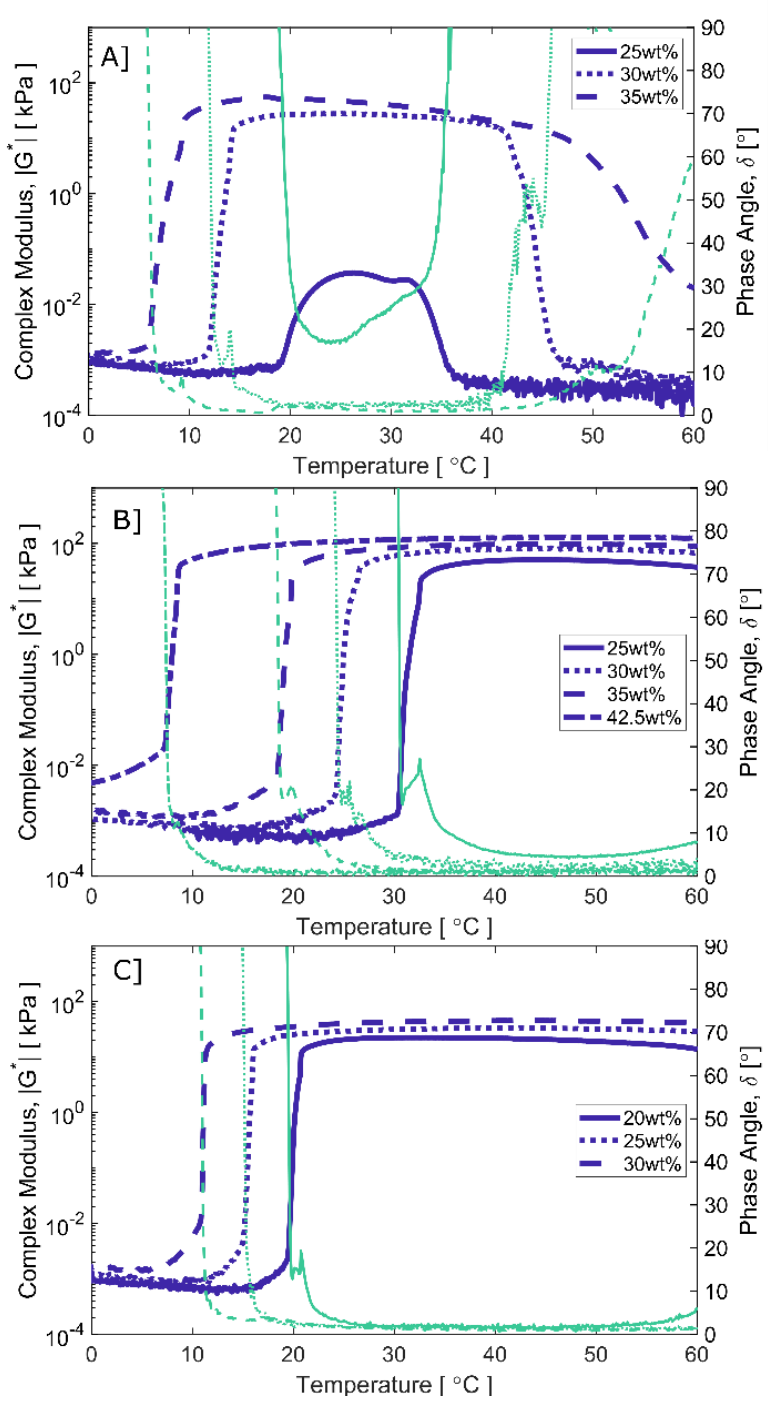

Figure 2.3: Complex modulus (|*G**|, blue lines) and phase angle (δ, cyan lines) as a function of temperature for **[A]** P123 25, 30, and 35wt% in bicarbonate buffer demonstrating the effect of concentration on the lower and upper ODTs. **[B]** F87 25,30,35, and 42.5wt% in bicarbonate buffer demonstrating decreasing lower ODT with increasing concentration. **[C]** F127 20, 25, and 30wt% in bicarbonate buffer demonstrating decreasing lower ODT with increasing concentration.

Figures 2.4-2.6 show rheological frequency sweeps for P123, F87 and F127 taken at temperatures in the solid-like regions found during the temperature sweeps outlined in Figure 2.3. For P123 (Figure 2.4) we can see a large increase in the modulus at all frequencies as concentration is increased from 25 to 35 wt%. All samples demonstrate viscoelastic solid behavior with G' > G''. At both concentrations, from 25-35°C we observe an increase in G'' with decreasing frequency. This could indicate a crossover between G' and G'' at frequencies below those tested. For 25wt% P123, the effect of temperature from 25 to 35°C results in a slight decrease in modulus at low frequency. For P123 35wt%, increasing the temperature from 25 to 45°C results in a significant decrease in G' across the entire frequency range, while G'' remains constant. This decrease in the ratio of G' to G'' reflects a shift towards a more liquid-like state with heating. Finally at 55°C we observe a 2-3 order of magnitude decrease in G' and G'', which is also seen in the temperature ramps. This likely corresponds to a phase change in this region for P123.

For F87 (Figure 2.5) we observe remarkable consistency in G' and G'' with increasing temperature at the 4 concentrations which frequency sweeps were collected. All samples demonstrate viscoelastic solid behavior with G' > G''. In all samples tested, G' remains fairly consistent from 1-100 rad/s with a small decrease as frequency decreases from 1-0.001 rad/s. It is possible that G'' will continue to increase with decreasing frequency, leading to a crossover in the region of 0.001 rad/s. For F127 (Figure 2.6)

we again observe consistency in G’ and G’’ with increasing temperature at the 3 concentrations which frequency sweeps were collected. All samples demonstrate viscoelastic solid behavior with G’ > G’’. In all samples tested, G’ remains consistent across the entire frequency window. It is possible that G’’ will continue to increase with decreasing frequency, leading to a crossover lower than 0.001 rad/s.

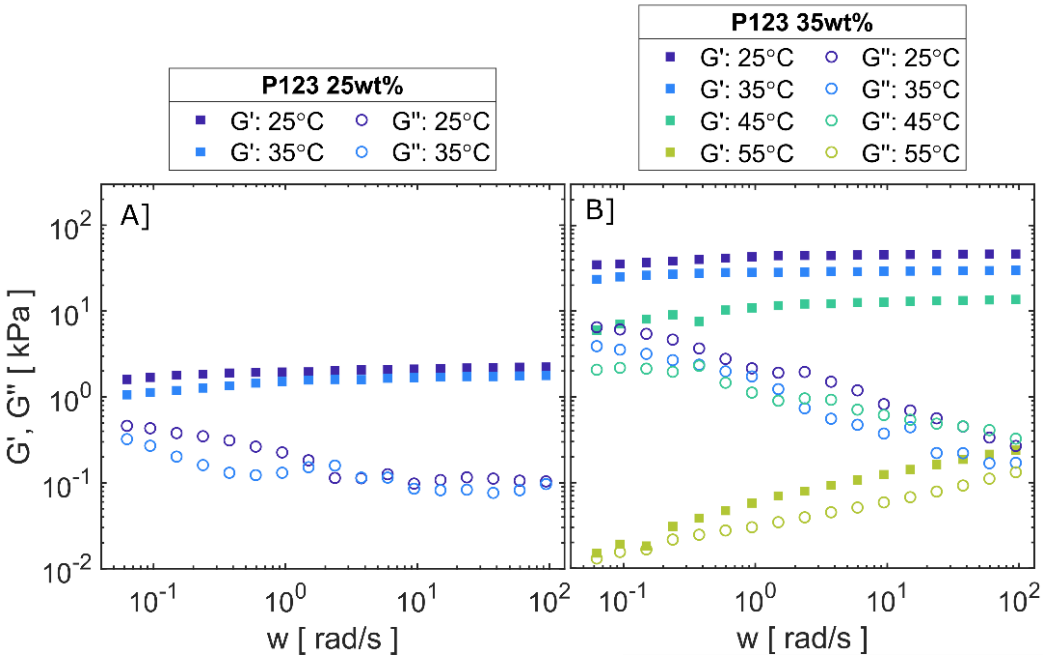

Figure 2.4: Storage modulus (G’, squares) and loss modulus (G’’, circles) as a function of shear frequency for Pluronic P123 in bicarbonate buffer at temperatures demonstrating solid-like properties. **[A]** P123 25wt% **[B]** P123 35wt%

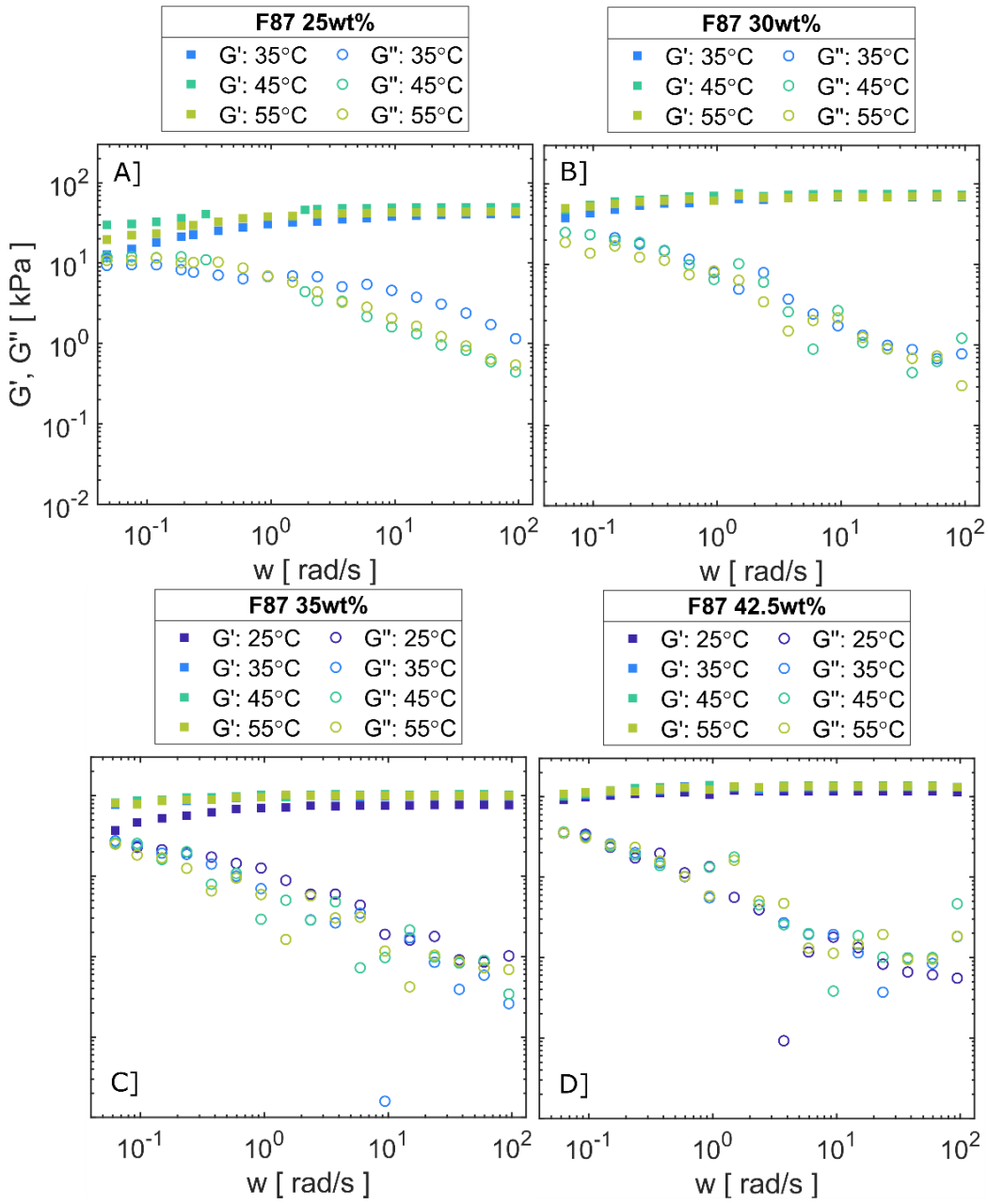

Figure 2.5: Storage modulus (G', squares) and loss modulus (G'', circles) as a function of shear frequency for Pluronic F87 in bicarbonate buffer at temperatures demonstrating solid-like properties. **[A]** F87 25wt% **[B]** F87 30wt% **[C]** F87 35wt% **[D]** F87 42.5wt%

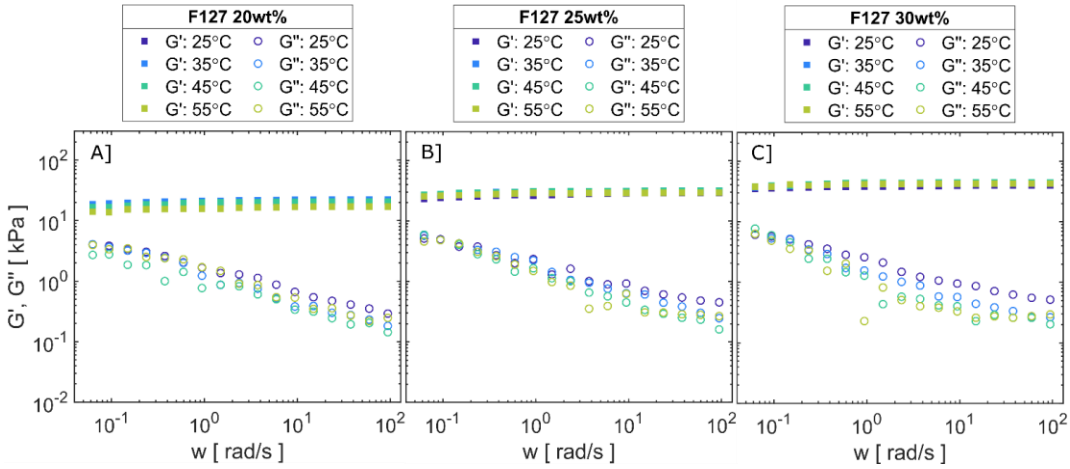

Figure 2.6: Storage modulus (G', squares) and loss modulus (G'', circles) as a function of shear frequency for Pluronic F127 in bicarbonate buffer at temperatures demonstrating solid-like properties. **[A]** F127 20wt% **[B]** F127 25wt% **[C]** F127 30wt%

Synchrotron small-angle X-ray scattering (SAXS) was used to collect structural information for samples demonstrating solid-like rheological properties at 25, 35, 45, and 55°C. The size of the crystalline unit cell (*a*) and the arrangement of the micelles within the unit cell, or crystalline phase, were resolved as a function of temperature and concentration. Figures 2.7-2.9 show 1D-SAXS profiles for F87, F127, and P123. A change in crystalline phase with increasing temperature is not observed in any of the F87 or F127 samples within the temperature window of 25-55°C. Nearly all samples demonstrated body-centered cubic (BCC) crystalline phases. For F87 and F127, the unit cell size increases slightly with increasing temperature, as demonstrated by a slight decrease in the location of the first peak. In F87 the unit cell size is nearly constant with increasing concentration (Figure

2.7), however in F127 a decrease in unit cell size with increasing concentration is observed (Figure 2.8).

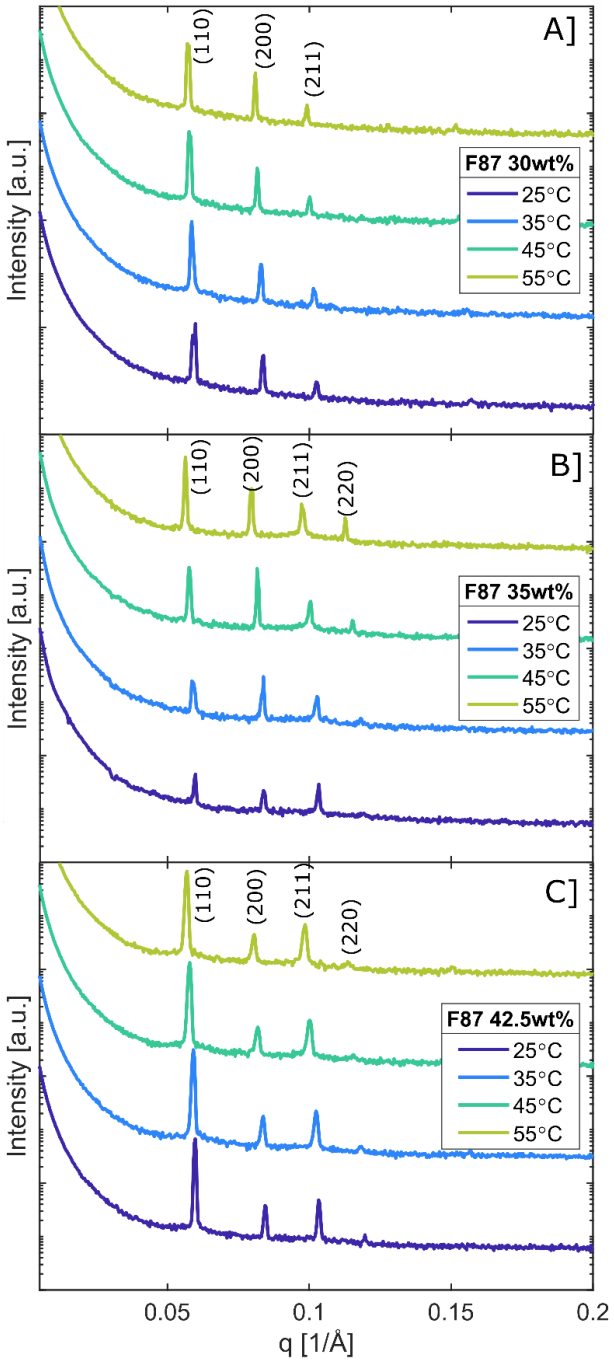

Figure 2.7: 1D-SAXS profiles for **[A]** F87 30wt% **[B]** F87 35wt**% [C]** F87 42.5wt% Indexed peaks for BCC are overlaid. Increasing temperature does not change the crystalline phase. A slight downshift in the first peak indicates an increase in unit cell size with increasing temperature.

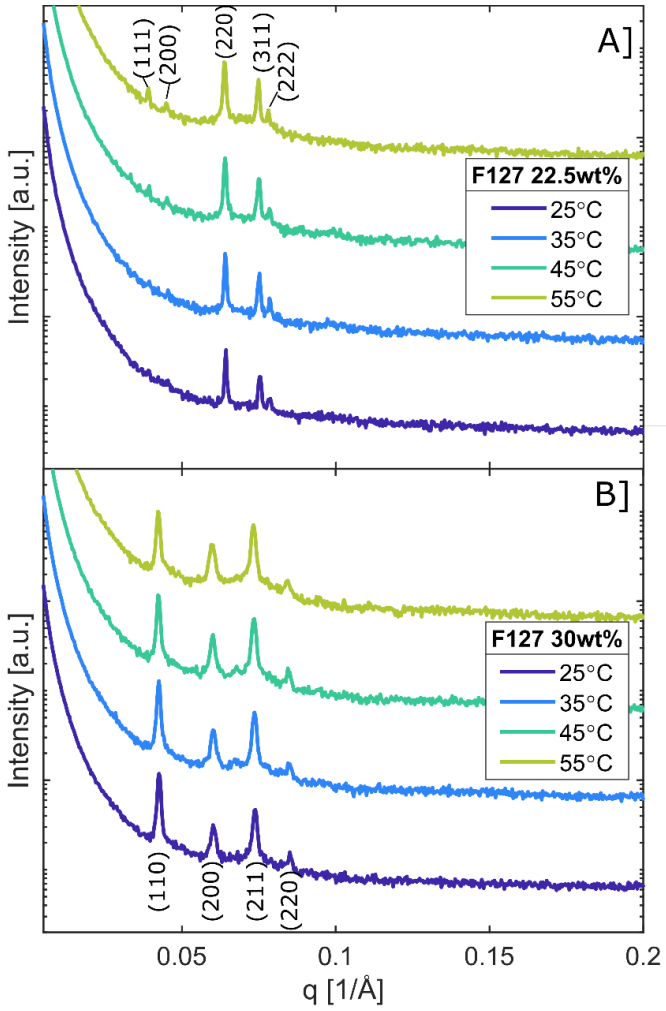

Figure 2.8: 1D-SAXS profiles for **[A]** F127 22.5wt%, indexed peaks for FCC are overlaid. **[B]** F127 30wt%, indexed peaks for BCC are overlaid. Increasing temperature does not change the crystalline phase.

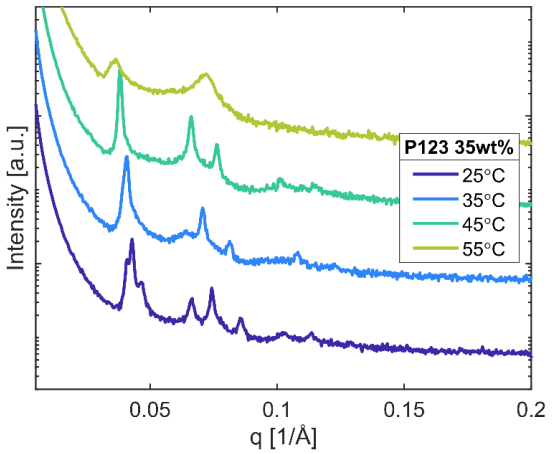

Figure 2.9: 1D-SAXS profiles for P123 35wt%. The 55°C sample demonstrates a shift towards a disordered micellar state.

This high resolution SAXS dataset can be dissected to create a structural understanding of the crystalline environment as it changes in response to temperature and concentration. Rather than sample a wide variety of phases, we intentionally focus on the changes in BCC and FCC crystalline unit cell size with high accuracy. Figure 2.10 shows trends in unit cell size and micelle size with changing concentration and temperature for F127 and F87. For F87 and F127, the unit cell size increases slightly with increasing temperature. In F87 the unit cell size is nearly constant with increasing concentration, however in F127 a decrease in unit cell size with increasing concentration is observed (Figure 2.10). The arrangement of micelles (the phase), the size of the crystalline unit cell, and the size of the micelles are all known with high accuracy with temperature and concentration (Tables 2.2-2.4). This dataset and the techniques employed

to create it will be useful to formulation attempts involving block polymer crystalline phases.

Table 2.2: SAXS characterization for Pluronic F87 in bicarbonate buffer. SAXS data for Pluronic F87 were collected for 30, 35, and 42.5 wt% samples. For concentrations without SAXS data, the phase is assumed to be BCC and the micellar radius is determined via a 2nd-order polynomial fit and extrapolation from 30, 35, and 42.5 wt%. Included is the location of the first peak (*q1*), the unit cell size (*a*), the hard sphere radius of the micelles (R_m), the radius of the octahedral site (R_{oct}), and the radius of the hole between micelles at the triangular face of each octahedral site (R_{hole}).

Pluronic	Wt %	T [°C]	q1 [Å^{-1}]	phase	a [nm]	R_m [nm]	R_{oct}	R_{hole}	Extrapolated?
F87	30	25	0.0593	BCC	14.99	6.49	4.11	1.46	SAXS data
		35	0.0585	BCC	15.20	6.58	4.17	1.48	
		45	0.0578	BCC	15.38	6.66	4.22	1.50	
		55	0.0572	BCC	15.53	6.72	4.26	1.51	
	35	25	0.0597	BCC	14.89	6.45	4.08	1.45	SAXS data
		35	0.0593	BCC	14.97	6.48	4.10	1.46	
		45	0.0577	BCC	15.41	6.67	4.22	1.50	
		55	0.0563	BCC	15.79	6.84	4.33	1.54	
	37.5	25	Extrapolated	BCC	14.86	6.44	4.07	1.45	Extrapolated
		35		BCC	14.94	6.47	4.09	1.45	
		45		BCC	15.40	6.67	4.22	1.50	
		55		BCC	15.81	6.85	4.33	1.54	
	40	25	Extrapolated	BCC	14.86	6.44	4.07	1.45	Extrapolated
		35		BCC	14.95	6.47	4.10	1.46	
		45		BCC	15.39	6.66	4.22	1.50	
		55		BCC	15.76	6.82	4.32	1.53	
	42.5	25	0.0597	BCC	14.88	6.44	4.08	1.45	SAXS data
		35	0.0592	BCC	15.02	6.50	4.12	1.46	
		45	0.0578	BCC	15.37	6.65	4.21	1.50	
		55	0.0568	BCC	15.63	6.77	4.28	1.52	

Table 2.3: SAXS characterization for Pluronic F127 in bicarbonate buffer. SAXS data for Pluronic F127 were collected for 22.5 and 30wt% samples. For concentrations without SAXS data, the phase is assumed to be BCC and the micellar radius is determined via a linear extrapolation of the micellar radius measured at 22.5 and 30wt%. Included is the location of the first peak (*q1*), the unit cell size (*a*), the hard sphere radius of the micelles (R_m), the radius of the octahedral site (R_{oct}), and the radius of the hole between micelles at the triangular face of each octahedral site (R_{hole}). For 22.5 wt% samples, q1 is taken to be the 220 peak, which is the 3rd peak seen in FCC. The first two peaks, (111) and (200), were visible but the 220 peak provided a more distinct anchor for unit cell size calculations.

Pluronic	Wt %	T [°C]	q1 [Å^{-1}]	phase	a [nm]	R_m [nm]	R_{oct}	R_{hole}	Extrapolated?
F127	22.5	25	*0.0642	FCC	27.69	9.79	4.06	2.20	SAXS data
		35	*0.0641	FCC	27.74	9.81	4.06	2.20	
		45	*0.0640	FCC	27.79	9.82	4.07	2.21	
		55	*0.0638	FCC	27.87	9.85	4.08	2.21	
	25	25	Extrapolated	BCC	22.11	9.57	6.06	2.15	Extrapolated
		35		BCC	22.15	9.59	6.07	2.16	
		45		BCC	22.19	9.61	6.08	2.16	
		55		BCC	22.25	9.63	6.10	2.17	
	28	25	Extrapolated	BCC	21.48	9.30	5.89	2.09	Extrapolated
		35		BCC	21.53	9.32	5.90	2.10	
		45		BCC	21.57	9.34	5.91	2.10	
		55		BCC	21.61	9.36	5.92	2.10	
	30	25	0.0426	BCC	20.85	9.03	5.72	2.03	SAXS data
		35	0.0425	BCC	20.91	9.05	5.73	2.03	
		45	0.0424	BCC	20.96	9.07	5.74	2.04	
		55	0.0424	BCC	20.98	9.09	5.75	2.04	

Table 2.4: SAXS characterization for Pluronic P123 in bicarbonate buffer**.** SAXS data for Pluronic P123 were collected for 35wt% samples. Included is the location of the first peak (*q1*), the unit cell size (*a*), and the cylindrical radius of the micelles (R_m).

Pluronic	Wt %	T [°C]	q1 [Å^{-1}]	phase	a [nm]	R_m [nm]
P123	35	25	0.0410	HEX +BCC	15.32	7.66
		35	0.0407	HEX	15.42	7.71
		45	0.0382	HEX	16.46	8.23
		55	0.0000	DIS.	0.00	0.00

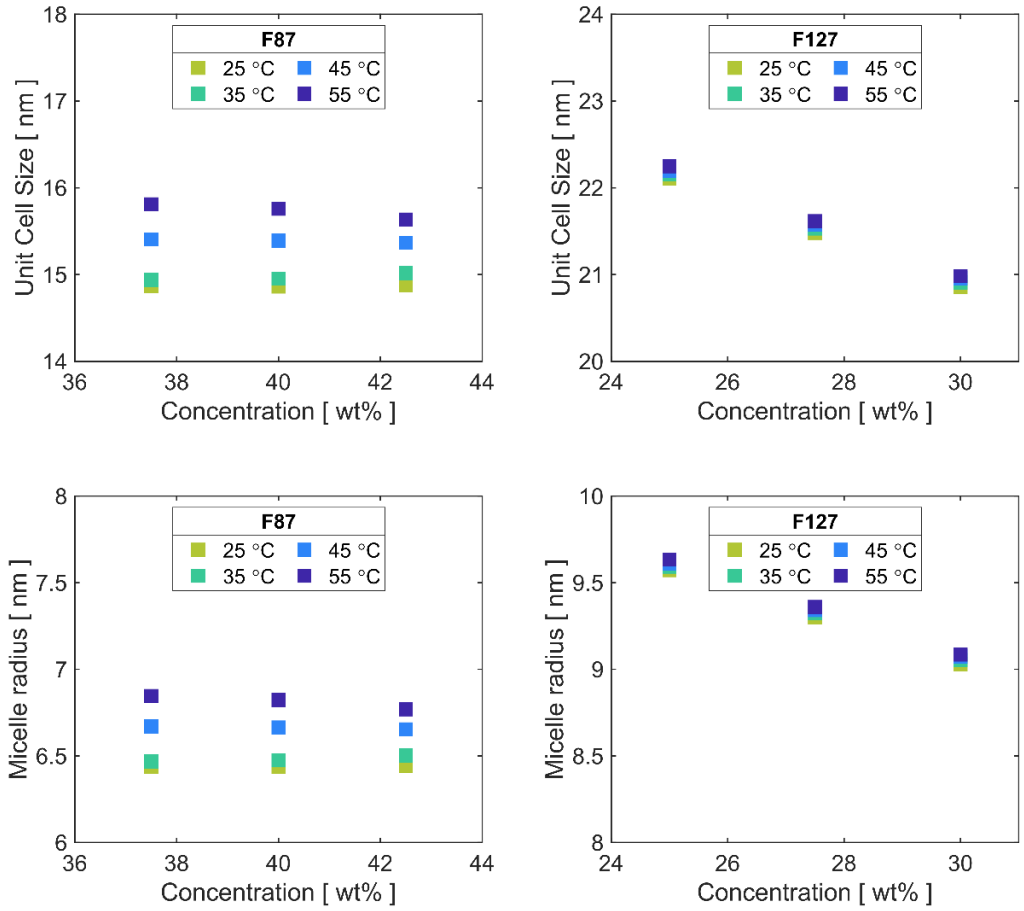

Figure 2.10: Unit cell size and corresponding micelle radius as calculated using SAXS data for F87 (Table 2.2) and F127 (Table 2.3).

2.9 Summary

A review of phase behavior of linear diblock (AB) and triblock (ABA) block polymers in solvents with preferential selectivity for one of the blocks shows significant complexity. Limitations predicting phase behavior even in simple binary polymer and solvent solutions warrant further experimental and theoretical study. Formulators need access to accurate phase behavior data in addition macroscopic property data across wide composition and temperature ranges. Unfortunately, this combination is rarely available in the scientific literature. Formulators seeking to use materials with self-assembled polymeric crystalline structures must become experts in a variety of experimental methods to record this data themselves.

To study phase behavior in these systems, jar tests are used to locate ODTs, birefringence is used to identify or lamellar and cylindrical phases, rheological temperature sweeps have been used to narrow regions of interest for ODTs and OOTs, and small angle scattering is used to obtain quantitative structural data. Improved methods for rapidly surveying phase diagrams will yield experimental insights and inform predictive models. Further rheological studies may provide conclusive “fingerprints” for the various phases seen in these systems, providing a way to rapidly identify phases widely available rheometers. Processing of these systems will be required to realize the full potential of the self-assembled structures in these systems. This will require understanding the complicated flow mechanisms that are dependent on the crystalline nanostructure.

To demonstrate the effects of polymer architecture and molecular weight on macroscopic rheological data from the literature is compiled into useful trends. Rheological studies have provided enormous insights into the properties and flow mechanisms of these materials. When coupled with small angle scattering data, the nanoscale structures can be linked to these macroscopic properties. These methods will be useful for formulation attempts that leverage self-assembled crystalline lattices in block polymer systems to produce desirable macroscopic properties. The liquid crystalline structures formed in these polymer solutions have an enormous impact on the possible flow mechanisms, which dictate the material's response to external shear fields during processing.

Chapter 3 Rheological Characterization of BCC and FCC packings in aqueous diblock polymer liquid crystals

Valentine C.S., Walker L.M., "Rheological Characterization of BCC and FCC Structures in Aqueous Diblock Polymer Liquid Crystals". *Korea-Aust. Rheol. J.* (2019). https://link.springer.com/article/10.1007/s13367-019-0025-2

Low molecular weight, amphiphilic diblock copolymers in selective solvent exhibit complex phase behavior and macroscopic properties that affect the processing of these materials to create desirable macroscopic properties. The mechanical properties of the crystalline phases seen in concentrated solutions are dependent on nanoscale structure and sample history. In this chapter we investigate the impact of thermal history on phase behavior in an aqueous diblock system, where the micellar coronas are composed of PEO brushes. Thermal history can be a powerful tool to achieve desirable mechanical properties during formulation and production of useful products. These mechanical properties arise from the crystalline nanostructure, also known as the crystalline phase. Therefore, it is crucial to understand the changes to the crystalline phase that are occurring during thermal processing.

Small angle X-ray and Neutron scattering data are powerful and well-established tools to quantitatively measure the crystalline phase in block polymer systems. However, these experiments are not always available to scientists for use during formulation attempts due to their monetary or time cost. Lab-scale equipment for small angle X-ray scattering can cost millions

of dollars, and access to government established labs can be limited by demand for the facilities. Additionally, the time allotted for experiments at these national facilities may not be enough to explore a wide formulation space. This is not meant to downplay the immense importance of these facilities towards advancing our scientist understanding of nanostructured materials, but rather to convey to the reader that time with scattering instruments should be regarded as a precious commodity. Rheometric tools are widely available and can be used to identify regions of interest in the formulation parameter space before spending crucial time and resources on scattering experiments.

In this chapter we develop rheological techniques that could be used to identify crystalline phases and phase boundaries in block polymer liquid crystals. Rheological temperature ramps are used to characterize three aqueous concentrations of diblock copolymer [Brij-58®, $C_{16}H_{33}$-$(CH_2CH_2O)_{20}OH$]. Between these three samples the order-disorder transitions (ODTs) for BCC and FCC are accessible in addition to the order-order transition (OOT) between BCC and FCC. These transitions are distinguished by rheological methods. Frequency sweeps are performed across a range of temperatures and parameterized with a three mode Maxwell model to extract the longest relaxation time. We find that a single frequency sweep does not distinguish BCC and FCC structures. By normalizing the temperature with respect to the ODT, we use a series of

frequency sweeps to distinguish characteristic trends in the response of BCC and FCC structures to thermal history.

3.1 Relaxation timescales of liquid crystalline structures

Block copolymer molecules in a selective solvent self-assemble into nanostructured soft materials, for example see “Block Copolymers in Solution: Fundamentals and Applications”.[1] The amphiphilic nature of a diblock copolymer molecule drives assembly of micelles in both the melt state and solvent-swollen state. For a given polymer architecture, concentration, temperature, and solvent quality, micelles will form crystalline lattices known as lyotropic liquid crystals (LLCs.[1,8] A single system can have multiple accessible LLC packings including body-centered cubic (BCC), face-centered cubic (FCC), hexagonally close-packed spheres (HCP), hexagonally close-packed cylinders (H_I), and lamellar phases (L_α).[9] Solvent selectivity for at least one of the polymer blocks often varies with temperature, broadening the accessible number and types of phases.[9] The thermoreversible order-order transitions (OOTs) and order-disorder transitions (ODTs) between phases can be located using a number of structural (small angle scattering, birefringence) and macroscopic (jar inversion tests, rheological) techniques.[6,10] The mechanical properties, nanoscale crystalline structure, and phase transition boundaries are dependent on sample history. For example, the thermal history of a sample can shift ODTs and OOTs and initiate metastable phases which are kinetically trapped, preventing a transition back to thermodynamic equilibrium.[11,12] Hysteresis, or a dependence of structure on thermal sample

history, near OOTs has been observed in several block polymer systems.[11–13]

Relaxation mechanisms that occur at timescales measurable by rheology are present in micellar cubic liquid crystals. The storage modulus (*G'*) and loss modulus (*G''*) in these systems often is strongly frequency dependent, which allows for the study of these timescales. Previous studies have attempted to use the frequency dependence of the storage and loss modulus as a signature or fingerprint for specific liquid crystalline structures.[21,22] Individual crystal grains in these phases can be aligned and annealed into larger crystalline domains via shear. Under continuously increasing stress (steady shear) it has been shown that BCC crystals show no yield stress in addition to two plateaus in the stress versus shear rate data, while FCC crystals show a distinct yield stress and strong shear thinning behavior.[59,60] In aqueous Pluronic® systems it was found that shear flow will align BCC and FCC structures and anneal grains, but that this has a minimal impact on the frequency dependence of the storage and loss modulus.[60]

Models have been developed to relate the viscoelastic properties of these materials to molecular or nanoscale structures. Mezzenga et al. attribute the longest relaxation time from a multimode Maxwell model to the relaxation of the lipid-water interface.[1,22,61] Jones and McLeish modelled the response of micellar cubic phases to oscillatory shear using a slip-plane model.[62] This model accounts for the slip-planes that arise during shear in

these phases that give rise to bulk relaxation mechanisms. One prediction from this model is solid-like behavior at high frequencies and Maxwell liquid-like behavior at low frequencies; a main consequence of this model is a single relaxation time for the bulk that depends on the average slip plane density. This single timescale arises despite a distribution of slip-plane densities in the crystal. A modified version of this model has been applied where the bulk relaxation time is modeled as a log-normal distribution of relaxation times with a maximum relaxation time (τ_{max}) given by the inverse of the crossover frequency (ω_c) of G' and G'' ($\tau_{max} \sim 1/\omega_c$). This modified slip-plane theory model has been applied to micellar cubic phases and reverse cubic phases, with excellent agreement to the experimental data.[63,64] Rather than this modified slip-plane model, in this work we use a general three-mode Maxwell model to consistently parameterize the data while using the minimum number of modes to adequately capture $\tau_{max} \sim 1/\omega_c$.

The techniques outlined above can be used to better characterize new materials, thermal history effects, and to guide processing. The goal of this study is to characterize macroscopic properties of lyotropic liquid crystals in diblock copolymer solutions, specifically the BCC and FCC phases.

3.2 Materials and Methods: Rheological Temperature ramps

Brij 58® is purchased from Sigma Aldrich (lot # SLBT3530) and used as received. The reported chemical formula is $C_{16}H_{33}(CH_2CH_2O)_{20}OH$. Samples are made with purified 18.2 MΩ·cm water and sealed in glass jars. Samples are then held at 80°C for at least 24 hours to facilitate polymer dispersion. Immediately after heating the solutions are vigorously hand mixed and transferred to centrifuge tubes. Air bubbles are removed via two or more 90-minute cycles of centrifugation at 40°C and 3250g.

Rheological measurements are performed on a TA instruments (TA Instruments; New Castle, DE) DHR-2 stress-controlled rheometer. A 40 mm parallel plate configuration is used with a 500 μm gap height. Temperature control is provided by a Peltier system in the bottom plate. Before beginning measurements, samples are heated to 5 °C above the ODT to remove loading stresses. To prevent evaporation, a 4 cm tall Teflon ring is sealed to the bottom plate using vacuum grease, and ~20 mL of FC-70 Fluorinert® fluorinated oil is poured into the ring. This creates a 2 cm deep pool of oil in which the geometry and sample are submersed. The extra torque from the oil pool is negligible in the structured polymer samples. The magnitude of the complex modulus, $|G^*|$, ranges from 150 to 400 kPa with phase angle, δ, less than 10°. These are stiff, gel-like materials.

Rheological temperature ramps are used to probe the effect of temperature on macroscopic properties, and to define ODTs. The strain amplitude for temperature ramps is verified to be in the linear viscoelastic

regime through separate amplitude sweeps at 20°C intervals. We assume that by operating in the linear regime, the applied oscillatory shear is a nondestructive probe of macroscopic properties and does not impact material structure.

Figure 3.1 shows the effect of temperature ramp rate on $|G^*|$ in a 35 wt% sample. Slower temperature ramp rates result in a more pronounced hysteresis between cooling and heating ramps. Based on this, a ramp rate for all temperature ramps of 0.2 °C/min is chosen to allow sufficient thermal equilibration throughout the gap. The precipitous drop in modulus in Figure 3.1 shows the presence of an ODT. In practice, the ODTs can be difficult to consistently define. The complex modulus drops six orders of magnitude over a 5-10 °C window when disordering from the gelled state during heating. During this precipitous change, the phase angle will fluctuate around 20°, before suddenly increasing to unphysical values. To consistently choose an ODT, we define the ODT as the temperature when $|G^*|$ reaches 5% of $|G^*|$ measured at 25 °C. Data is not shown above T_{ODT}, as the measurement of the phase angle becomes unreliable due to an experimental design optimized for measurement of stiff materials.

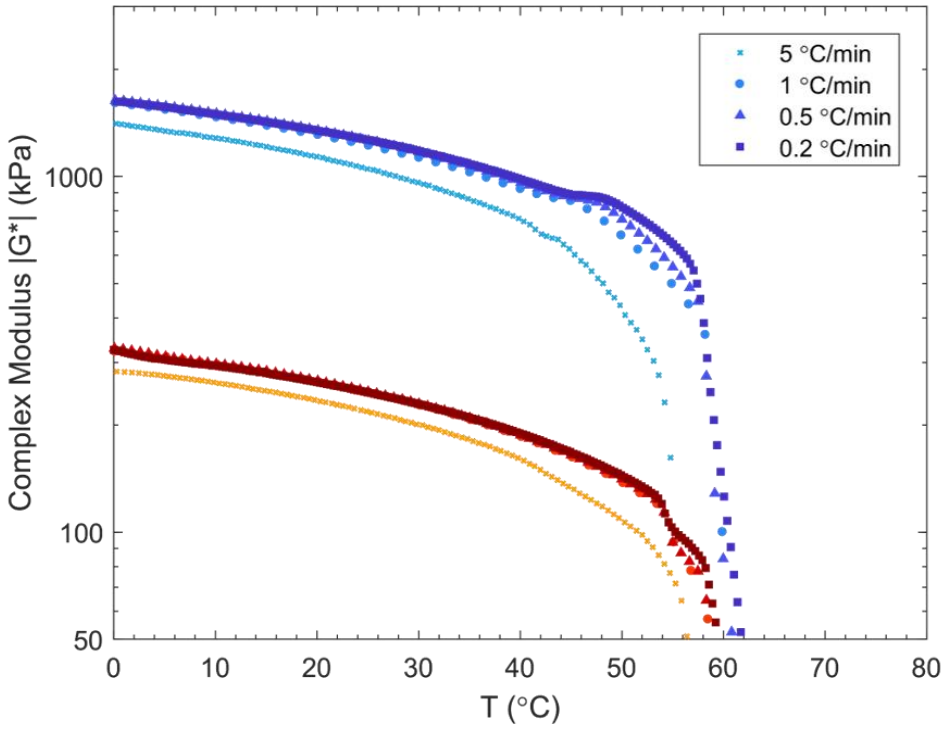

Figure 3.1: Complex modulus, |*G**|, as a function of temperature for Brij-58® in water at various temperature ramp rates (0.25%, 6.28 rad/s). Blue symbols are cooling ramps from the disordered state, red symbols are subsequent heating ramps immediately following. Cooling ramps have been shifted upwards by a factor of 3. Crosses are 5 °C/min, circles are 1 °C/min, triangles are 0.5 °C/min, and squares are 0.2 °C/min. Color darkens with decreasing temperature ramp rate.

Frequency dependent storage and loss moduli were measured during the cooling ramps for each sample. The same temperature ramp procedure is applied to disorder each sample, but the ramps are paused to record frequency sweeps at a given temperature before the cooling ramp continues. At each temperature where a frequency sweep is performed, the linear viscoelastic regime was determined at five frequencies distributed logarithmically across the range of measured frequencies.

A phase diagram for Brij-58 and water is available in the literature.[65] The structural information from Jayaraman et al. was determined via small

angle x-ray scattering (SAXS) and is used to augment rheological data with structural information in this work. The rheological data in this work are collected with different thermal history than the reported SAXS data.

3.3 Detection of BCC to FCC transition: Hysteresis in Temperature Ramps

Figure 3.2 shows the magnitude of the complex modulus (|*G**|, filled) and the phase angle (δ, open) for three different concentrations of Brij-58 (30 wt%, 35 wt%, and 42 wt%) during temperature ramps between the disordered state and T > 0 °C. The temperature decreases from the disordered state (blue) and then increases from 0 °C (red) at a rate of 0.2 °C/min as |*G**| and δ are measured at 0.25% strain and 1 Hz (0.1% strain for 30 wt%). These conditions are verified to be in the linear regime. Structural SAXS data from Jayaraman *et al.* are overlaid as vertical lines for each concentration. Continuous temperature ramp data from this study is used to refine the ODT and OOT locations. The 30 wt% data capture the FCC to disorder transition, and the 42 wt% data capture the BCC to disorder transition. The 35 wt% data capture both the FCC to BCC transition and the BCC to disorder transition.

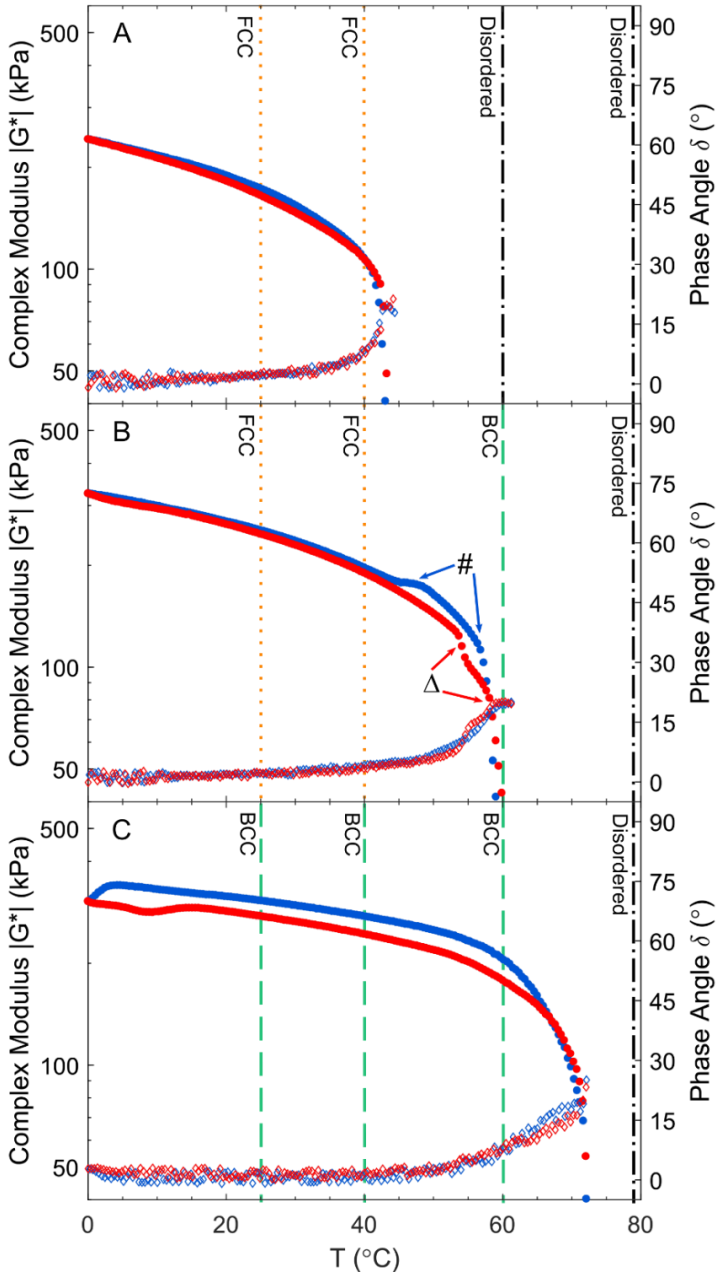

Figure 3.2: Complex modulus (|*G**|, filled circles) and phase angle (δ, open diamonds) as a function of temperature for Brij-58® in water [A = 30 wt% (0.1%, 6.28 rad/s), B = 35 wt% (0.25%, 6.28 rad/s), C = 42 wt% (0.25%, 6.28 rad/s)]. Blue symbols are cooling ramps from the disordered state, red symbols are subsequent heating ramps from 0 °C [0.2 °C/min]. Discrete data from the phase diagram are overlaid as vertical lines.[65] FCC data are shown as orange dots. BCC data are shown as light green dashes. Disordered data are shown as black dash-dots.

For the 30 wt% sample (Figure 3.2A), |*G**| increases by six orders of magnitude during cooling from the disordered phase to the FCC phase. Continued cooling results in an increase in |*G**| from 95 kPa (42 °C) to 245 kPa (0 °C) that is approximately linear with respect to temperature. The phase angle decreases during cooling from 42°C to 35°C and reaches δ = 0° from 35-0 °C. Subsequent heating to the disordered phase results in overlapping data for |*G**| and δ with differences too small to distinguish. The 30 wt% temperature ramp data capture the FCC ODT. We place the ODT at 44°C. This refines the location of the ODT and is in agreement with the ODT from the published phase diagram between data at 40 and 60°C.[65]

For the 35 wt% sample (Figure 3.2B), |*G**| again increases by six orders of magnitude during cooling from the disordered phase to the BCC phase. We place the ODT at 61°C. This refines the location of the ODT and is in agreement with the ODT from the published phase diagram between data at 60 and 80°C.[65] Continued cooling results in a doubling in |*G**| from 85 kPa (58 °C) to 175 kPa (48 °C) [# symbol, blue arrows]. There is a plateau in |*G**| at 175 kPa from 48 to 45 °C. This plateau is followed by an increase to 325 kPa as the sample is cooled from 45 to 0 °C. The phase angle decreases during cooling from 60 to 45 °C and is δ = 0° from 45 to 0 °C. Subsequent heating results in overlapping values of |*G**| and δ, but only in from 0 to 45 °C. The plateau at 175 kPa (45°C) seen during cooling is missing in the heating ramp. Rather, |*G**| continues to decrease at the same

rate until 53°C where there is a rapid 40 kPa dip in |*G**| [Δ symbol, red arrows].

The hysteresis from 40 to 60°C in the 35 wt% data is reproducible and distinct. Temperature ramps with a different minimum temperature than 0 °C show the same hysteresis for the 35 wt% samples. Unlike most OOTs the FCC to BCC transition is not usually accompanied by a drastic change in modulus, although it is sometimes observed as a small change in the viscous modulus.[28] Interestingly, the observed hysteresis occurs in a temperature range in between discrete SAXS data for the FCC phase (40°C) and the BCC phase (60°C).[65] The increase in |*G**| seen from 55 to 45 °C when cooling [# symbol, blue arrows] from the disordered state is a consequence of the BCC phase nucleating and persisting as the sample is cooled, until eventually the sample transitions to FCC near the plateau in |*G**| at 175 kPa from 48 to 45 °C. The hysteresis is an indication of an OOT from BCC to FCC during cooling near 45 °C. During heating, the 40 kPa dip in |*G**| from 53 to 58°C [Δ symbol, red arrows] is explained by an OOT from FCC to BCC during heating. There may also be regions of coexistence during heating and cooling that were not captured by discrete SAXS data used to map the phase diagram. The features in the rheological temperature ramps refine the location of the OOT between BCC and FCC.

For the 42 wt% sample (Figure 3.2C), |*G**| increases by six orders of magnitude during cooling from the disordered phase to the BCC phase. We place the ODT at 72°C. This refines the location of the ODT and is in

agreement with the ODT from the published phase diagram between data at 60 and 80°C.[65] Further cooling from 72 to 4 °C results in |*G**| steadily increasing from 80 to 340 kPa. This is followed by a 40 kPa decrease in |*G**| during cooling from 4 to 0°C. Subsequent heating shows a small decrease in |*G**| from 0 to 9°C, followed by a recovery in |*G**| from 9 to 15°C. After this small drop and recovery, further heating from 15 to 60 °C shows a trend in |*G**| that is parallel to the cooling ramp, although |*G**| is 30 kPa lower during heating. As the temperature approaches the ODT, the heating ramp data converge with the cooling ramp data. The phase angle data for both temperature ramps overlap despite the differences in |*G**|.

In the 42 wt% sample the decrease in |*G**| seen when cooling from 4 to 0 °C may represent a change in the phase behavior that was not captured on the phase diagram. A partial phase change near 0 °C would explain the hysteresis seen across almost the entire temperature range. We do not believe this change is due to freezing of the hexadecane cores, as it is not seen at other concentrations after cooling to 0 °C. Additionally, temperature ramps that begin heating at 25 °C rather than 0 °C show no hysteresis for the 42 wt% samples.

3.4 Distinct Trends in Relaxation timescale – FCC and BCC

Figure 3.3 shows the frequency dependence of the storage modulus (*G'*) and loss modulus (*G''*) for the 3 concentrations studied. The left column is 30 wt% data, the middle column is 35 wt% data, and the right column is 42 wt% data. Each row shows data taken at the temperature listed to the right of the figure. Phase data from Jayaraman et al. along with the hysteresis shown in the temperature ramp rates are used to identify each frequency sweep according to phase. FCC phases are boxed in orange dots, BCC phases are boxed in light green dashes, and disordered phases are boxed in black dash-dots. The effect of increasing temperature at a constant concentration can be seen by moving up a column. The effect of increasing concentration at constant temperature can be seen by moving to the right along a row. The qualitative features of the frequency sweeps are not enough to distinguish the difference between FCC and BCC structures. The data is fit to a three mode Maxwell model to parameterize the frequency dependent behavior. The resulting fit is shown as black lines. The unphysical oscillations around *G''* at high frequency are a consequence of the fitting algorithm prioritizing *G'*, as the values for *G'* are one or two orders of magnitude larger than G'' at high frequency. This is particularly prevalent at 0 °C, when *G'* and *G''* have the weakest frequency dependence.

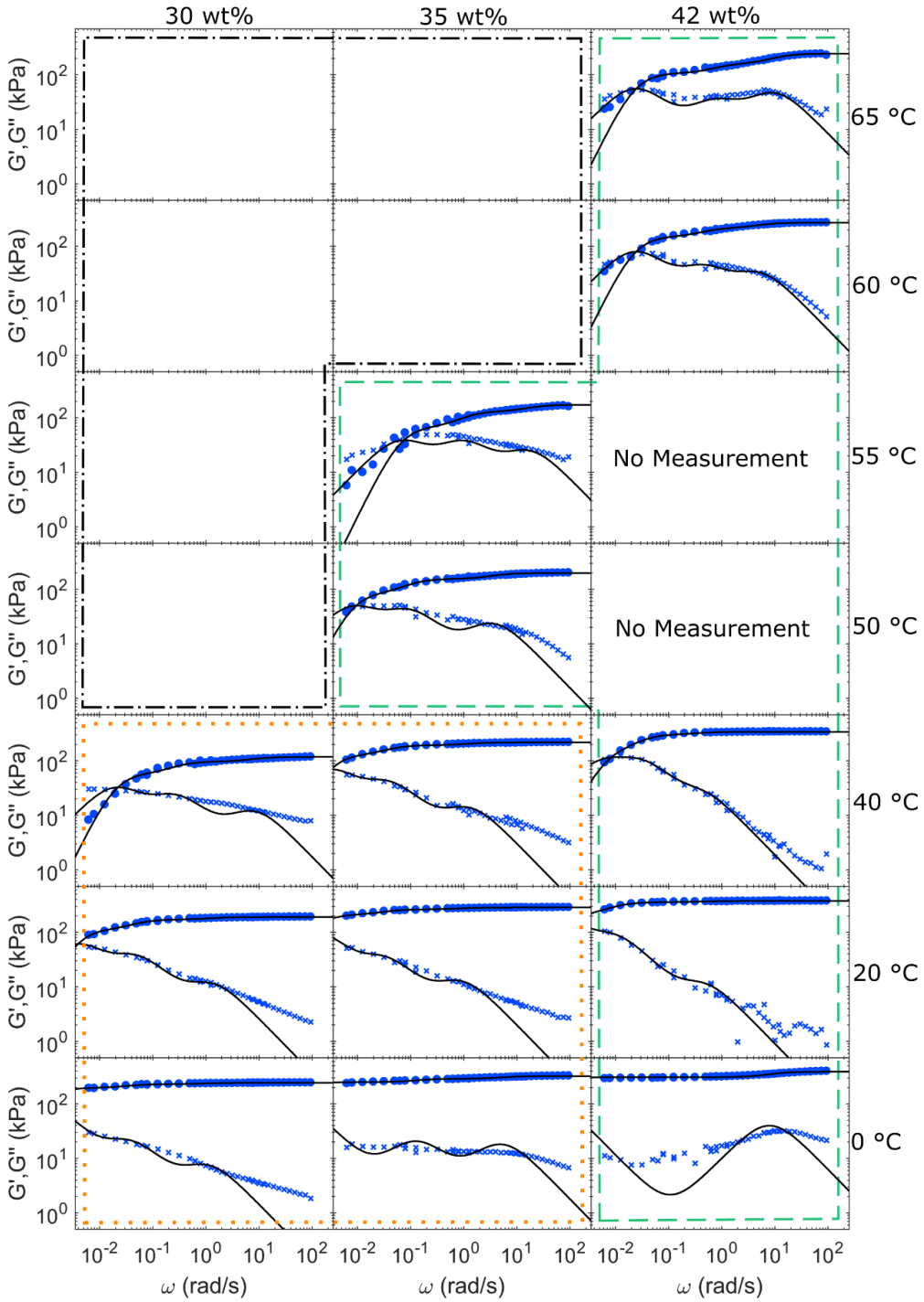

Figure 3.3: Frequency dependent storage modulus (*G'*, circles) and loss modulus (*G''*, crosses) at specified concentration (columns) and temperature (rows). FCC samples are boxed in orange dots. BCC samples are boxed in light green dashes. Disordered samples are boxed in black dash-dots.

The longest relaxation time from the Maxwell fit has been interpreted previously as the timescale for lipid-water interface to relax.[22] Increasing temperature shifts the crossover of *G'* and *G''* to higher frequencies. This corresponds to a shifting of the longest relaxation time to shorter time scales. The longest relaxation times are shown in Table 1. The longest timescale measurable is $\tau_{longest} \sim 1/\omega_{min} = 150$s, where ω_{min} is the lowest frequency measured. Timescales longer than 150s are a result of the three mode Maxwell fit extrapolating to lower frequencies. It can be seen in Figure 3.3 that the crossover frequencies at 20 °C are lower than ω_{min}, however the extrapolated Maxwell fits provide a reasonable estimate for the crossover frequency as G' and G'' near ω_{min} have begun to converge. Relaxation times longer than 750s are a result of extrapolation to frequencies half of an order of magnitude lower than ω_{min}. The 0 °C data in Figure 3.3 show that the trends in G' and G'' are relatively flat, with values an order of magnitude apart at ω_{min}. We place higher uncertainty on the 0 °C timescales as they are a result of extrapolation of trends in G' and G'' with minimal features to frequencies well outside of the measured frequency range.

Table 3.1: Longest relaxation time (τ_{max}) from a 3 mode Maxwell fit for frequency data in Figure 3.3. T_{ODT} is included for reference. FCC relaxation times are shaded in orange. BCC relaxation times are shaded light green.

τ_{max}	**0 °C**	**20 °C**	**40 °C**	**50 °C**	**55 °C**	**60 °C**	**65 °C**	T_{ODT}
30 wt%	> 750 s	270 s	50 s					44 °C
35 wt%	> 750 s	710 s	340 s	120 s	15 s			61 °C
42 wt%	> 750 s	750 s	160 s	N/A	N/A	40 s	40 s	72 °C

To determine trends in the relaxation times for each phase, we shift the temperature by T_{ODT} for each concentration and separate the data by phase. Figure 3.4 shows the relaxation times plotted against normalized temperature. Fits to a single exponential are shown for the BCC data (dashes) and the FCC data (dots). The slope of the BCC trend is 0.07 with 95% confidence bounds [0.05, 0.09] and the slope of the FCC trend is 0.05 with 95% confidence bounds [0.01, 0.09]. Timescales above 750s were excluded from the fitting process and are shown with large uncertainty bounds that are proportional to the distance from $1/\omega_{min}$.

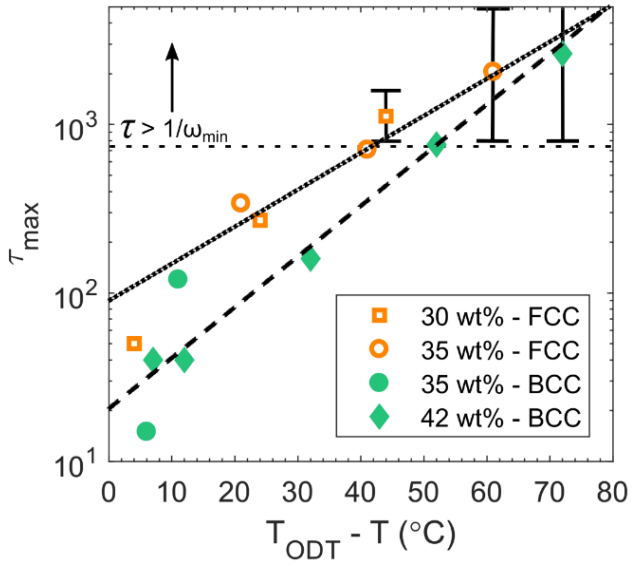

Figure 3.4: The longest relaxation time (τ_{max}) for the FCC (orange, open) and BCC (light green, filled) samples (squares = 30 wt%, circles = 35 wt%, diamonds = 42 wt%). Fits to a single exponential are shown for FCC (dots) and BCC (dashes). Temperatures are shifted by the corresponding T_{ODT} or each data. A horizontal dotted line shows $\tau_{max} = 1/\omega_{min.}$ Where $\omega_{min.}$is the minimum measured frequency. Timescales above $1/\omega_{min}$ were excluded from the fitting process. Uncertainty bounds are proportional to the distance from $1/\omega_{min.}$

There is a significant difference in the scaling of the relaxation time for each phase. Within 15 °C of the ODT there is more deviation from these trend lines. Overall, a simple exponential fit captures the trend in longest relaxation time with proximity to the ODT quite well. While a single frequency sweep is not a useful fingerprint for BCC and FCC structures, the temperature dependence of the relaxation times within each phase may prove to be a useful metric.

3.5 Conclusions

Rheological temperature ramps are used to characterize the FCC to disorder transition, BCC to disorder transition, and the FCC to BCC transition. A hysteresis is observed over the region where the OOT from BCC to FCC is expected. The features in the temperature ramps are used to refine the location of the ODTs and OOTs from the published phase diagram for samples showing FCC and BCC structures. We find that a frequency sweep at a single temperature does not distinguish BCC from FCC structures. However, by parameterizing frequency data across a range of temperatures normalized by distance from the ODT, we distinguish characteristic differences in the response of BCC and FCC structures to thermal history. We conclude that the longest relaxation time has a stronger temperature dependence in the BCC phase than in the FCC phase.

Understanding the effect of thermal history on the mechanical properties of block copolymer lyotropic liquid crystals is crucial to the application of these materials in industry. Rheometric tools are a widely available means to gain rapid insights into structural changes at the nanometer scale in self-assembling block polymer systems. The methods in this work can be used by formulators to rapidly probe mechanical properties, investigate the impact of thermal history, and gain structural insights in new systems before delegating resources to small angle scattering experiments.

Chapter 4 Shear-Modulated Rates of Phase Transitions in Sphere-Forming Diblock Oligomer Lyotropic Liquid Crystals

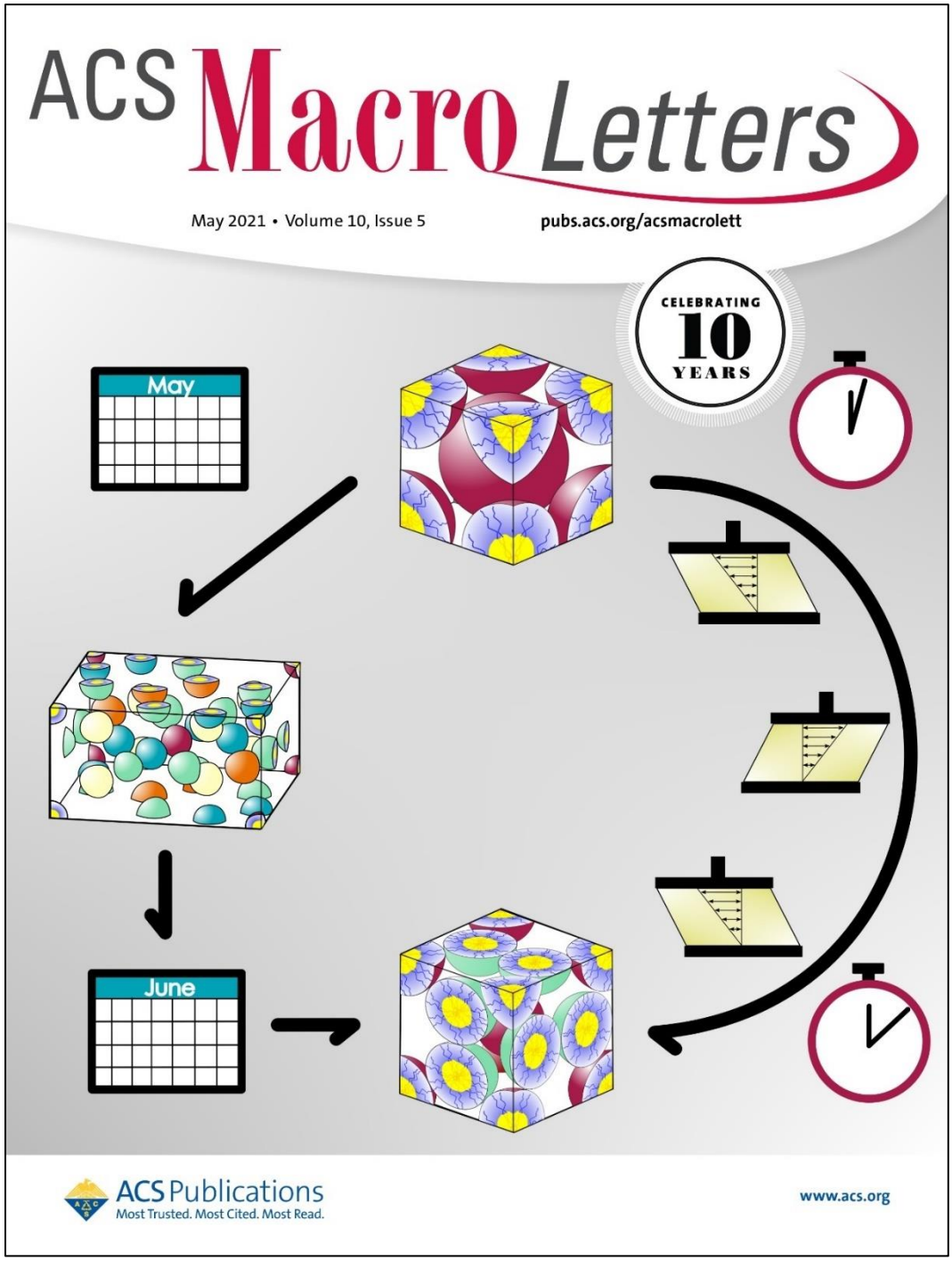

ACS Macro Letters cover page, May 2021. Drawn and composed by Connor Valentine.

"Shear-Modulated Rates of Phase Transitions in Sphere-Forming Diblock Oligomer Lyotropic Liquid Crystals". *ACS Macro Lett.* (2021) https://pubs.acs.org/doi/10.1021/acsmacrolett.1c00154

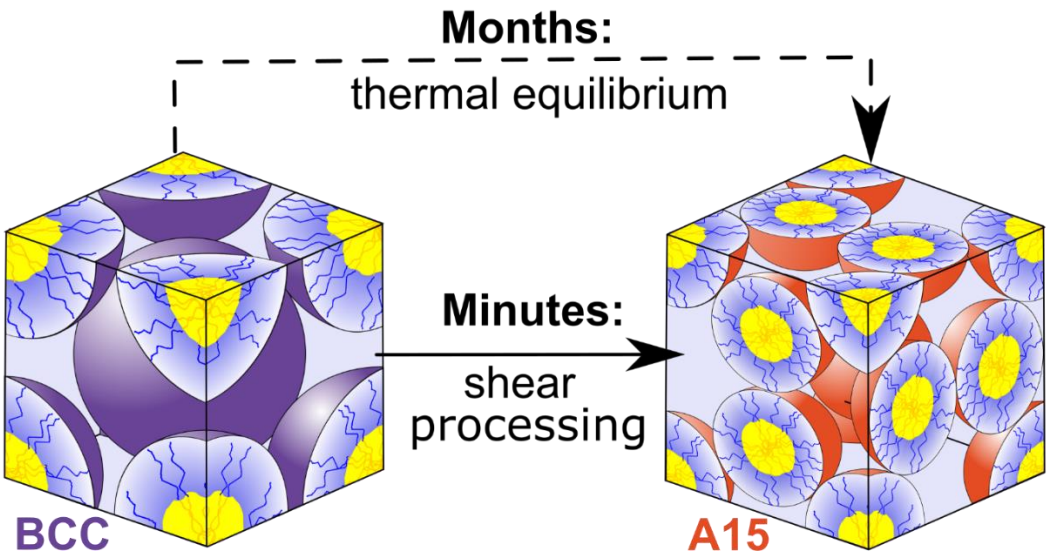

In this chapter, we demonstrate the impact of large amplitude oscillatory shear processing on phase transitions in a diblock polymer where the outer corona is composed of PEO. Included is a review of previous work summarizing the impact of shear processing on liquid crystalline phase alignment and crystalline size in block polymer systems. This is followed by our investigation of the impact of large amplitude shear processing on not just the phases and phase boundaries observed, but also the timescale of the phase transitions. To the best of our knowledge this is the first demonstration of shear processing to modulate the rate of phase transitions in solvent swollen block polymer crystalline systems. The comparison between metallic crystals and self-assembled polymeric crystalline phases

is often made. In contrast to metallic systems, polymeric systems demonstrate drastically lower moduli which facilitates shear processing. When formulators attempt to optimize the final macroscopic properties of materials with self-assembled crystalline structures, shear processing is a powerful tool that can be used to control the phases formed and the rate that the final phases formed. We present a methodology in this chapter which can accelerate certain phase transitions to occur within minutes rather than months.

Hydration of the amphiphilic diblock oligomer $C_{16}H_{33}(CH_2CH_2O)_{20}OH$ ($C_{16}E_{20}$) leads to concentration-dependent formation of micellar body-centered cubic (BCC) and Frank-Kasper A15 lyotropic liquid crystals (LLCs). Quiescent thermal annealing of aqueous LLCs comprising 56-59 wt% $C_{16}E_{20}$ at 25°C after quenching from high temperatures established their ability to form short-lived BCC phases, which transform into long-lived, transient Frank-Kasper σ phases *en route* to equilibrium A15 morphologies on a time scale of months. Here, the frequency and magnitude of applied oscillatory shear shows the potential to either dynamically stabilize the metastable BCC phase at low frequencies or increase the rate of formation of the A15 to minutes at high frequencies. Time-resolved synchrotron small-angle X-ray scattering (TR-SAXS) provides in situ characterization of the structures during shear and thermal processing. This chapter shows that the LLC phase and order-order phase transformation rates can be controlled by tuning the shear strain amplitude and frequency.

4.1 Shear Induced Alignment of Lamellar Phases

The orientation of lamellar phases in PS-*b*-PI diblock polymers in a neutral solvent dioctyl phthalate (DOP) has been studied via Rheo-SANS in a Couette cell.[66] Below the ODT, a shear induced lamellae was formed and oriented parallel to the shear cell walls via oscillatory shear. Steady shear aligned the lamellae parallel to the velocity gradient and direction. The alignment in these samples followed the reduced shear rate for the temperatures studied. The critical shear rate for alignment followed temperature exponentially.[66] In a similar PS-*b*-PI system the transition between lamellae parallel to the shear cell walls at high frequencies and parallel to the velocity gradient at low frequencies was accessed isothermally.[67] This behavior has been observed in the melt and solutions of PS-*b*-PI. At higher temperatures, steady shear induced less alignment than oscillatory shear perhaps due to a tendency to form defects during steady shear.[68] A study of lamellar phases in aqueous Pluronic P85 solutions showed that after steady shear, the lamellae were aligned in all orientations still parallel to the flow direction. This is a coexistence of layers parallel to the shear wall, and parallel to the velocity gradient.[69] For an extensive review of the rheological properties of the lamellar phase, refer to Berni and Lawrence, “A review of the rheology of the lamellar phase in surfactant systems”. Advances in Colloid and Interface Science 2002.[70]

4.2 Shear Effects on Crystals Composed of Spherical Micelles

Commonly seen cubic phases in concentrated block polymer solutions include hexagonally close-packed (HCP), face-centered cubic (FCC), and body-centered cubic (BCC). The influence of shear on the alignment of these phases has been well studied and reviewed.[36,71] Studies of a PS-*b*-PEP diblock in dodecane found that steady shear at low shear rates formed a distorted FCC phase with decreased distance between the close-packed {111} planes that was attributed to normal stresses. Two separate studies , one for a PS-*b*-PI and decane solution, and one for a polypropylene-polyethylene and water solution showed that steady shear induced a transition from polycrystalline FCC to sliding layers of HCP.[72,73]

The effect of large amplitude oscillatory shear (LAOS) was studied in an aqueous solution of Pluronic F108 using a couette cell.[74] Diat et al. investigated the effect of shear on the FCC phase in Pluronic F108. A twinned FCC structure with a high density of stacking faults was successfully annealed into an aligned single crystal of both twins separated by mm length scales. They found that steady shear oriented the most compact <111> layers parallel to the shear plane. The resulting crystal demonstrated a large amount of stacking faults that were subsequently annealed through oscillatory shear.[75] Later investigations revealed a shear rate dependent flow mechanism. At low shear rates intact FCC crystals flowed via grain boundaries, at intermediate shear rates (around 50 inverse seconds) HCP layers parallel to the Couette cell walls flowed via layer

sliding, and high shear rates induced shear melting. Creep experiments were used by Eiser, Molino and Porte to study the flow mechanisms starting from a polycrystalline FCC phase in aqueous F108.[76] Here it was found that flow starts at the nucleation of parallel HCP layers that facilitated sliding along closest packed layers.

Alignment of the BCC phase has been reported for several systems.[77,78] For oscillatory and steady shear. In a PS-*b*-PI decane solutions the twinned BCC structure was sheared into a distorted HCP structure before the twinned BCC was recovered again at higher shear rates ($\dot{\gamma} > 50\ s^{-1}$).[77] A common flow mechanism consists of a BCC crystal twinned along a {211} plane with the <111> direction along the shear direction and {110} planes in the shear plane. Flow occurs in the {211} planes due to slip along the twinning planes. A more complex version of this flow mechanism was presented to explain flow due to steady and oscillatory shear in an EO_{86}-*b*-BO_{10} in 0.2M K_2SO_4 system where the flow occurs in the {110}, {211}, and {321} planes that share the [111] zone axis.[79,80] This is consistent with the flow observed in metallic BCC structures.[78,81] These slip mechanism consist of planes sliding past each other. For BCC the slip direction is always the close-packed direction <111>. This is because the energy of dislocation is proportional to the square of the Burgers vector, since the <111> direction has the shortest burgers vector, dislocations along this axis will require the lowest stress.[78] The most common slip planes in BCC are the most densely packed {110} planes, which also are the most

widely separated. Higher shear stresses are required to produce slip in the {211} and {321} planes. This explains why the {110} <111> slip system is the most observed flow mechanism for BCC crystals.

Hamley et al. have compared the flow mechanisms in BCC and FCC structures under LAOS. The BCC systems were much more elastic and demonstrated hindered flow resulting from slip-stick motion. The FCC systems demonstrated unhindered sliding of HCP layers.[82] LAOS has also been used to study the nonlinear response in these systems via Lissajous figures. These results indicated shear thinning for an FCC structure in PEO-*b*-PB diblock solution. This has been associated with the formation of HCP layers that promote layer sliding and agrees with results from creep experiments on FCC.

A Study by Eiser and Molino compared the flow of a BCC phase (F68, EO_{76}-PO_{29}-EO_{76}) and an FCC phase (F108, EO_{127}-PO_{48}-EO_{127}).[25,78] Both systems reoriented under shear with their densest packed direction <111> parallel to the velocity. The BCC system demonstrated two distinct transitions in flow. The first transition occurred at lower shear rates ($\dot{\gamma} \sim 10\ s^{-1}$) as the BCC phase oriented from a disordered polycrystalline state to a twinned BCC crystal with the <111> direction parallel to the velocity and the {211} planes parallel to the shear plane.[78] The second transition at higher shear rates ($\dot{\gamma} \sim 100\ s^{-1}$) was observed as the crystal reoriented with the <111> direction parallel to the velocity and the {110} planes parallel to the shear plane. The FCC system showed a continuous

change with increasing shear. Additionally the BCC sample showed no measurable yield stress in contrast to the FCC sample which showed a yield stress will separate creep and flow regimes.[25]

4.3 Shear Effects on Hexagonally Packed Cylindrical Micelles

It has been found that hexagonally packed cylindrical micelles (H_1) will orient in the direction of shear in block polymer solutions.[83] We observe this ready transition to oriented cylinders in Brij-58 as well. Shear orientation in aqueous Pluronic L64 was found to be determined by strain and independent of the stress applied. Shear orientation by large amplitude oscillations on the H_1 in a system of EO_{18}-*b*-BO_{10} in 0.2 M K_2SO_4 was found to scale logarithmically with shear rate. Finally aqueous EO_{40}-*b*-BO_{10} H_1 phases were found to only orient under shear above 30 wt%.[83,84]

4.4 Effect of Shear Alignment on Rheological Moduli

Hamley, Pople, *et al.* studied the impact of alignment on ethyleneoxide-*b*-butyleneoxide blocks (EO_{40}-BO_{10}) in aqueous K_2SO_4 via rheo-SAXS. They showed that the moduli of the BCC and hexagonally packed cylindrical micelles are very weakly dependent on the alignment or size of the crystal grains.[1,85,86] Watanabe *eti al.* studied the impact of alignment on the modulus of a BCC lattice in polystyrene –*b*- polybutadiene and tetradecane solution. They found a minimal lowering of the storage modulus after alignment via steady shear.[87] Eiser and Molino demonstrated a similarly minimal impact on modulus when aligning Pluronic F68 (BCC) and Pluronic F108 (FCC) phases.[25]

4.5 A Note on Shear Banding in Liquid Crystalline Systems

In a review of shear-banding in complex fluids, Divoux states that the shear induced non-equilibrium structures seen in liquid crystalline phases are likely to involve shear banding.[70,88] The rheological signature of shear banding is a horizontal plateau in stress (σ) when measuring the flow curve, $\sigma(\dot{\gamma})$.[88] Holmqvist *et al.* used creep experiments to find a plateau in shear stress versus shear rate of a BCC forming diblock, $E_{315}B_{17}$, and water solution. They found that the flow behavior at shear rates above this plateau (high shear rates) was independent of shear history. However, when applying shear rates below the plateau (low shear rates) shear thinning was observed only in samples pre-aligned by high shear rates. Shear thickening was observed in samples pre-aligned by shear by low shear rates. This was attributed to enhanced packing of the micelles.[89] The plateau in the flow curve, $\sigma(\dot{\gamma})$ is only supportive of shear banding. To confirm shear banding one would need to perform local measurements of structure and flow field throughout the sample gap. Manneville provides a review of spatially resolved techniques for measurement of shear banding.[90]

In a Pluronic F68 (EO_{76}-PO_{29}-EO_{76}) 46 wt% solution Eiser *et al.* observed two separate stress plateaus in the flow curve during Rheo-SAXS using a Couette cell with a 1 mm gap and 10 mm diameter bob.[78] The first plateau was seen as the sample oriented from a disoriented polycrystalline BCC phase to a twinned BCC crystal with the <111> direction parallel to the velocity and the {211} planes parallel to the shear plane.[78] The second

plateau was observed as the crystal reoriented with the <111> direction parallel to the velocity and the {110} planes parallel to the shear plane. Due to the X-ray beams small cross section or ~150 μm compared to the 1 mm gap width, the authors were able to take spatially resolved structural data. A reproduction of the alignments seen is included in Figure 4.1. Due to the relatively large Couette cell gap width, the shear rate varies ~ 20% throughout the gap. As a result - the intermediate orientation (middle horizontal {110} planes) was only seen with the disoriented BCC (shaded right) and aligned orientation (left vertical {110} planes).

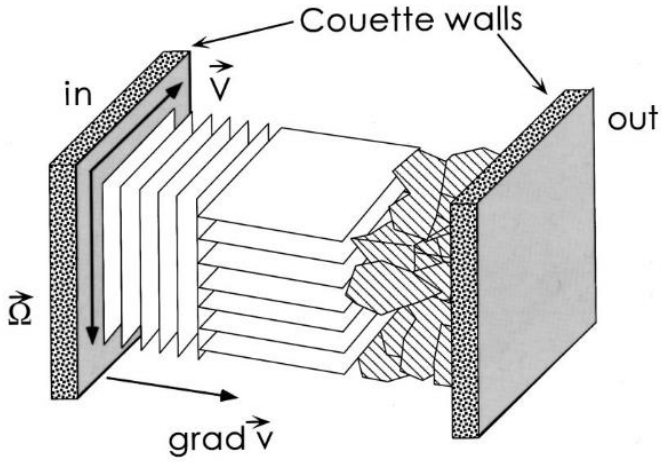

Figure 4.1: Schematic of three crystalline orientations coexisting at a shear rate of 50 s^{-1}. The parallel planes in the middle and on the left show the orientation of the dense {110} planes. Adapted from Eiser, Molino, and Porte, 2000.[78]

Another Study by Eiser and Molino compared the flow of a BCC phase (F68, EO_{76}-PO_{29}-EO_{76}) and an FCC phase (F108, EO_{127}-PO_{48}-EO_{127}).[25] Both systems reoriented under shear with their densest packed planes parallel to the velocity. The BCC system demonstrated distinct transitions as described earlier, while the FCC system showed a continuous change with increasing shear. Additionally the BCC sample showed no measurable yield stress in contrast to the FCC sample which showed a yield stress will separate creep and flow regimes.[25] Unfortunately the spatially resolved flow properties of concentrated polymer systems remains largely unexplored, and more work is required to understand the complicated shear-induced transitions.[88]

4.6 The Impact of Shear Processing on Frank-Kasper Phases in C_iE_j Diblock Polymers

Amphiphiles self-assemble in selective solvents to yield temperature and concentration dependent lyotropic liquid crystal (LLC) morphologies, including 1D lamellae, bicontinuous networks, hexagonally-packed cylindrical micelles (H_I), and ordered 3D packings of spherical micelles.[9,91,92] Typical micellar arrangements include high-symmetry body-centered cubic (BCC), face-centered cubic (FCC), and hexagonally closest-packed (HCP) phases.[93–97] Recent studies of aqueous LLCs of small amphiphiles have also revealed their ability to form lower symmetry packings known as Frank-Kasper (FK) phases.[98–101]Such complex micellar packings have also been observed in solventless thermotropic liquid crystals[15,102,103] and block polymer soft materials.[16,104–107] FK phases are characterized by large unit cells comprising ≥ 7 micelles of at least two different volumes.[108,109] For example, the FK A15 phase consists of two populations of quasispherical micelles where the aggregation number varies by ± 3% around a mean value.[65] Phase transitions amongst these complex structures have been induced by controlling thermal processing history under quiescent conditions, some of which mimic metallurgical processing procedures.[65,106,107]

Unlike metallic crystals, LLC phases of packed micelles can be easily manipulated at the micelle, lattice, and grain size length scales using relatively weak external forces. In these soft systems, shear is effective in enabling long-range structure and grain orientation refinement resulting in

pseudo-monodomain crystals of soft materials.[1,10,110–116] Shearing of ordered micellar phases results in micelle deformation, reorientation, and slipping along lattice planes to relieve stress accumulation in the structure.[117–119] Reports of the use of shear high shear rates ($\dot{\gamma}$ > 100 s^{-1}) to drive 'shear-induced melting' of ordered phases into disordered micellar fluids and modify order-to-order transitions (OOTs) of micellar materials have largely been limited to canonical BCC, FCC, and H_I phases.[110,113,120,121] Time-varying or oscillatory shear fields applied while cooling an aqueous lyotropic FCC phase of a poly(isoprene-*block*-ethylene oxide) diblock polymer enabled observation of transitions into structures exhibiting 12-fold and 18-fold rotational symmetries.[122] There are no reports of using shear to alter the rate of formation of a specific crystal phase. Herein, we show that the formation of the FK A15 phase can be sped up or entirely suppressed by tuning the frequency and strength of a simple oscillatory shear field.

Jayaraman *et al.* showed previously unrecognized aqueous LLC self-assembly behaviors of the nonionic diblock oligomer $C_{16}H_{33}(CH_2CH_2O)_{20}OH$ ($C_{16}E_{20}$ or Brij® 58).[65] With decreasing hydration, quiescent X-ray scattering analysis revealed that $C_{16}E_{20}$ exhibits the concentration-dependent phase sequence FCC ➞ BCC ➞ A15 ➞ H_I at 25 °C.[65] Different underlying micellar arrangements in these phases lead to subtle differences in their viscoelastic rheological signatures under oscillatory shear, as recently established for the FCC and BCC

morphologies.[23] Quiescent heating of the A15 phase formed between 56–59 wt% $C_{16}E_{20}$ in H_2O triggers an OOT into a BCC phase at 57°C, which transforms into a H_I phase at 70 °C. Subsequent quenching of the H_I phase to 25 °C results in an initial OOT to a non-equilibrium BCC phase that exhibits a broad SAXS signature that is different from that of the high temperature BCC phase. Subsequent isothermal annealing of this quenched sample at 25 °C leads to the nucleation and growth of a FK σ phase within 1 h. Extended annealing of the well-developed σ phase at 25°C results in slow nucleation of the equilibrium A15 phase after several days with complete transformation after 5 months. The slow BCC → σ → A15 transition in this system provides an opportunity to quantify the impact of shear processing, specifically, the frequency and strength of an oscillatory shear field on OOT kinetics.

In this work, we apply a well-defined oscillatory shear, $\gamma(f,t) = \gamma_o \, sin(2\pi f t)$, as a canonical shear deformation. Use of an oscillatory deformation facilitates control of both the frequency, *f*, and the strength, γ_o, of the deformation while limiting the chances of tearing or gross failure of the sample. We use this well-defined deformation to modulate the kinetics of the isothermal BCC → σ → A15 transition at 25 °C in aqueous $C_{16}E_{20}$ samples in the narrow 57−59 wt% amphiphile composition range. Time-resolved synchrotron small-angle X-ray scattering (TR-SAXS) is used to collect structural information every 5 s with an X-ray exposure time of 0.1 s while oscillatory shear is applied using a parallel-plate shear cell. The

strains applied are sufficiently greater than the linear plateau in moduli observed during strain amplitude sweeps per our previous work with $C_{16}E_{20}$.[23] While oscillatory shear flow is a central pillar of rheometric studies, we do not use the deformation to extract mechanical behavior or material properties; the linearity or nonlinearity of the constitutive behavior is not a focus of this work. Shear is applied only as a well-controlled deformation. All samples are initially heated to 70°C for 1 min to induce H_I phase formation and subsequently cooled to 25°C at a rate of 30°C/min. Immediately upon cooling to 25°C a BCC phase is observed. After equilibration at 25°C for 5 min, oscillatory shear is initiated.

4.7 Materials and Methods – Time Resolved Synchrotron SAXS with *in-situ* large amplitude oscillatory shear

Commercially available Brij 58® ($C_{16}E_{20}$) (*n*-$C_{16}H_{33}(OCH_2CH_2)_{20}$-OH) from Millipore-Sigma (Milwaukee, WI, U.S.A.) was used as received. Samples were mixed with ultrapure water (18 MΩ●cm) and homogenized with three cycles of hand-mixing and centrifugation (4950g, 10 min).

SAXS measurements were performed at the 12-ID-B beamline of the Advanced Photon Source at Argonne National Lab (Argonne, IL, U.S.A.). An incident beam energy of 13.3 keV (λ = 0.932 Å) was used with a sample to detector distance of 3.618 meters to acquire 2D-SAXS patterns on a Pilatus 2M detector with 172 μm x 172 μm pixel resolution. SAXS patterns are acquired every 5 s (10 s in the γ = 0% control experiments) with typical exposure times of 0.1 s. The wavevector, $q = (4\pi \sin(\theta/2)/\lambda)$, was calibrated with a silver behenate standard. Acquired 2D-SAXS traces were azimuthally integrated using the Datasqueeze software package to yield 1D-SAXS $I(q)$ vs q patterns, (https://www.physics.upenn.edu/~heiney/datasqueeze/index.html).

To obtain *in-situ* X-ray scattering under oscillatory shear, samples were loaded via spatula into a Linkam CSS-450 Optical Shear Stage equipped with Kapton windows and set to a 400 μm gap. The shear cell was mounted with the X-ray beam parallel to the shear gradient direction. Each side of the cell is electrically heated and cooled with gas boil off from a liquid nitrogen reservoir. Three frequencies of shear were investigated: high

frequency (9.9 Hz, 63 rad/s), intermediate frequency (1 Hz, 6.3 rad/s), and low frequency (0.1 Hz, 0.63 rad/s). Due to instrument limitations, the range of accessible shear strains at each frequency were limited. The high frequency oscillations were applied with shear strains in the range of γ = 3.54-177% strain. The intermediate and low frequency oscillations were applied with shear strains in the range of γ = 177-1,770% strain. During sinusoidal oscillatory shear the applied strain, $\gamma(t)$, is equal to: $\gamma(t) = \gamma \sin(\omega t)$, where $\omega = 2\pi f$. The strain rate, $\dot{\gamma}(t)$, is the derivative of strain with respect to time, $\dot{\gamma}(t) = \gamma\omega \cos(\omega t)$. The maximum strain rate applied during oscillatory shear, $\dot{\gamma}$, is equal to $\gamma\omega$.

Peak finding and data analysis of the 1-D SAXS profiles was performed using MATLAB in a rigorous multistep process. First, all peaks in every data file were found using the built-in function, findpeaks(). The minimum peak prominence was set to 0.75 and minimum peak spacing set to 0.001. Second, any peak that fell into the expected *q*-range for (200) peak of BCC or A15 were set aside as “target peaks” for each phase. Third, a final optimization was performed before these “target peaks” were identified the (200) peak of BCC or A15. For every single data frame ($I(q)$ v. q), the entire set of peaks found using MATLAB’s findpeaks() were fed into a function that calculated the least squared error between this set of peaks and the reference spacing for BCC or A15. Using the “target peak” as the anchor for this search, we were able to concretely establish the presence of either phase in every single data frame, including frames with both

phases present. All figures in this manuscript with peak locations overlaid used this method to add the vertical lines and symbols identifying peak locations. Finally, we manually confirmed that this protocol correctly identified BCC(200) and A15(200) peaks in each data frame.

The intensity of the (200) peak of the BCC phase located at q = 0.135 ± 0.001 $Å^{-1}$ (I_{200}(BCC)) and the intensity of the (200) peak for the A15 phase at q = 0.084 ± 0.001 $Å^{-1}$ (I_{200}(A15)) were used to quantify the transition from BCC to A15. At 25 °C and the small concentration window tested, there was no significant change in these peak positions (q ($Å^{-1}$)) during or after the application of oscillatory shear. This is demonstrated by the low standard deviation in the peak locations across nearly 4000 SAXS patterns obtained from the A15 and BCC structures under the complete range of oscillatory shear conditions tested.

The kinetics of phase change in block polymer crystals has been interpreted using Mehl-Johnson-Avrami (MJA) nucleation theory.[123–126] In this study we used a simplified Avrami model to parameterize the kinetics of the transition from BCC to A15 under isothermal oscillatory shear at 25°C by tracking the time-evolution of I_{200}(A15) as $I(t) - I(t_0) = [I(t_\infty) - I(t_0)]\,(1 - e^{-k(t-t_0)^n})$. A characteristic timescale that arises from the MJA fit is $\tau = k^{-(1/n)}$.

The phase transformation rate constant, k, and the Avrami exponent, n, are calculated by fitting the Avrami model to the time-dependent I_{200}(A15) derived from TR-SAXS with the constraint that $1 \leq n \leq 4$. Here t_0 is taken as

the time when shear is initiated, and t_∞ is taken as the time when shear is ceased. TR-SAXS patterns were acquired during the application of oscillatory shear for at least 20 min. In the cases where oscillatory shear was applied for longer times (Figures 4.9, 4.16, and 4.17), Avrami fit parameters show no significant changes when fit to only the first 20 min of shear. While this equation can be used to classify not only the rate of crystal growth but also the mechanism, we focus solely on the rate of A15 crystal growth. This parameterization allows quantitative comparison of the effect of shear on lyotropic liquid crystal growth between trials.

Included below is the thermal annealing procedure that was applied to every sample after loading into the shear cell, prior to TR-SAXS analysis. Each sample was first heated to 70 °C and annealed there for 1 min to ensure complete transition to the H_I phase. Samples were then cooled to 25 °C at 30 °C/min, followed by 5 min of thermal equilibration. After this 5 min equilibration period, oscillatory shear was started at t = 0 min. This annealing procedure provides a consistent starting BCC structure prior to application of oscillatory shear.

4.8 Shear Induced Acceleration of the BCC to A15 transition

Figure 4.2 shows the impact of shear at a frequency f = 1.0 Hz and strain amplitude γ = 1770% on the BCC to A15 phase transition at 25 °C. Before shear is initiated (t < 0 min), the sample forms a BCC phase with unit cell parameter a_{BCC} = 9.3 nm as evidenced by the SAXS maxima at $(q/q^*)^2$ = 1,2,3... (Figure 4.2a, *purple circles*). The quiescent thermal equilibration continues at 25 °C until t = 0 min, when oscillatory shear is initiated. After one minute of shear (t > 1 min), the BCC reflections are entirely absent from the SAXS data and they are replaced with the somewhat broad (110), (200), (210), and (211) reflections of the A15 phase (Figure 4.2a). Red triangles denote the calculated positions of the first eleven A15 peaks with unit cell parameter a_{A15} = 14.9 nm. Continued application of shear results in intensified and narrowed SAXS peaks, which indicates grain size coarsening.[127] The isothermal BCC to A15 transition is monitored under shear by tracking the intensity of the (200) SAXS peak for each of the two phases. The (200) peaks were selected due to minimal overlap with other peaks and their equal reflection multiplicities. Standard peak fitting algorithms were used to extract peak locations and intensities in MATLAB as defined in the methods section.

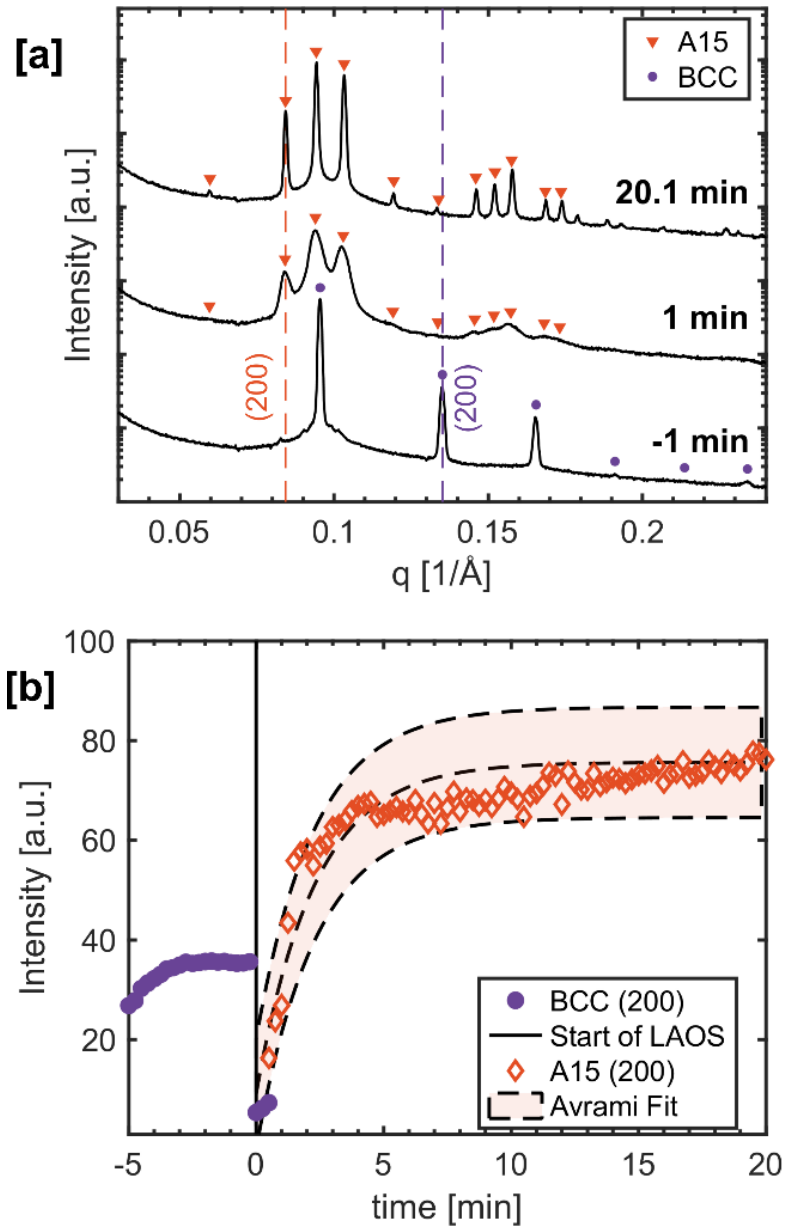

Figure 4.2: [a] 1D-SAXS profiles at time points before and during oscillatory shear (f = 1.0 Hz, γ = 1770%), initiated at t = 0 min. Calculated peak positions for BCC with unit cell parameter a_{BCC} = 9.3 nm (*purple circles*) and A15 with lattice parameter a_{A15} = 14.9 nm (*red triangles*) are overlaid. **[b]** Time-evolution of I_{200}(BCC) and I_{200}(A15) before and during shear. I_{200}(A15) data are fit to the Mehl-Johnson-Avrami (MJA) equation and shown with shaded 95% confidence intervals. Every third data point is shown for clarity.

The time-evolution of I_{200} is shown for each phase in Figure 4.2b. Mehl-Johnson-Avrami (MJA) nucleation theory[123–126] offers a natural framework for quantifying the kinetics of the isothermal oscillatory shear modulated BCC ➞ A15 OOTs across a range of shear conditions. We specifically modeled the time evolution of the peak intensity I_{200}(A15) derived from TR-SAXS analyses using the simplified MJA model,

$$I(t) - I(t_0) = [I(t_\infty) - I(t_0)]\,(1 - e^{-k(t-t_0)^n}),$$

where $I(t_0)$ and $I(t_\infty)$ are the intensities of the A15 (200) peak at initiation (t = 0 min) and upon cessation of shear ($t = 20\ \mathrm{min}$). k is the phase transformation rate constant and from this model, and $\tau = k^{-(1/n)}$ is a characteristic phase transformation time scale. For the purposes of this letter, we primarily seek to use this model to parameterize the kinetics of the isothermal BCC ➞ A15 transition under shear processing. The A15 phase formation is captured well by the MJA fit, shown with shaded 95% confidence intervals throughout the chapter.

The rapid and direct, shear-induced transition from BCC ➞ A15 significantly differs from the slower, indirect BCC ➞ σ ➞ A15 transition sequence observed during quiescent isothermal annealing.[65] In the latter report, signatures of the A15 phase emerge only after several days with the complete phase transformation after 150 days at 25 °C. We note that those quiescent phase behavior studies employed small samples enclosed in metal pans that were cooled by immersion into a temperature-controlled water bath. To understand whether the cooling rate and geometry of the

parallel-plate shear cell used in our TR-SAXS studies influenced the OOT pathways and kinetics, we performed a control experiment where no shear is applied at t = 0 min after the thermal annealing procedure outlined above (Figure 4.3). TR-SAXS analyses of this quiescent sample reveal somewhat slower σ phase nucleation kinetics, which we ascribe to slight differences in sample cooling rate and composition. Despite these small differences, our control experiment provides baseline kinetics to establish that oscillatory shear suppresses σ phase formation and triggers an accelerated BCC → A15 OOT within minutes rather than months in comparison to quiescent thermal annealing.

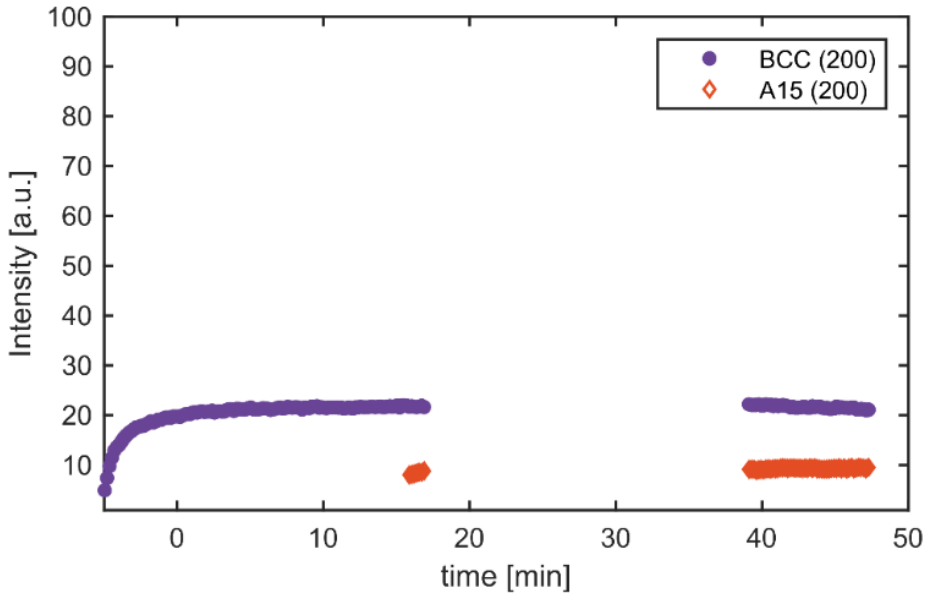

Figure 4.3: I_{200}(BCC) (*purple circles*) and I_{200}(A15) (*red diamonds*) as a function of time, after the thermal quench procedure outlined above. The results concur with those reported by Jayaraman et al.[65] Data is shifted so that t = 0 min corresponds to the time in the thermal annealing procedure when oscillatory shear would normally be applied. Between t = 18 min and t = 39 min, x-ray exposure was stopped, and no data was collected to prevent sample degradation.

4.9 Shear Modulation of the BCC to A15 Transition – A Tunable Timescale from Months to Minutes

To explore the impact of shear processing, we demonstrate the effect of strain amplitude, γ_o, on the BCC → σ → A15 transition under shear of the same frequency, f = 1.0 Hz (Figure 4.4a). The time-evolution of I_{200} is shown for each phase, with the resulting MJA fit shown for I_{200}(A15) in Figure 4.4a. As strain amplitude is decreased by an order of magnitude from 1770% to 177%, the rate of A15 formation slows (see Figures 4.11-4.13 for full time-resolved profiles). Figure 4.4b shows the 1D-SAXS traces obtained at t = 20 min of oscillatory shear under these conditions. Results of the quiescent control experiment where no shear is applied for approximately 20 min (Figure 4.3) are included for comparison. The BCC peaks for the control experiment appear at slightly lower q values as the sample was at the lower end of the concentration window (57-59 wt%), corresponding to an incremental change in a_{BCC} = 9.3 to a_{BCC} = 9.5 nm. An increase in the BCC unit cell size with decreasing $C_{16}E_{20}$ concentration has been previously reported in this system.[65] Peaks that are not labeled with markers for the calculated A15 or BCC peak positions correspond to the σ phase, which is the expected intermediate structure.[65] Increasing γ_o at this frequency increases the rate of A15 formation, decreases the intensity of residual σ and BCC reflections, and leads to larger grain sizes after 20 minutes of shear as shown by qualitatively sharper SAXS peaks in Figure 4.4b. Similar

trends are observed for shear experiments conducted at a higher frequency f = 9.9 Hz with 3.54% ≤ γ_o ≤ 177% (Figures 4.14 - 4.17).

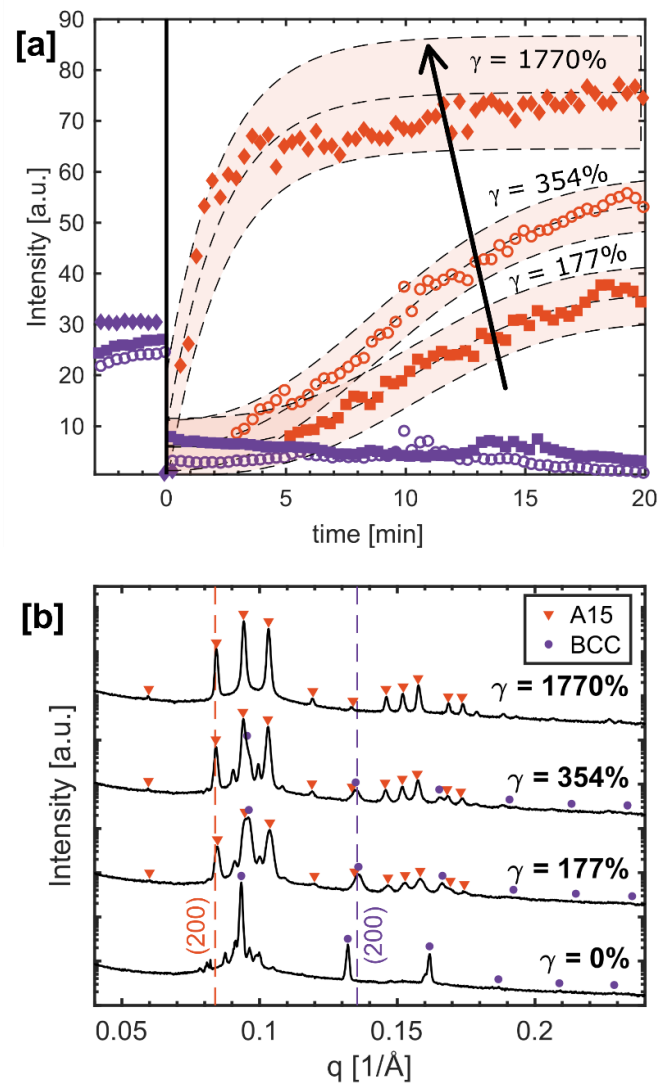

Figure 4.4: [a] Time-evolution of I_{200}(BCC) and I_{200}(A15) for three separate shear trials, demonstrating the effect of strain amplitude at f = 1.0 Hz. Oscillatory shear is initiated at t = 0 min. BCC data (*purple*) and A15 data (*red*) share the same symbol shape at each strain amplitude. I_{200}(A15) data are fit the Mehl-Johnson-Avrami (MJA) equation and shown with shaded 95% confidence intervals. Every fourth data point shown for clarity, see Figures 4.11 - 4.13 for complete profiles. **[b]** 1D-SAXS profiles at t = 20 min of oscillatory shear, compared to the control case where no shear is applied for ~20 minutes. Calculated peak positions for BCC (*purple circles*) and A15 (*red triangles*) are overlaid.

Lowering the frequency of the deformation to 0.1 Hz drastically changes the dependence of the BCC ⟶ A15 transition kinetics on applied strain amplitude in the range 177 ≤ γ_o ≤ 1770% (Figures 4.5). In contrast to the observations at 1.0 Hz (Figure 4.4) and 9.9 Hz (Figures 4.14 - 4.17), increasing the strain amplitude decreases the rate of A15 formation. Remarkably, the highest strain amplitude oscillatory shear applied at 0.1 Hz suppresses the formation of both A15 and σ for the duration of the experiment. At the end of the 20 min oscillatory shear process, only two low intensity SAXS maxima are visible near the expected *q*-values for the (200) and (211) reflections (second and fourth SAXS peaks) of the A15 phase in Figure 4.5b. In this case, slow growth of the A15 phase prevents a reliable MJA fit. However, it is evident that the timescale of A15 formation under these conditions is significantly longer than the other oscillatory shear conditions tested (τ > 100 min).

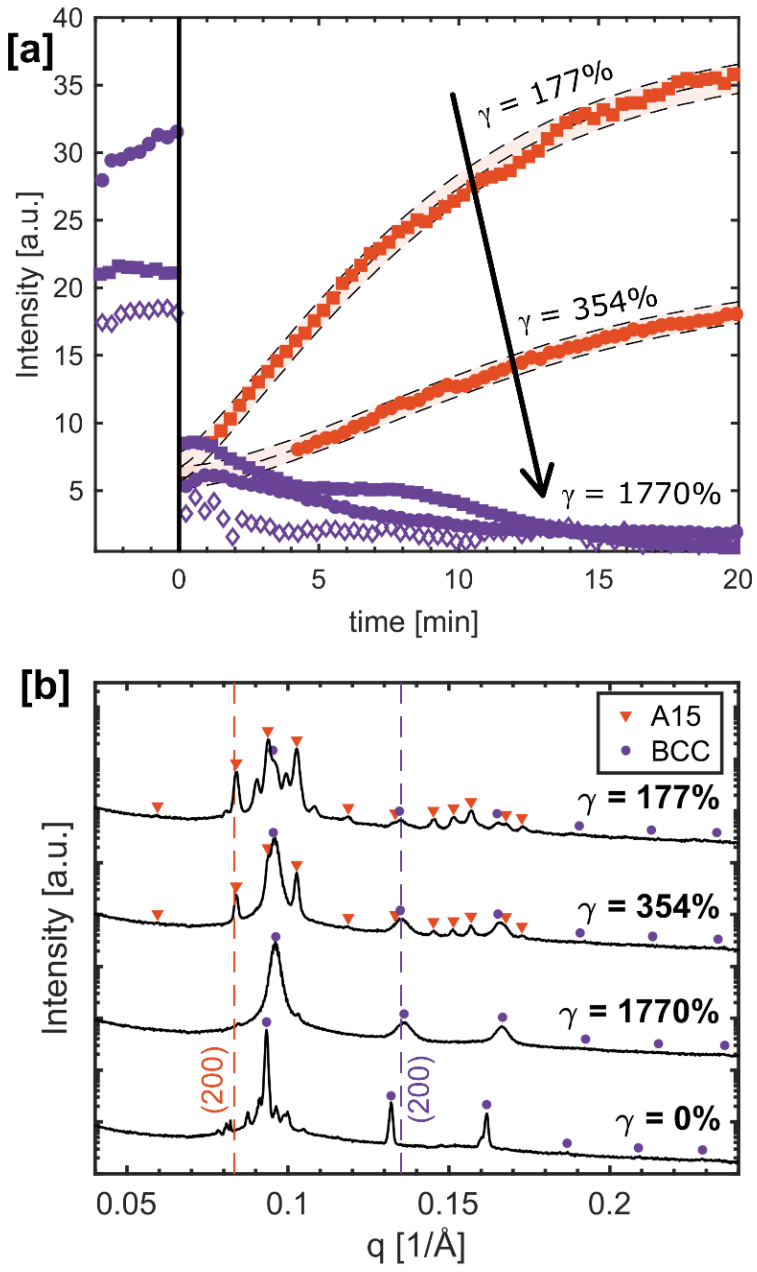

Figure 4.5: [a] Time-evolution of I_{200}(BCC) and I_{200}(A15) for three separate shear trials, demonstrating the effect of strain amplitude at f = 0.1 Hz. Oscillatory shear is initiated at t = 0 min. BCC data (*purple*) and A15 data (*red*) share the same symbol shape at each strain amplitude. I_{200}(A15) data are fit the Mehl-Johnson-Avrami (MJA) equation and shown with shaded 95% confidence intervals. Every fourth data point shown for clarity, see Figures 4.8 - 4.10 for complete profiles. **[b]** 1D-SAXS profiles at t = 20 min of shear, compared to the control case where no shear is applied for ~20 min. Calculated peak positions for BCC (*purple circles*) and A15 (*red triangles*) are overlaid.

The timescale for A15 formation (τ) which results from the MJA fits to each oscillatory shear experiment are shown in Figure 4.7 (see Figure 4.6 for associated model fits of *k* and *n*). Error bars are shown and are typically smaller than the size of the markers. For both *f* = 1.0 and 9.9 Hz (*filled symbols*) τ monotonically decreases with increasing strain amplitude, indicating an acceleration of the BCC to A15 transition. A different trend holds at *f* = 0.1 Hz (*open purple symbols*). At this low frequency, increasing strain amplitude slows the kinetics of the BCC → A15 transition such that the slow growth kinetics at γ_o = 1770% prevent reliable extraction of MJA fit parameters. Under these low frequency and high strain amplitude conditions, τ is evidently much longer than every other shear condition tested (indicated by the purple arrow) and may even be longer than the quiescent case.

Finally, we use the maximum shear rate applied during oscillatory shear ($\dot{\gamma} = 2\pi f\gamma_o$) to clarify trends in the timescale of A15 formation (τ) between low, intermediate, and high frequency trials (Figure 4.7b). The maximum shear rate during oscillatory shear represents the rate at which deformations to the sample are applied at the peak of the sinusoidal oscillation cycle. By replotting the data in Figure 4.7a using this reduced form that incorporates both γ_o and *f*, we find that increasing $\dot{\gamma}$ during oscillatory shear decreases τ for A15 formation *only* when the frequency of oscillation is sufficiently rapid (*f* = 1.0 and 9.9 Hz, *filled symbols*). These data follow a simple power-law scaling with an exponent of -0.57 ± 0.18, as

indicated by the linear fit of the log-log plot, suggesting a scaling with rate or timescale or deformation rather than strain. However, the data collected at f = 0.1 Hz (*open purple symbols*) do not follow this trend: instead, increasing the effective shear rate of a low frequency oscillation results in a drastic increase in τ. The purple arrow on Figure 4.7b again indicates the f = 0.1 Hz and γ_o = 1770% oscillatory shear condition that resulted in nearly complete A15 suppression.

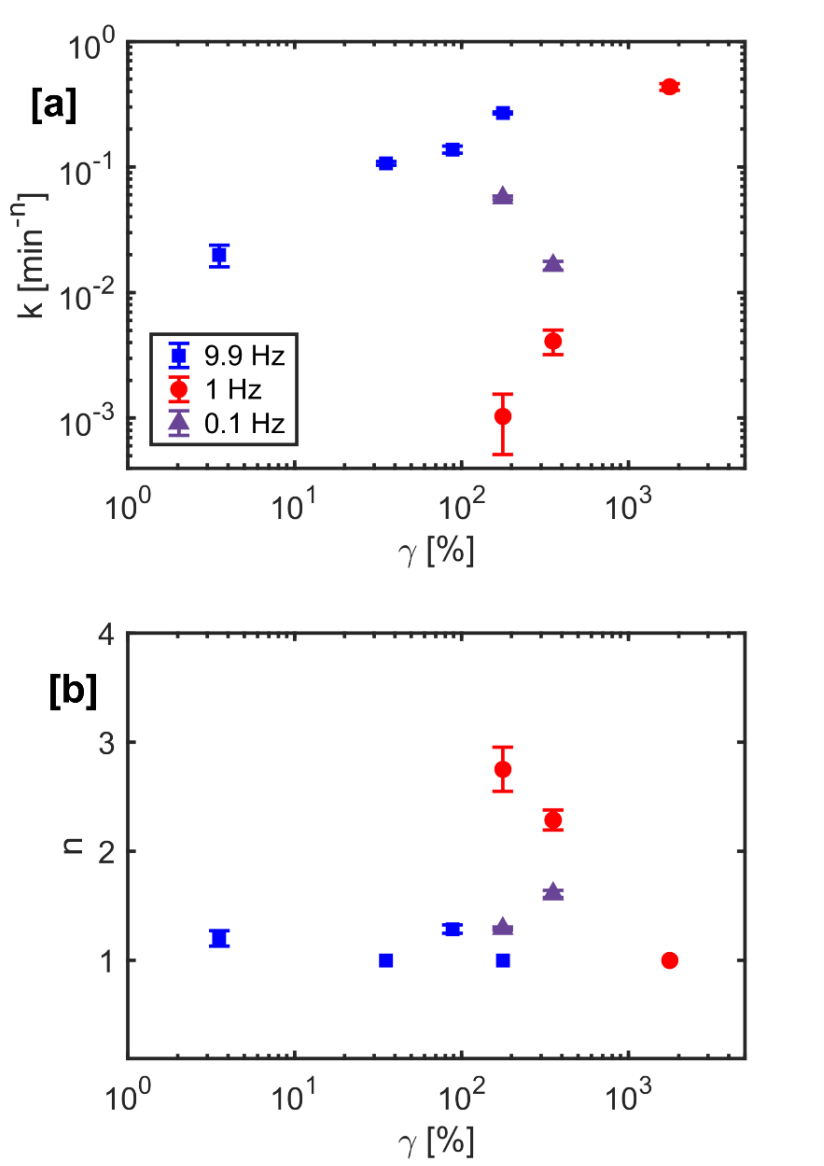

Figure 4.6: [a] The phase transformation rate constant, *k*, and **[b]** the Avrami exponent, *n*, from the MJA model fit for each oscillatory shear condition with *f* = 9.9 Hz (*blue squares*), 1.0 Hz (*red circles*), and 0.1 Hz (*purple triangles*). These parameters are used to calculate (τ) in Figure 4.7.

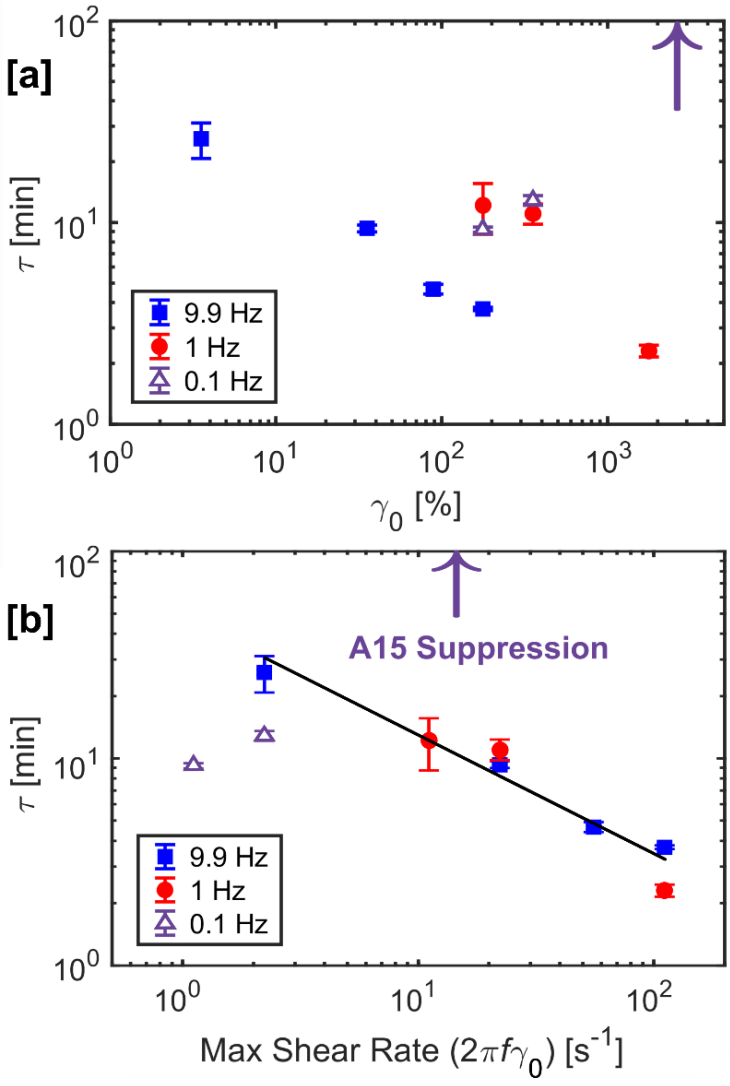

Figure 4.7: [a] The timescale for A15 formation (τ) from the MJA model versus applied γ_0 for each shear condition with f = 9.9 Hz (*filled blue squares*), 1.0 Hz (*filled red circles*), and 0.1 Hz (*open purple triangles*). A purple arrow denotes that τ is dramatically longer than 100 min when γ_0 = 1770% and f = 0.1 Hz. In most cases, the calculated error bars are smaller than the size of the markers. **[b]** Trends in τ with *maximum shear rate* during oscillatory shear deformation. The maximum shear rate during oscillatory shear is proportional to the frequency multiplied by the strain amplitude. A simple power-law scaling with an exponent of -0.57 ± 0.18 is fit to data of intermediate and high frequency (*filled symbols*)

The BCC → σ → A15 transition has been argued to stem from a combination of intermicellar chain exchange to achieve the prerequisite aggregation number distribution with minimal interfacial area for phase formation and micelle diffusion to appropriate symmetry-equivalent positions in the lattice.[98,108,128] For example, in 58.9 wt% $C_{16}E_{20}$ the average aggregation number (N_{AGG}) for the A15 phase is ~ 128.2, while for BCC, N_{AGG} ~ 123.2.[65] The small difference in aggregation numbers is achieved through intermicellar chain exchange in the quiescent case. However, the results presented here suggest that macroscopic deformation during shear alters or even suppresses the nanoscale mechanisms that mediate these phase transitions. If the BCC phase were replaced directly by the A15 phase via chain exchange and micelle diffusion, we expect an Avrami-style fit to capture the growth of the A15 phase as well as the reduction of the BCC phase as seen in quiescent thermal annealing studies.[123] Instead we observe a large, almost instantaneous decrease in intensity of BCC peaks upon initiation of shear, followed by a slow increase in the magnitude of peaks corresponding to the A15 structure. Chain exchange and micelle diffusion alone cannot account for this observation. We speculate that the non-linear strain applied during oscillatory shear immediately breaks the metastable BCC phase to possibly yield a poorly ordered micellar arrangement, which falls into the equilibrium A15 arrangement with minimal corona overlap.[129,130] Subsequent application of high frequency shear facilitates intermicellar collisions and chain exchange[120] to equilibrate the

micelle aggregation numbers to achieve minimal interfacial area, enabling nucleation and growth of a well-ordered, equilibrium A15 structure from the poorly-ordered intermediate micellar phase.

Sufficiently high frequency shear-induced spatial displacement of the micelles coupled with accelerated chain exchanged likely drives the approach to the equilibrium A15 phase from the metastable BCC phase. The cause of the *decrease* in rate and even suppression of A15 nucleation observed during low frequency oscillations is not clear. A possible explanation stems from the realization that low frequency oscillatory flow approaches steady state, unidirectional flow, especially at these large amplitudes. For steady shear flow ($f \rightarrow 0$), the mechanism could shift to one in which the crystalline planes slip and yield to alleviate accumulated stress in the structure. The high-symmetry BCC structure with 12 independent lattice slip systems does provide more efficient pathways for energy dissipation as compared to 3 independent slip systems that characterize the relatively less ductile A15 phase.[131,132] Hence, nucleation of complex FK structures is delayed under conditions approaching steady shear achieved only at the lowest frequency and highest strain applied in this work. The observed (albeit slow) formation of the A15 structure upon cessation of the shear under these last conditions corroborates this hypothesis.

4.10 Conclusions

In summary, we have demonstrated that shear processing of aqueous LLCs of $C_{16}E_{20}$ enables control over the kinetics of the metastable BCC ⟶ equilibrium A15 phase transition at 25°C. Shear processing accelerates the phase transition from BCC ⟶ A15 by several orders of magnitude as compared to the quiescent case. At f = 1 and 9.9 Hz, increasing the shear rate increases the rate of A15 formation. In contrast, at the lowest applied frequency 0.1 Hz, increasing the shear rate slows the rate of A15 formation. Combining a low f with a high γ_o entirely arrests the BCC structure, rendering the timescale for A15 formation immeasurable within the resolution of our TR-SAXS experiments. In all cases, increasing the strain amplitude at a given frequency decreases the observed intensities of any intermediate σ phase reflections remaining after 20 min.

These results illustrate that shear processing can be used to control the rates of order-order phase transformations in self-assembled soft materials that are otherwise slow under quiescent thermal annealing conditions. The shear-modulated control of these various transformations likely stems from complex changes in the frequencies of interparticle collisions, micelle rearrangements with minimal coronal overlap, intermicellar chain exchange, and activation of slip systems within the polycrystalline domains of the material. These findings illustrate the potential for shear processing to control the rates of phase transitions in self-assembled structures in soft matter, which will inform the formulation

and processing of aqueous dispersions of oligomeric and polymeric surfactants at high solids contents.

4.11 Auxiliary Data for Chapter 4

Included in this section are complete 1-D TR-SAXS profiles and corresponding fits to the MJA model. In Figures 4.8 - 4.10 the oscillatory shear frequency is set to 0.1 Hz.

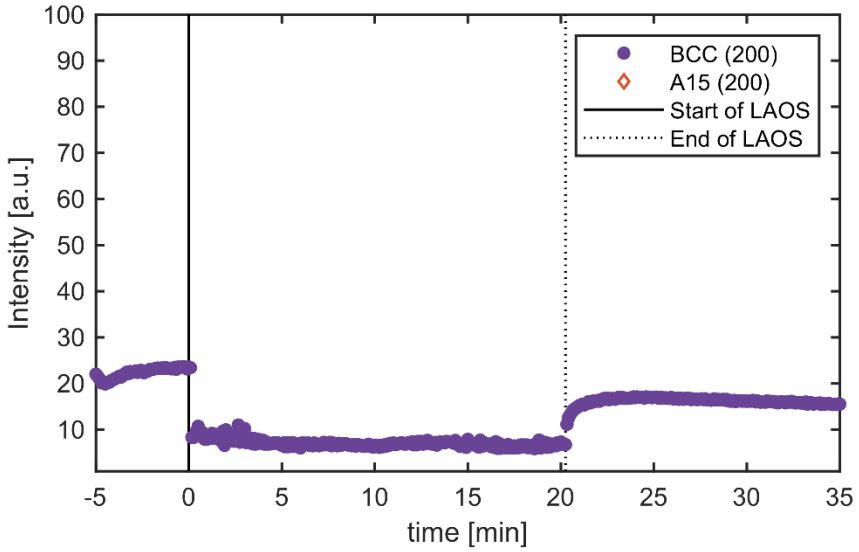

Figure 4.8: I_{200}(BCC) (*purple circles*) and I_{200}(A15) (*red diamonds*) as a function of time, where the solid black vertical line indicates the start of oscillatory shear with f = 0.1 Hz, γ = 1770%. A fit to the MJA model was not possible due to slow A15 growth kinetics at these conditions. Dashed vertical line indicates the cessation of shear.

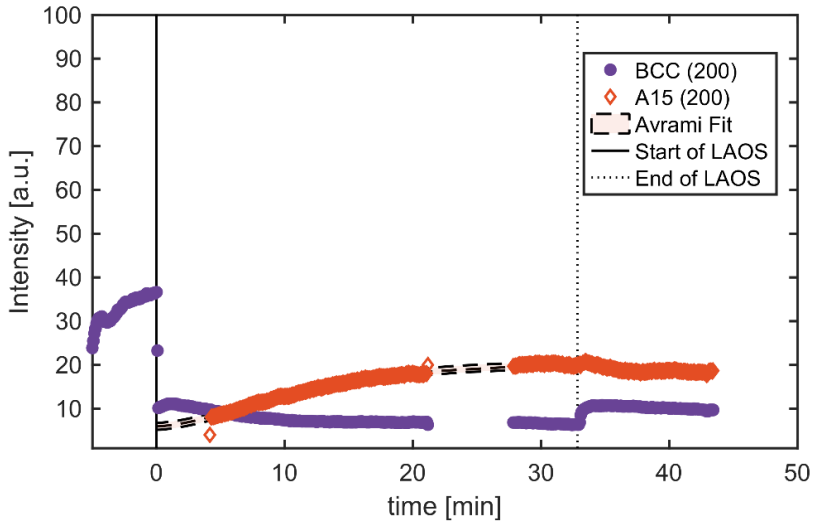

Figure 4.9: I_{200}(BCC) (*purple circles*) and I_{200}(A15) (*red diamonds*) as a function of time, where the solid black vertical line is start of oscillatory shear with f = 0.1 Hz, γ = 354%. A fit to the MJA model is shown as dashed black lines for the data acquired during shear, with the 95% confidence region shaded. Dashed vertical line shows the cessation of shear. The Avrami fit parameters show no significant deviation when fit to only the first 20 min of shear.

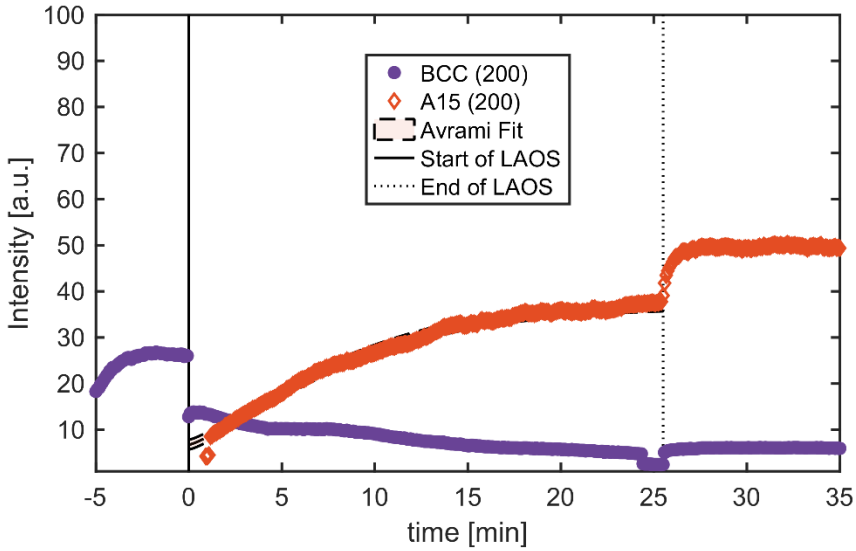

Figure 4.10: I_{200}(BCC) (*purple circles*) and I_{200}(A15) (*red diamonds*) as a function of time, where the solid, black vertical line indicates the start of oscillatory shear with f = 0.1 Hz, γ = 177%. A fit to the MJA equation is shown as dashed black lines for the data acquired during shear, with the 95% confidence region shaded. Dashed vertical line indicates the cessation of shear.

Included in Figures 4.11 - 4.13 are complete 1-D TR-SAXS profiles and corresponding fits to the MJA model, with the oscillatory shear frequency set to 1 Hz.

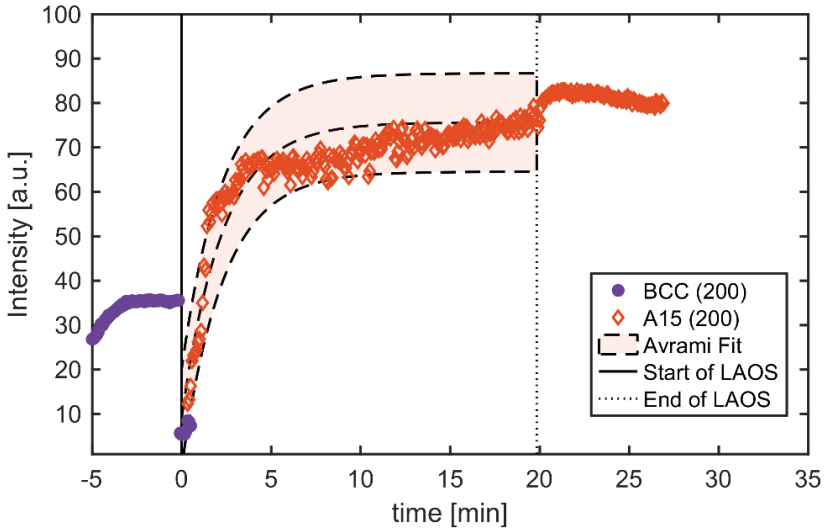

Figure 4.11: I_{200}(BCC) (*purple circles*) and I_{200}(A15) (*red diamonds*) as a function of time, where the solid vertical line indicates the start of oscillatory shear with f = 1 Hz, γ = 1770%. A fit to the MJA equation is shown as dashed black lines for the data acquired during shear, with the 95% confidence region shaded. Dashed vertical line indicates the cessation of shear.

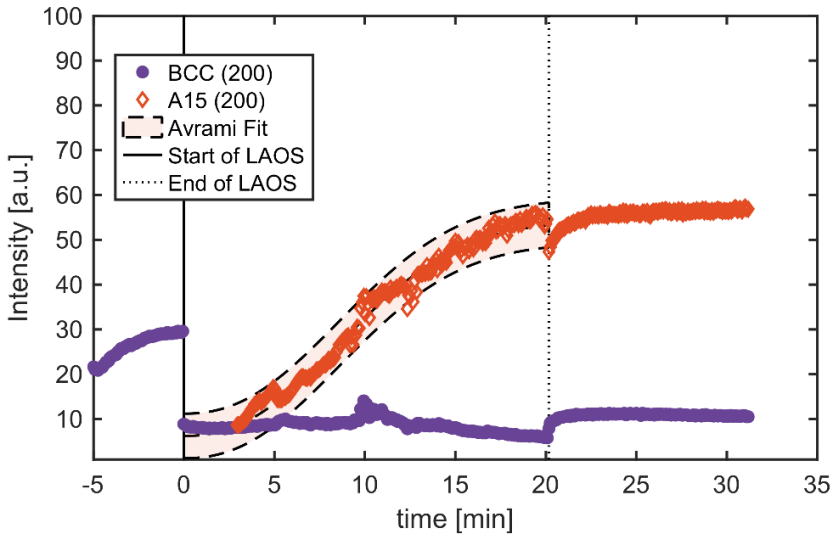

Figure 4.12: I_{200}(BCC) (*purple circles*) and I_{200}(A15) (*red diamonds*) as a function of time, where the solid vertical line indicates the start of oscillatory shear with f = 1 Hz, γ = 354%. A fit to the MJA model is shown as dashed black lines for the data acquired during shear, with the 95% confidence region shaded. The dashed vertical line indicates the cessation of shear.

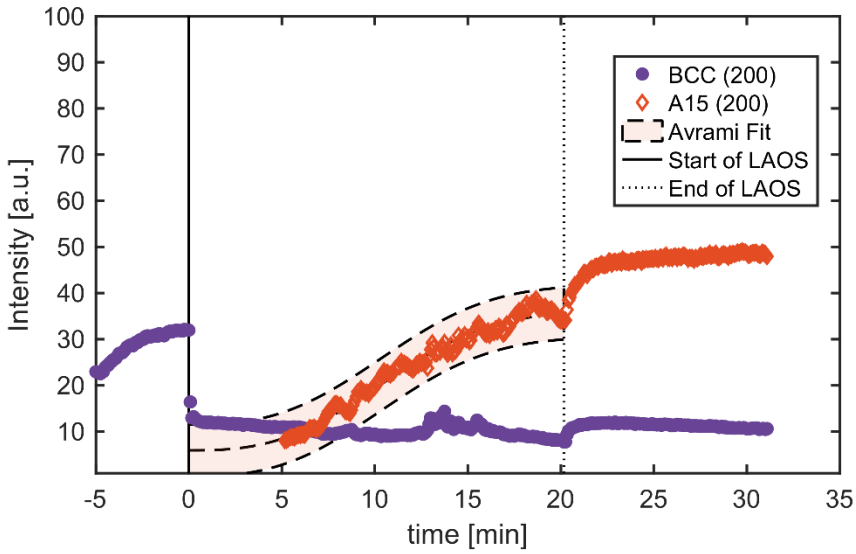

Figure 4.13: I_{200}(BCC) (*purple circles*) and I_{200}(A15) (*red diamonds*) as a function of time, where the solid black vertical line indicates the start of oscillatory shear with f = 1 Hz, γ = 177%. A fit to the MJA equation is shown as dashed black lines for the data acquired during shear, with the 95% confidence region shaded. Dashed vertical line indicates the cessation of shear.

Included in Figures 4.14 – 4.17 are complete 1-D TR-SAXS profiles and corresponding fits to the MJA model with the oscillatory shear frequency set to 9.9 Hz.

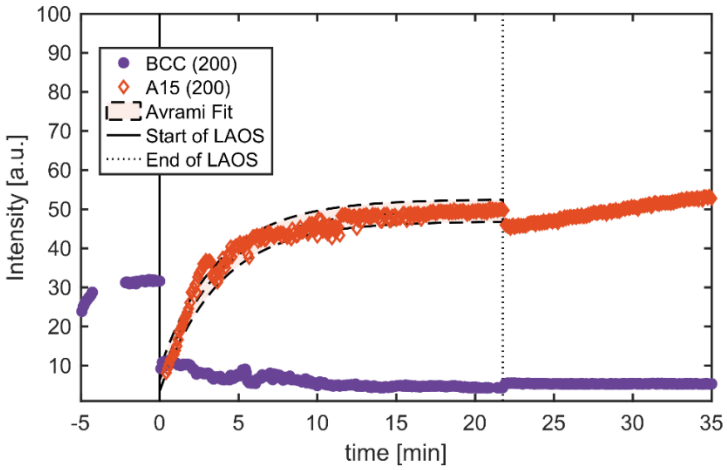

Figure 4.14: I_{200}(BCC) (*purple circles*) and I_{200}(A15) (*red diamonds*) as a function of time, where the solid black vertical line indicates the start of oscillatory shear with f = 9.9 Hz, γ = 177%. A fit to the MJA model is shown as dashed black lines for the data acquired during shear, with the 95% confidence region shaded. Dashed vertical line indicates the cessation of shear.

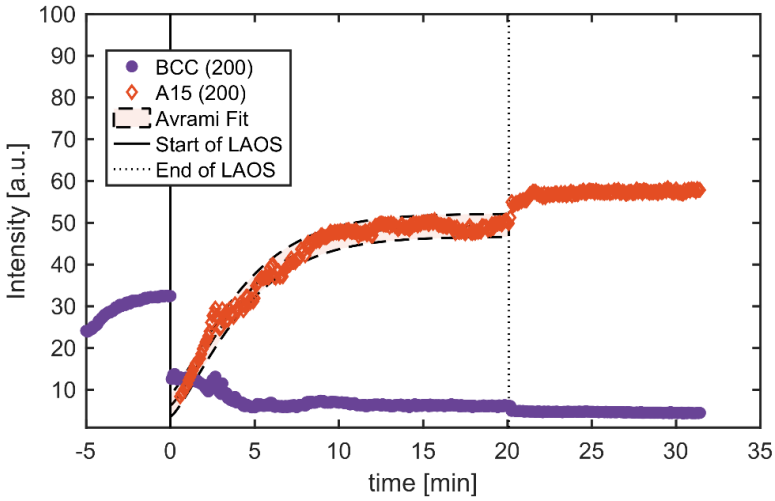

Figure 4.15: I_{200}(BCC) (*purple circles*) and I_{200}(A15) (*red diamonds*) as a function of time, where the solid black vertical line indicates the start of oscillatory shear with f = 9.9 Hz, γ = 88.5%. A fit to the MJA model is shown as dashed black lines for the data acquired during shear, with the 95% confidence region shaded. Dashed vertical line indicates the cessation of shear.

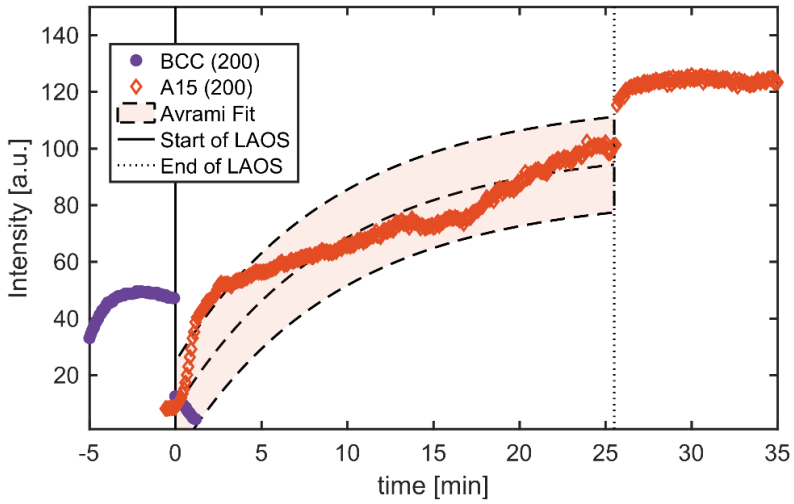

Figure 4.16: I_{200}(BCC) (*purple circles*) and I_{200}(A15) (*red diamonds*) as a function of time, where the solid black vertical line indicates the start of oscillatory shear with f = 9.9 Hz, γ = 35.4%. A fit to the MJA equation is shown as dashed black lines for the data acquired during shear, with the 95% confidence region shaded. Dashed vertical line indicates the cessation of shear.

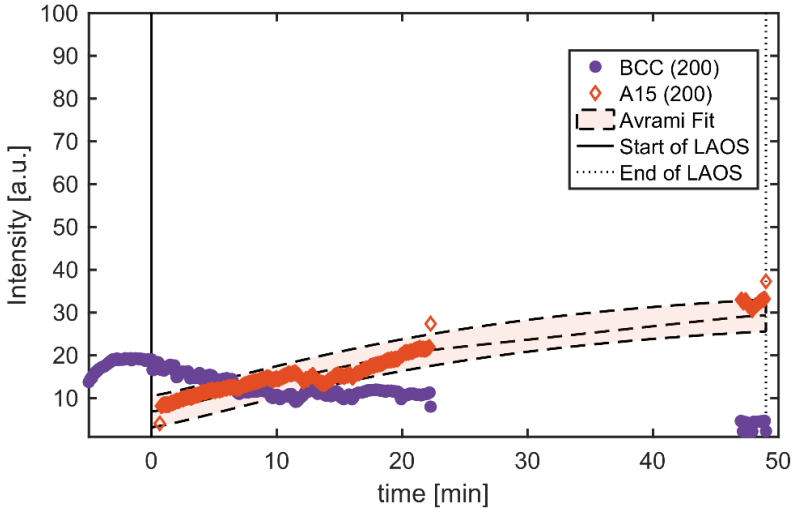

Figure 4.17: I_{200}(BCC) (*purple circles*) and I_{200}(A15) (*red diamonds*) as a function of time, where the solid black vertical line indicates the start of oscillatory shear with f = 9.9 Hz, γ = 3.54%. A fit to the MJA model is shown as dashed black lines for the data acquired during shear, with the 95% confidence region shaded. Dashed vertical line indicates the cessation of shear. The Avrami fit parameters show no significant deviation when fit to only the first 20 min of shear.

Chapter 5 Diffusion of proteins through the aqueous regions in block polymer liquid crystals – confinement and crowding in self-assembled nanostructures

Valentine C.S., Wholey C., Walker L.M., "Diffusion of proteins through the aqueous regions in block polymer liquid crystals – confinement and crowding in self-assembled nanostructures". *In submission, Soft Matter.*

The self-assembled crystalline phases observed in aqueous triblock polymer systems have been investigated for a wide variety of drug delivery methods ranging from delivery of small molecules in the hydrophobic cores to delivery of particles or proteins that reside in the semi-continuous aqueous interstitial environment. The goal of this work is to identify the design parameters that lead to decreased mobility of proteins in the aqueous continuous phase in PEO_m-PPO_n-PEO_m block polymer liquid crystals. We hypothesize that the dimensions of the interstitial site will become a controlling parameter as the length scale of the interstitial site approaches the hydrodynamic radius of the protein. In addition to this crowding effect within the interstitial site composed of concentrated PEO chains, the crystalline lattice is expected to sterically hinder the proteins moving throughout the continuous aqueous environment. Rheological characterization is used to identify triblock polymer concentrations that demonstrate favorable mechanical properties for applications. Synchrotron SAXS is used to accurately quantify the impact of concentration and temperature on the nano-scale arrangement of micelles. Semi-autonomous Fluorescence Recovery after Photobleaching (FRAP) is then used to

elucidate the impact of protein size on protein mobility through the liquid-crystalline matrices. This high-resolution structural dataset is leveraged to inform a model for diffusion of proteins via an interstitial hopping mechanism. Combining the FRAP and SAXS datasets, the protein radius relative to the radius of the aqueous interstitial site is identified as a controlling factor of protein diffusion.

5.1 Designing an aqueous block polymer crystal to confine proteins within

Pluronic® triblock polymers with the formula PEO_m-PPO_n-PEO_m, (also known as Synperonic® or Polaxomer) have been extensively studied over the past 30 years due to their commercial availability and widespread use in cosmetics, pharmaceutical formulations, protein stabilization, cell culture formulations, and nanoscale templating materials.[4–7] The self-assembled liquid crystalline phases observed in these aqueous block polymer systems have been investigated for a wide variety of drug delivery methods including liquid formulations that solidify upon injection for intramuscular delivery[133,134] and gels that adhere to mucosal walls.[135] Particles or proteins can be incorporated into the formulation of these self-assembled structures as cargo. The resulting meta-materials demonstrate macroscopic properties that arise from the nano-scale structure.[6,38,55,136,137] The release of small molecules or protein therapeutics from the structures will depend on the dissolution rate of the liquid crystalline structure and the diffusivity of the cargo within the nanoscale crystalline matrix.[138,139] The enzymatic activity of particles distributed throughout liquid crystalline matrices has been shown to depend on the geometric arrangement of the micellar structures in addition to the relative size of the aqueous channels that the enzymes are diffusing throughout.[140] To engineer and control the kinetics of cargo delivery, the mechanism of diffusion controlling the movement of large particles, or proteins, through the self-assembled liquid crystalline phases observed in aqueous triblock polymer systems must be quantified.

Another potential use case for self-assembled liquid crystalline meta-materials is for protein protection. The natural environment where proteins exist is a crowded chaotic storm of nutrients, waste, water, other proteins, DNA, and cell organelles. Proteins do not immediately denature at high temperatures in this crowded environment, where concentrations of large polymer-like molecules can exceed 30-40 volume percent.[141] Attempts have been made to increase protein protection by recreating this environment, via confinement[141–144] and crowding by large molecules such as polymers.[145,146] The aqueous, polymer-dense interstitial spaces in self-assembled liquid crystalline meta-materials may be tuned to mimic the intracellular environment, which could enhance protein protection from thermal denaturation and aggregation.[147]

Proteins and other particles can be readily placed into the aqueous interstitial sites of polyethylene (PEO) and polypropylene (PPO) block polymer liquid crystals.[55,147,148] Proteins are first dispersed in a Pluronic (PEO_m-PPO_n-PEO_m) and water solution that is liquid at low temperature ($T < 15°C$). Upon heating, the polymer molecules aggregate into micelles which then rapidly crystalize into larger structures, trapping the proteins into the aqueous pockets between each micelle. Figure 5.1 schematically shows this transition. Each micelle is an aggregate of a few dozen of polymer chains, with water swollen PEO brushes surrounding the hydrophobic core consisting of predominantly dehydrated PPO.[149,150] The properties and size of the pockets between micelles can be engineered by changing polymer

architecture and polymer concentration. Proteins are recovered via dilution or cooling. Previous studies using primarily contrast-matching neutron scattering and rheology have confirmed that nanoparticles and proteins are effectively templated into the aqueous interstitial sites.[6,48,136,148,151] It has also been shown that polymeric impurities are sequestered into the interstitial sites in these systems, supporting the hypothesis that sufficiently small particles will be preferentially segregated into the aqueous spaces rather than the micellar cores.[152] A self-assembled crystalline matrix like the system outlined above has the potential to protect proteins from aggregation and thermal denaturation via confinement and crowding effects. If the aqueous pockets are completely sealed, proteins will be effectively isolated from each other leading to decreased aggregation. Similarly, any decrease in protein mobility throughout the matrix will result in fewer chances for proteins to collide and aggregate – thereby providing an effective level of protection from aggregation and denaturation.

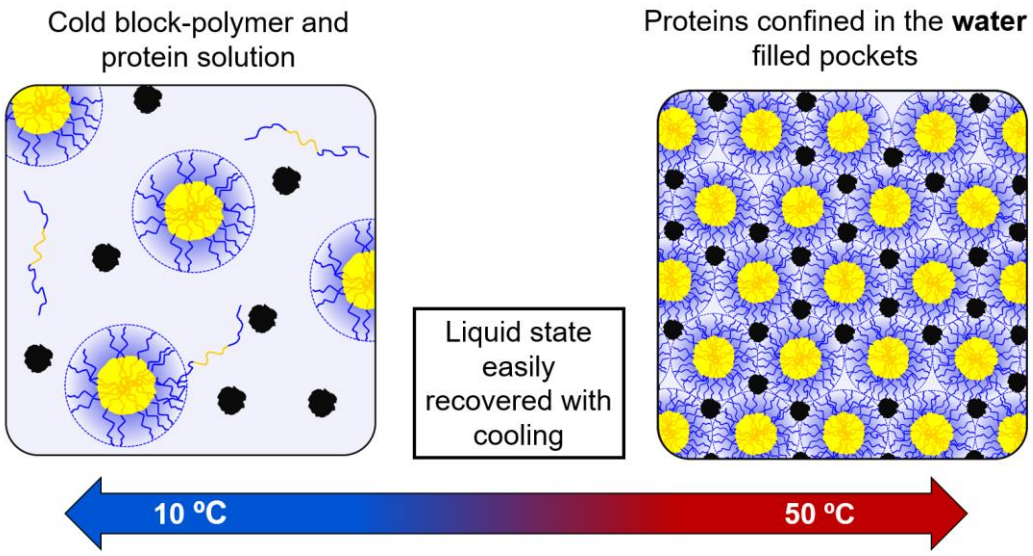

Figure 5.1: *Proteins captured in a spontaneously self-assembled structure.* Below the order-disorder transition temperature (~ 10°C), an aqueous dispersion of Pluronic® (PEO-PPO-PEO) and proteins (●) is formed. Upon heating the PPO blocks pack into hydrophobic cores (●) surrounded by aqueous PEO brushes. The micelles spontaneously arrange into crystalline phases. The proteins are guided to the aqueous pockets between micelles.

Pluronic (PEO_m-PPO_n-PEO_m) triblock polymers are commercially available in a variety of *m/n* ratios and total molecular weights. It should be noted that the commercially available samples can have broad block length distributions that vary between batches and manufacturers. These aqueous systems have characteristic thermo-reversible phase transitions, with a disordered phase often seen at temperatures below the structured gel-like phases.[4,56] Phases seen include disordered micelles, hexagonally-packed cylindrical phases, body-centered cubic (BCC), face-centered cubic (FCC), bicontinuous cubic phases, and the lamellar phase. The ratio of PEO or PPO controls the number of phases formed, with a larger ratio generally resulting in more phases observed.[34,56] The triblock molecular weight, block

ratio (*m/n),* and solvent choice will affect the interstitial site geometry as concentration and temperature are changed. As the molar mass of the PPO block increases, the minimum concentration for an ordered phase to form decreases from 60 wt% (MW_{PPO} ~1700g/mol) to 20 wt% (MW_{PPO} ~4000 g/mol). The relative size of the PEO and PPO blocks play a crucial role in the phase behavior. When the PEO blocks have a larger apparent volume than the PPO blocks, there is a tendency to form spherical or cylindrical structures.[56] Lamellar structures are favored when the PPO blocks are comparable in size to the PEO blocks. The effect of temperature on phase behavior is due to the temperature dependence of the solvent selectivity for one or both blocks. As temperature is increased, the PPO and PEO blocks become less soluble in water.[34] Simultaneously, the PEO-PPO interaction parameter will decrease with temperature which lowers the repulsion between the blocks. The summation of these effects is a decreased swelling of the PEO blocks at higher temperatures, and thus lower curvature structures are favored.[34]

In addition to the crystalline arrangement and size of micelles, the radial distribution of the PEO blocks within the micellar corona brushes will be affected by the polymer architecture. Course grained implicit solvent Langevin dynamics (CGIS LD) simulations comparing Pluronic L64 (PEO_{13}-PPO_{30}-PEO_{13}) to Pluronic F127 (PEO_{99}-PPO_{65}-PEO_{99}) show volumetric composition as a function of radius for two simulated micelles in water.[153] In F127, the higher ratio of PEO:PPO (*m/n* = 3) results in a PEO distribution

that extends almost 12 nm into solution from the core center, despite the maximum in PEO brush density lying near 5 nm. The effect of lowering the ratio of PEO:PPO (m/n = 0.85) produces a brush with a much tighter PEO corona in L64 that do not taper off into solution, showing an even distribution on either side of the radial location of maximum PEO brush density. While these simulations were done in dilute solution, similar trends in corona density could be occurring in the F127 micelles arranged into crystalline phases at higher concentration. As the micellar coronas define the boundaries of the interstitial sites, changes in brush density due to temperature and concentration will impact the environment surrounding the dispersed proteins.

Pluronic systems that demonstrate body-centered cubic (BCC) and face-centered cubic (FCC) structures are the focus of this work. It should be noted that the octahedral interstitial sites are part of a continuous aqueous environment as shown in Figure 5.2. Each site is surrounded by 6 micelles forming an octahedron. The stacking of the spherical micelles leaves an opening on each triangular face of the interstitial site. When the radius of the protein is larger than this opening, the protein will have to compress the PEO brushes surrounding the opening to successfully escape the interstitial site. In this case, the PEO brush density profile will impact the energy required for the protein to proceed through the opening. However, proteins with a sufficiently small radius will be able to pass through the opening unimpeded by the PEO brushes. In this second case, the main

factor slowing down the protein diffusivity in comparison to free solution will be geometric constraints caused by the presence of the micellar lattice.

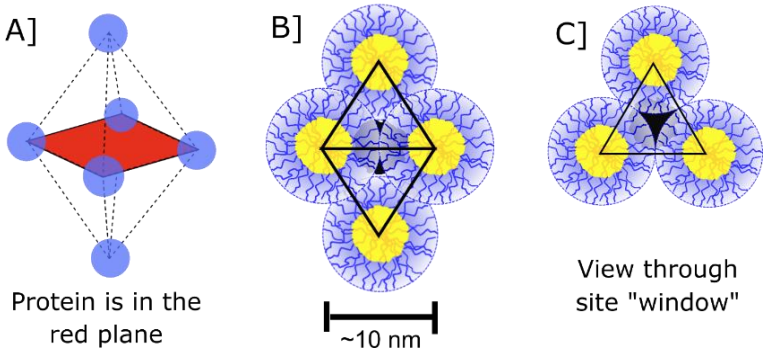

Figure 5.2: An illustration of the octahedral interstitial site. **[A]** A ball and stick diagram showing the location of each micelle at the points of the octahedron. The largest void is in the red plane, but the protein is free to move throughout this space. **[B]** From the side, the protein appears to be sealed into the site by PEO brushes. **[C]** However, there are 8 holes of least-resistance out of the interstitial site. These exist on each triangular face of the octahedron where the micelles meet. The window scales with micelle radius as $R_{window} = R_{micelle}\left[\left({}^{2}/_{3}\right)\sqrt{3} - 1\right]$.

The formulation parameters in self-assembling triblock polymer systems are intricately linked as described above. For example, changing the block length or molecular weight of the triblock polymer will shift or change the phase boundaries and crystalline phases formed.[56] Similarly, the solvent buffer salts and pH choice will produce shifts in the phase boundaries as the solubility of the PEO blocks changes.[51–54] The list of design parameters that will impact the liquid crystalline matrix includes the triblock molecular weight, PEO-PPO ratio (*m/n*), solvent buffer, buffer pH, triblock polymer concentration, and temperature range. To effectively explore this design space, the following constraints are introduced:

1. The material must experience a reversible order-disorder transition below room temperature but above the freezing point of the buffer solvent ($-5 < T_{ODT} < 15$ °C). This will facilitate the mechanism of protein dispersion outlined in Figure 5.1.
2. The ideal material will be a gel-like solid within the temperature range of interest (25-55°C) to facilitate protein storage.
3. There should not be phase transitions within the temperature range of interest, as this could disrupt protein confinement.
4. The buffer chosen should be able to maintain a pH far from the isoelectric point of the protein. Avoiding the isoelectric point will increase protein stability and resistance to aggregation.

With these constraints in place, the design space is large but manageable. The list of potential Pluronic triblock polymers was assembled using existing phase diagrams and scattering data from the literature.[6,55–57] Pluronic polymers of interest were chosen that demonstrated large cubic crystalline regions with an order-to-disorder transition (ODT) in the range of 0 to 15 °C so that constraints 1) and 2) would be met. After selecting P123, F87, and F127 as potential candidate triblock polymers, the concentration ranges of interest were narrowed using rheological characterization to quantify the ODT with changing polymer concentration. Finally, we chose to narrow the solvent buffer choice to bicarbonate buffer at pH = 9, which was substantially far away from the isoelectric point of the four globular proteins chosen for study.

Characterization of protein mobility after incorporation into the nanostructured matrix was chosen as a direct measure of protein interaction with the matrix. A semi-automated Fluorescence Recovery After Photobleaching (FRAP) system was developed to explore this large parameter space efficiently. Samples showing marked decreases in diffusivity were designated for thorough geometric classification via Small Angle X-ray Scattering (SAXS). The goal of this work to explore this large parameter space to develop design rules that help formulation scientists control mobility of proteins or cargo particles in self-assembled liquid crystalline phases.

5.2 Experimental Methods - Semi-Autonomous FRAP, SAXS, and Rheology

Pluronic P123 [PEO_{20}-PPO_{70}-PEO_{20}] (Sigma Aldrich, lot# MKCH4375), F127 [PEO_{106}-PPO_{70}-PEO_{106}] (Sigma Aldrich, lot# BCBX9224), and F87 [PEO_{75}-PPO_{46}-PEO_{75}] (BASF, lot# 0008779132) were used as received. Bicarbonate buffer (pH = 9) was freshly made with purified 18.2 MΩ·cm water before sample preparation. Bovine serum albumin, BSA (Sigma Aldrich, lot# SLCC2453), lysozyme from chicken egg white, LYS (Alfa Aesar, lot# P25B001), albumin from chicken egg white also known as ovalbumin, CHA (Sigma Aldrich, lot# SLCD9242), and human serum albumin, HSA (Sigma Aldrich, lot# SLCD9951), were purchased and used as received.

Proteins were fluorescently labeled according to the following procedure, which was adapted from Feltkamp *et al*.[154,155] 1 mg/mL FITC isothiocyanate solution was made using 0.15M Na_2HPO_4 as the solvent. The proteins are dissolved into Phosphate Buffered Saline (PBS) to a concentration of $5x10^{-4}$ mmol/mL. For BSA this is ~ 30 mg/mL. 1.5 mL of the FITC solution was then added to 0.25 mL of the protein solution. The solution was then allowed to react in the dark at room temperature while mixing end-over-end for one hour. Post-reaction, the excess FITC isothiocyanate was removed from the reaction via elution with bicarbonate buffer using PD-10 desalting columns packed with Sephadex G-25 resin. Concentration of the eluted bicarbonate protein solution was confirmed by

measurement of the absorbance at 495 and 280 nm, A_{495} and A_{280}. (NanoDrop, Thermo Fisher Scientific; Waltham, MA). The concentration of the tagged protein is calculated using,

$$C = \frac{MW}{\in} \left(\mathrm{A}_{280} - \left(\mathrm{A}_{495} \times \mathrm{CF}\right)\right)$$

where MW is the molecular weight of the protein, ∈ is the molar extinction coefficient, and *CF* is the correction factor. The correction factor accounts for adsorption at 280 nm due to the dye and not the protein. For FITC the correction factor is approximately equal to 0.3.[156]

Aliquots of the stock solution of fluorescently labeled proteins were then added to pre-weighed amounts of triblock polymer in 2 mL vials. Extra bicarbonate buffer was added so that the protein concentration was 5×10^{-5} mmol/mL in each sample. This concentration was chosen to keep samples sufficiently dilute, there will always be less than one protein per unit cell of the crystal. Samples were used within one week of preparation. The 2mL vials of protein and triblock solution were mixed end over end at 8°C for at least 24 hours to ensure sufficient dispersion and dissolution of the polymer.

Protein Characterization – Dynamic Light Scattering (DLS)

Dynamic light scattering (DLS) was used to determine the free solution diffusion coefficient of each protein (Table 5.1, Figure 5.3). Proteins were used as received and dispersed into bicarbonate buffer before performing characterization via DLS at 25,35,45, and 55°C. DLS measurements were performed using a Malvern Nanosizer (Malvern Panalytical Ltd, UK).

Table 5.1: Protein diffusivity and hydrodynamic radius in bicarbonate buffer as measured by DLS. The diffusivity, D_0, is used to calculate the hydrodynamic radius, R_h, via the Stokes Einstein Equation. Standard Deviations are provided based on 15 runs per trial, with three trials averaged at each temperature for each protein.

Protein	T [°C]	D_0 [μm/s^2]	Std. D_0 [μm/s^2]	R_h [nm]	Std. R_h [nm]
LYS	25	112.0	4.7	2.2	0.7
	35	150.7	3.4	2.1	0.4
	45	188.3	2.6	2.1	0.3
	55	226.7	30.0	2.1	1.0
HSA	25	71.7	3.8	3.4	0.8
	35	93.2	3.3	3.4	0.6
	45	115.0	4.4	3.4	0.8
	55	140.7	5.6	3.4	0.9
CHA	25	57.0	8.0	4.3	2.2
	35	70.4	8.8	4.3	2.2
	45	87.5	10.2	4.6	2.3
	55	108.0	10.8	4.5	2.2
BSA	25	52.4	5.7	4.7	1.7
	35	68.1	6.1	4.6	1.6
	45	85.3	6.6	4.6	1.5
	55	95.4	6.8	4.9	1.5

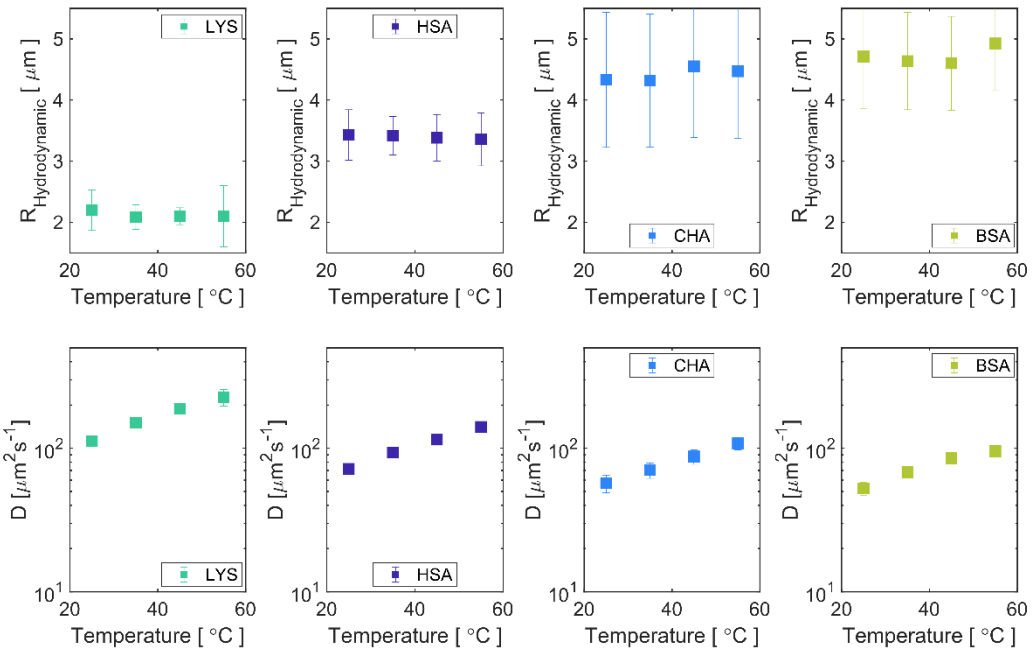

Figure 5.3: Hydrodynamic radii and diffusivity of all proteins used in bicarbonate buffer (pH = 9). Measured by DLS as described in methods. LYS = Lysozyme. HSA = Human Serum Albumin. CHA = albumin from chicken egg white. BSA = bovine serum albumin. *N* = 3.

Rheological Characterization

Rheological characterization of the Pluronic samples was accomplished with a TA Instruments (TA Instruments; New Castle, DE) DHR-2 stress-controlled rheometer with a 40 mm parallel plate geometry and an 800 µm gap height. Upon loading, samples were first cooled below the ODT to 0°C to relieve loading stresses. To prevent water evaporation at higher temperatures, a 4 cm tall Teflon ring was sealed around the geometry and filled with ~ 20 mL of FC-70 Fluorinert® fluorinated oil. This low viscosity oil pool is ~ 2 cm deep and provides sufficient evaporation control with minimal increase in measured torque. A ramp rate of 1°C/min

was used for all trials. The strain amplitude (γ = 0.25%) for all temperature ramps (*f* = 1 Hz) is verified to be in the linear viscoelastic regime through amplitude sweeps at 25, 35, 45, and 55°C.

Small-angle X-ray Scattering (SAXS)

Based on previously reported unit cell size estimations for F127 and F87, the aqueous interstitial sites were estimated to be between 30-200% larger than the protein radius.[6,55,57] While scattering data available in the literature provide an excellent starting point, most scattering data was recorded with high-purity water as the solvent. The presence of buffer salts in the solvent will shift the phase transitions as detected by rheological studies.[51] Previous work has also shown significant phase boundary shifts and even complete loss of solid-phase formation in F127 due to the addition of certain salts to the solvent.[52–54] SAXS measurements were performed at the 12-ID-B beamline at the Argonne National Lab Advanced Photon Source (APS, Argonne, IL, U.S.A). Samples were hermetically sealed into alodined aluminum DSC pans (TA instruments, Newcastle, DE). Samples were equilibrated for at least 5 minutes at the desired temperature prior to data collection. Typical exposure times were about 1 second. An incident beam energy of 13.3 keV (λ = 0.932 Å) was used. 2D-SAXS patterns were acquired on a Pilatus 2M detector with 172 µm x 172 µm resolution. The wavevector, $q = (\,^{4\pi}/_{\lambda})\,\sin(^{\theta}/_{2})$ was calibrated with a silver behenate standard. The complete SAXS dataset is included in Tables 5.2 - 5.4 and summarized in Figure 5.4.

Table 5.2: SAXS data for Pluronic F87 were collected for 30, 35, and 42.5 wt% samples. For concentrations without SAXS data, the phase is assumed to be BCC and the micellar radius is determined via a 2nd-order polynomial fit and extrapolation from 30, 35, and 42.5 wt%. Included is the location of the first peak (*q1*), the unit cell size (*a*), the hard sphere radius of the micelles (R_m), the radius of the octahedral site (R_{oct}), and the radius of the hole between micelles at the triangular face of each octahedral site (R_{hole}).

Pluronic	Wt %	T [°C]	q1 [Å^{-1}]	phase	a [nm]	R_m [nm]	R_{oct}	R_{hole}	Extrapolated?
F87	30	25	0.0593	BCC	14.99	6.49	4.11	1.46	SAXS data
		35	0.0585	BCC	15.20	6.58	4.17	1.48	
		45	0.0578	BCC	15.38	6.66	4.22	1.50	
		55	0.0572	BCC	15.53	6.72	4.26	1.51	
	35	25	0.0597	BCC	14.89	6.45	4.08	1.45	SAXS data
		35	0.0593	BCC	14.97	6.48	4.10	1.46	
		45	0.0577	BCC	15.41	6.67	4.22	1.50	
		55	0.0563	BCC	15.79	6.84	4.33	1.54	
	37.5	25	Extrapolated	BCC	14.86	6.44	4.07	1.45	Extrapolated
		35		BCC	14.94	6.47	4.09	1.45	
		45		BCC	15.40	6.67	4.22	1.50	
		55		BCC	15.81	6.85	4.33	1.54	
	40	25	Extrapolated	BCC	14.86	6.44	4.07	1.45	Extrapolated
		35		BCC	14.95	6.47	4.10	1.46	
		45		BCC	15.39	6.66	4.22	1.50	
		55		BCC	15.76	6.82	4.32	1.53	
	42.5	25	0.0597	BCC	14.88	6.44	4.08	1.45	SAXS data
		35	0.0592	BCC	15.02	6.50	4.12	1.46	
		45	0.0578	BCC	15.37	6.65	4.21	1.50	
		55	0.0568	BCC	15.63	6.77	4.28	1.52	

Table 5.3: SAXS data for Pluronic F127 were collected for 22.5 and 30 wt% samples. For concentrations without SAXS data, the phase is assumed to be BCC and the micellar radius is determined via a linear extrapolation of the micellar radius measured at 22.5 and 30 wt%. Included is the location of the first peak (*q1*), the unit cell size (*a*), the hard sphere radius of the micelles (R_m), the radius of the octahedral site (R_{oct}), and the radius of the hole between micelles at the triangular face of each octahedral site (R_{hole}). * For 22.5 wt% samples, q1 is taken to be the 220 peak, which is the 3rd peak seen in FCC. The first two peaks, (111) and (200), were visible but the 220 peak provided a more distinct anchor for unit cell size calculations.

Pluronic	Wt %	T [°C]	q1 [Å^{-1}]	phase	a [nm]	R_m [nm]	R_{oct}	R_{hole}	Extrapolated?
F127	22.5	25	*0.0642	FCC	27.69	9.79	4.06	2.20	SAXS data
		35	*0.0641	FCC	27.74	9.81	4.06	2.20	
		45	*0.0640	FCC	27.79	9.82	4.07	2.21	
		55	*0.0638	FCC	27.87	9.85	4.08	2.21	
	25	25	Extrapolated	BCC	22.11	9.57	6.06	2.15	Extrapolated
		35		BCC	22.15	9.59	6.07	2.16	
		45		BCC	22.19	9.61	6.08	2.16	
		55		BCC	22.25	9.63	6.10	2.17	
	28	25	Extrapolated	BCC	21.48	9.30	5.89	2.09	Extrapolated
		35		BCC	21.53	9.32	5.90	2.10	
		45		BCC	21.57	9.34	5.91	2.10	
		55		BCC	21.61	9.36	5.92	2.10	
	30	25	0.0426	BCC	20.85	9.03	5.72	2.03	SAXS data
		35	0.0425	BCC	20.91	9.05	5.73	2.03	
		45	0.0424	BCC	20.96	9.07	5.74	2.04	
		55	0.0424	BCC	20.98	9.09	5.75	2.04	

Table 5.4: SAXS data for Pluronic P123 were collected for 35 wt% samples. Included is the location of the first peak (*q1*), the unit cell size (*a*), and the cylindrical radius of the micelles (R_m).

Pluronic	Wt %	T [°C]	q1 [Å^{-1}]	phase	a [nm]	R_m [nm]
P123	35	25	0.0410	HEX	15.32	7.66
		35	0.0407	HEX	15.42	7.71
		45	0.0382	HEX	16.46	8.23
		55	0.0000	DIS.	0.00	0.00

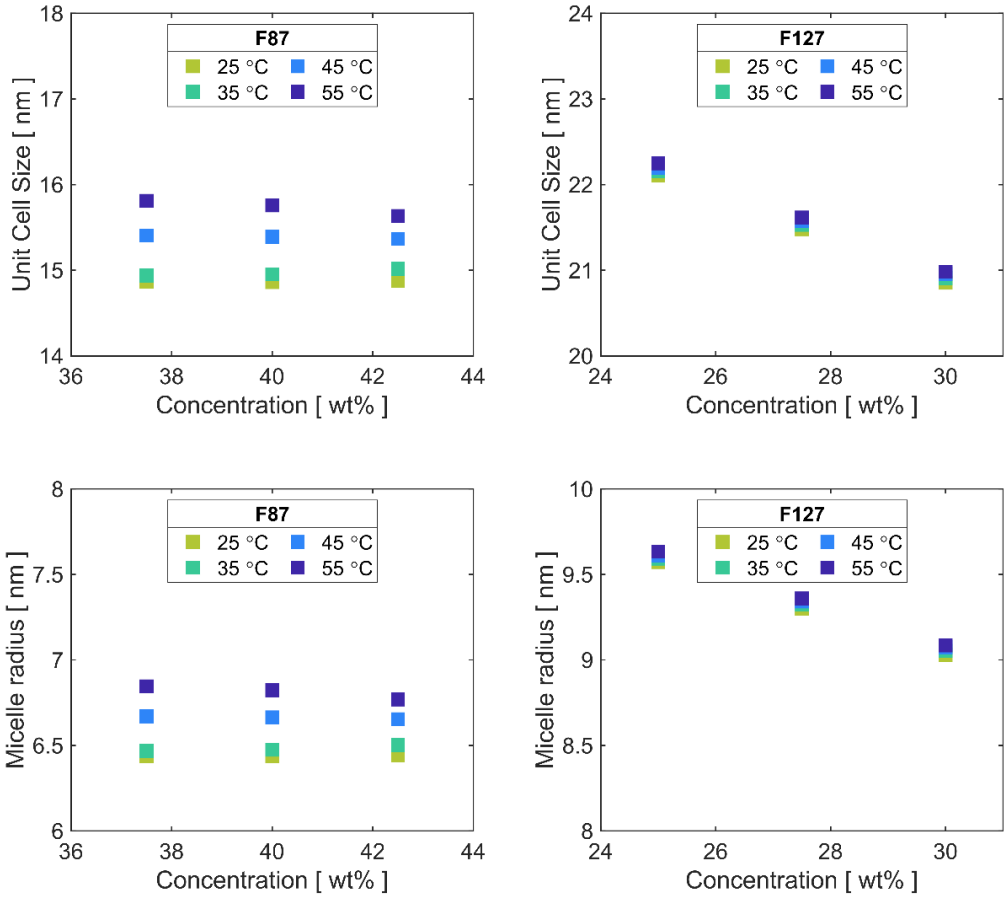

Figure 5.4: Unit cell size and corresponding micelle radius as calculated using SAXS data for F87 (Table 5.2) and F127 (Table 5.3).

Semi-Automated Fluorescence Recovery After Photobleaching (FRAP)

The triblock polymer and fluorescently labeled protein mixtures are first loaded into rectangular glass capillaries via capillary action (0.20 x 4.00 mm inner diameter cross section, VitroCom, Mountain Lakes, NJ). Sections of capillary (2 cm long) were gently placed into 2 mL sample vials and left to equilibrate for 15 minutes in the refrigerator (8°C). This is sufficient time for the viscous material to fill the length of the capillary. The vials are then

brought to room temperature, which solidifies the material. Each filled capillary is carefully cleaned to remove material on the outside of the capillary and laid onto microscope slides, evenly spaced with up to 6 capillaries per slide. Approximately 5 mL of 5-minute epoxy (Gorilla Glue Inc.), is mixed and de-gassed using an AR-100 planetary conditioning mixer (Thinky; Laguna Hills, CA). The bubble-free epoxy is then slowly poured over the capillaries, creating an air-tight sealant layer that coats the entire capillary in an optically clear layer. The epoxy-coated capillary slides are then left at room temperature to cure for one hour. The capillaries are subsequently pre-heated to the temperature at which FRAP will be performed for 1 hour prior to data collection.

The capillaries are imaged using a Nikon Eclipse Ti-u Microscope at 20x (Melville, NY). The image collection process was automated using MicroManager Software.[157,158] MicroManager facilitates communication and control between the computer, laser control unit, LED excitation lamp, camera, auto-focus unit, and precision XY stage. Temperature control is provided via a glass microscopy stage insert (Tokai Hit; Shizuoka-ken, Japan). An insulated box is placed on top of the sample area to maintain stable temperature. A 488 nm laser (Sapphire™, Coherent Inc; Santa Clara, CA) at 100% strength is used to photo bleach each position of interest for 5 seconds. Every 2 minutes for the first two hours, the LED excitation lamp (X-Cite mini+, Excelitas Technologies Corp; Waltham, MA) at 25% intensity is used to take an image of the bleached spot with a 100ms exposure time

to minimize photobleaching effects while retaining image quality during the initial intensity recovery. After the first two hours, images are taken every 20 minutes to further minimize photobleaching effects while the long-time recovery is observed. Images were captured with a pco.panda 4.2 camera (Pco-tech; Wilmington, DE). FRAP is performed at 3 locations per capillary over a time of at least 18 hours, and up to 24 hours. This system is designed to perform FRAP data collection simultaneously at up to 54 locations.

The fluorescence intensity at each location was calculated in each frame using MATLAB, in a rigorous multistep normalization process (see supporting information). The intensity within the bleached region, $I_b(t)$, is first normalized by the initial intensity of the region before bleaching, $I_b(t=0)$. To account for photobleaching effects, the intensity of a concentric unbleached region, $I_{ub}(t)$, far from the bleached area is tracked in every image. The final normalized intensity is calculated as

$$I_N(t) = \frac{I_b(t)}{I_b(t=0)} \frac{I_{ub}(t=0)}{I_{ub}(t)} \quad (1)$$

To extract mobility information from the dataset of normalized intensity versus time, the normalized intensity recovery curves are fit to the following function

$$I_N(t) = f_m \left[\sum_{n=0}^{\infty} \frac{-K^n}{n!} \left[1 + n\left(1 + \frac{2t}{\tau}\right) \right]^{-1} \right] + (1 - f_m) \frac{I_N(1)}{I_{N,i}} \quad (2)$$

$I_N(1)$ is the intensity in the first recorded frame after photobleaching, $I_{N,i}$ is the pre-bleach intensity, K is a parameter describing the shape of the initial intensity recovery, and τ is the time constant for intensity recovery. f_m is the mobile fraction of proteins, calculated as the fraction of intensity recovered within the bleached region. The mobile fraction is constrained between 0 and 1 and reflects the fraction of proteins with detectable movement on the timescale of the experiment. A mobile fraction of 0 corresponds to complete immobilization of the proteins, while a mobile fraction of 1 implies that the proteins are free to diffuse throughout the liquid crystal. A mobile fraction less than 1 could mean that a significant number of proteins do not leave their initial interstitial site throughout the duration of the experiment. Finally, diffusivity coefficients are calculated as

$$D = \frac{r_0^2}{4\tau}. \quad (3)$$

Where r_0 is the initial radius of the bleached circle, taken to be the full width half max of the gaussian shaped intensity profile immediately after bleaching. Typical spot sizes were 21 ± 3μm This measurement and data analysis procedure is repeated at three different locations within the glass capillary for every sample.

5.3 Protein diffusivity measurements in block polymer crystals

The first goal of this work is to identify aqueous triblock systems with wide cubic regions on phase diagrams so that the impact of crystalline phase, temperature, and polymer concentration on protein diffusivity can be studied without complications arising from phase transitions. The material must also experience a reversible order-disorder transition below room temperature but above the freezing point of the solvent. Three triblock polymers (Pluronic F87, F127, and P123) were chosen for initial investigation due to their reported phase diagrams showing ODTs in the region of interest.[6,55–57] Rheological temperature ramps (γ = 0.25%, *f* = 1 Hz) with a ramp rate of 1°C/min were used to find triblock concentrations that meet these constraints.

Figure 5.5 shows the magnitude of the complex modulus, |*G**|, and the phase angle, δ, for several concentrations of F87, F127, and P123 during temperature ramps between 0 and 60°C. All samples shown experience a disordered liquid-like state at 0°C as shown by δ ~ 90°. As temperature is increased, the block polymer micelles crystallize resulting in a sharp reduction in δ and 4-5 orders of magnitude increase in |*G**|. For P123 (Figure 5.5A) as the samples are heated from 0°C, there is an increase in modulus over a 1-5°C window as the material crystalizes through a lower ODT. As the samples are heated further a solid-like phase is observed. A subsequent upper ODT is observed with further heating for all concentrations of P123 tested. At the lowest concentration tested, 25 wt%,

the upper ODT is only 15°C higher than the lower ODT. At an intermediate concentration of 30 wt% P123, a sharp lower and upper ODT with a consistent modulus from 14-38°C was observed. The presence of multiple phase transitions within the 25-55°C window will convolute diffusivity measurements as we try to understand how temperature influences protein mobility throughout these self-assembled lattices. Significant changes in modulus with temperature were observed in this solid region, which could signify phase transitions with temperature.[21–23] The rheological temperature sweeps for P123 show a solid region that is not large or consistent enough to justify diffusivity measurements via FRAP.

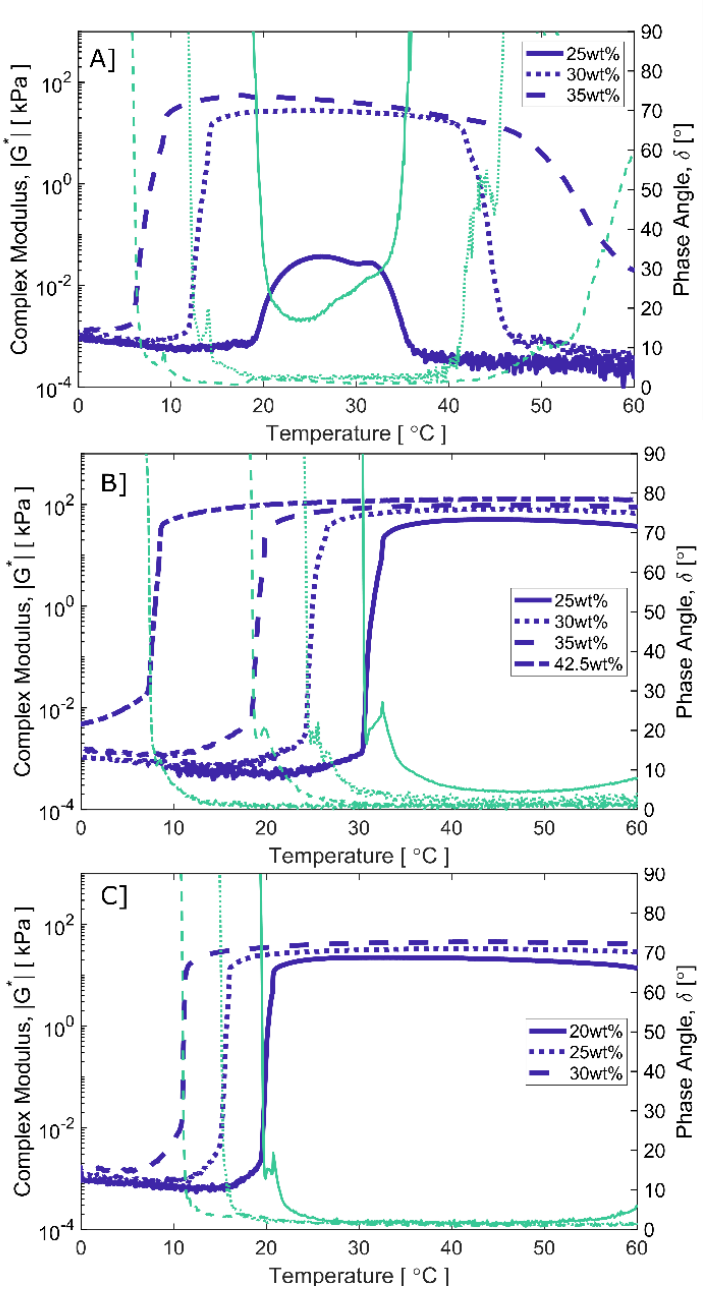

Figure 5.5: Complex modulus (|*G**|, blue lines) and phase angle (δ, cyan lines) as a function of temperature (γ = 0.25%, *f* = 1 Hz) for **[A]** P123 25, 30, and 35 wt% in bicarbonate buffer demonstrating the effect of concentration on the lower and upper ODTs. **[B]** F87 25, 30, 35, and 42.5 wt% in bicarbonate buffer demonstrating decreasing lower ODT with increasing concentration. **[C]** F127 20, 25, and 30 wt% in bicarbonate buffer demonstrating decreasing lower ODT with increasing concentration.

For F87 and F127 (Figures 5.5B and 5.5C), increasing Pluronic concentration results in a reduction in the ODT and increase of the modulus observed after crystallization. As the samples are heated from 0°C, there is a sharp increase in modulus over a 1-2°C window as the material solidifies through the ODT. As the samples are heated further into the solid-like phase, a plateau in modulus is observed on the order of 10-100 kPa. Increasing polymer concentration reduces the change in modulus with temperature above the ODT within this plateau. F87 and F127 show only a lower ODT with a sharp transition in all samples tested. This reversible phase transition can be tuned to occur between 15 and 0°C by adjusting concentration, facilitating protein dispersion via refrigeration. These samples form crystalline phases that show stable rheological properties within the temperature window of 25-55°C. From these studies, the F87 and F127 concentration windows of interest were narrowed for FRAP experiments. F87 samples in the range of 37.5-42.5wt% and F127 samples in the range of 25-30wt% were chosen.

Synchrotron small-angle X-ray scattering (SAXS) was used to collect structural information for samples demonstrating favorable rheological properties at 25, 35, 45, and 55°C. The size of the crystalline unit cell, *a*, and the arrangement of the micelles within the unit cell, or crystalline phase, were resolved as a function of temperature and concentration. Figure 5.6 shows representative 1D-SAXS profiles for F87 and F127. All SAXS data is included in Tables 5.2 - 5.4 and summarized in Figure 5.4. A change in

crystalline phase with increasing temperature is not observed in any of the F87 or F127 samples within the temperature window of 25-55°C. Nearly all samples demonstrated body-centered cubic (BCC) crystalline phases. Therefore, FRAP data can be collected within the entire temperature range for each sample without complications arising from phase transitions in the solid-like state. For F87 and F127, the unit cell size increases slightly with increasing temperature (Figure 5.4). In F87 the unit cell size is nearly constant with increasing concentration, however in F127 a decrease in unit cell size with increasing concentration is observed (Figure 5.4). This dataset does not show rich phase behavior, however fine-grained composition and temperature dependent structural data will be important for researchers to access as more liquid crystalline materials are used in formulation attempts. With the unit cell size now well-understood for F87 and F127 as a function of polymer concentration and temperature, diffusion models can be applied that account for the relative size of the protein to the interstitial site size.

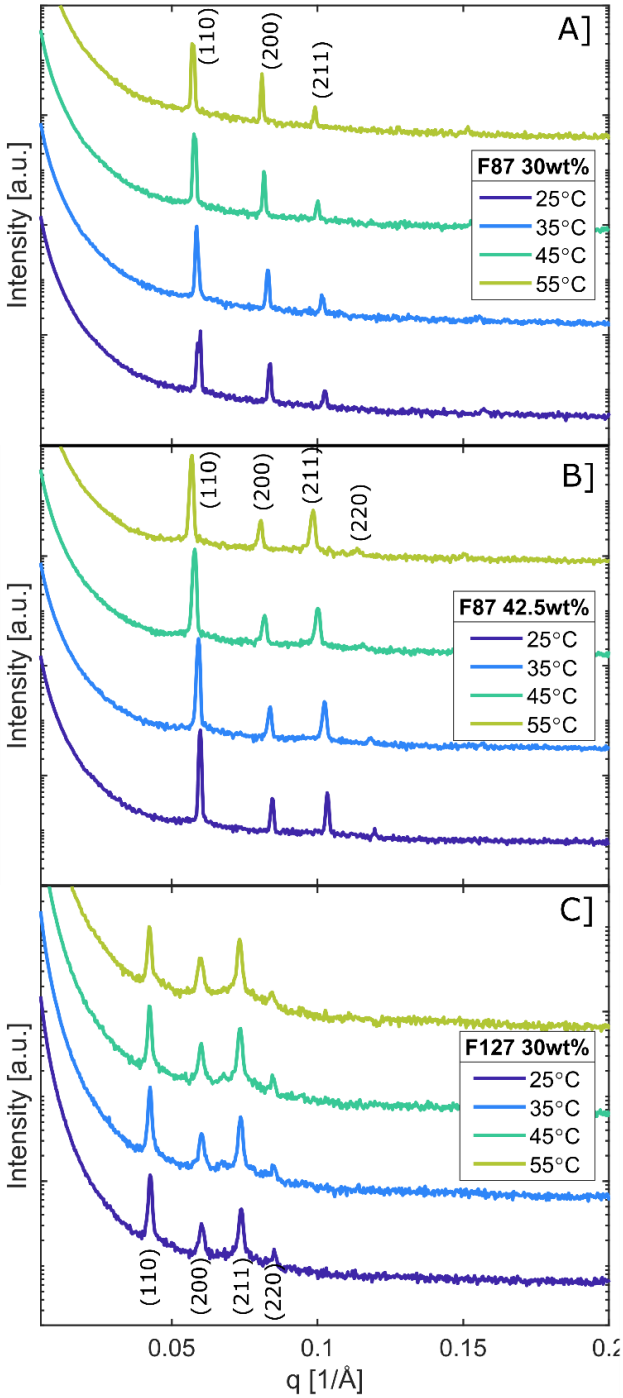

Figure 5.6: 1D-SAXS profiles for **[A]** F87 30wt% **[B]** F87 42.5wt% **[C]** F127 30wt%. Indexed peaks for BCC are overlaid. A slight downshift in the first peak indicates an increase in unit cell size with increasing temperature. Intensity is shifted vertically for clarity.

Using semi-automated FRAP, the mobility of BSA from 25 to 55°C in F127 and F87 at concentrations demonstrating favorable rheological properties was characterized and is shown in Figure 5.7. The protein mobility is reported as a diffusive component (D) and a mobile fraction of proteins (f_m) as defined in equations 2 and 3. In Figures 5.7A and 5.7B the diffusivity of the protein (D) normalized by its diffusivity in free solution (D_0) versus temperature for F87 and F127 is shown. D_0 is measured by DLS at the temperature which FRAP data was collected as described in the methods section (Table 1, Figure 5.3). As temperature is initially increased, a decrease in D/D_0 of BSA in F87 is observed. This is followed by an increase in D/D_0 from 35 to 45°C. However, further increasing the temperature from 45 to 55°C results in a drastic 50-100 times decrease in D/D_0 of BSA in F87. For F127, a steady increase in D/D_0 of BSA as temperature is increased from 25 to 45°C is seen. This is followed by a slight decrease in D/D_0 of BSA as temperature is increased from 45 to 55°C. The normalization procedure accounts for changes in diffusivity through the aqueous environment arising from temperature effects in the absence of polymer interactions or steric hindrance. Trends in D/D_0 with temperature arise from the effect of temperature on the crystalline unit cell and changing interactions between the PEO coronas and the protein. Incorporation of BSA into F87 and F127 liquid crystals results in at least a two order of magnitude decrease in diffusivity across the entire temperature range.

In Figures 5.7C and 5.7D changes in the mobile fraction of proteins with increasing temperature for F87 and F127 is shown. At 25°C almost all BSA molecules in F87 and F127 are free to move throughout the liquid crystalline lattices; the mobile fraction of proteins, f_m, is close to one. With increasing temperature, the mobile fraction begins to decrease in both F87 and F127, however the effect is significantly more pronounced in F87. In F87 at 40 wt% up to 78% of proteins are immobilized at 55°C. During this ~24-hour long experiment, the remainder of proteins that were still mobile diffused over 1000x slower than in free solution. A substantial decrease in protein mobility in F87 and F127 is reported.

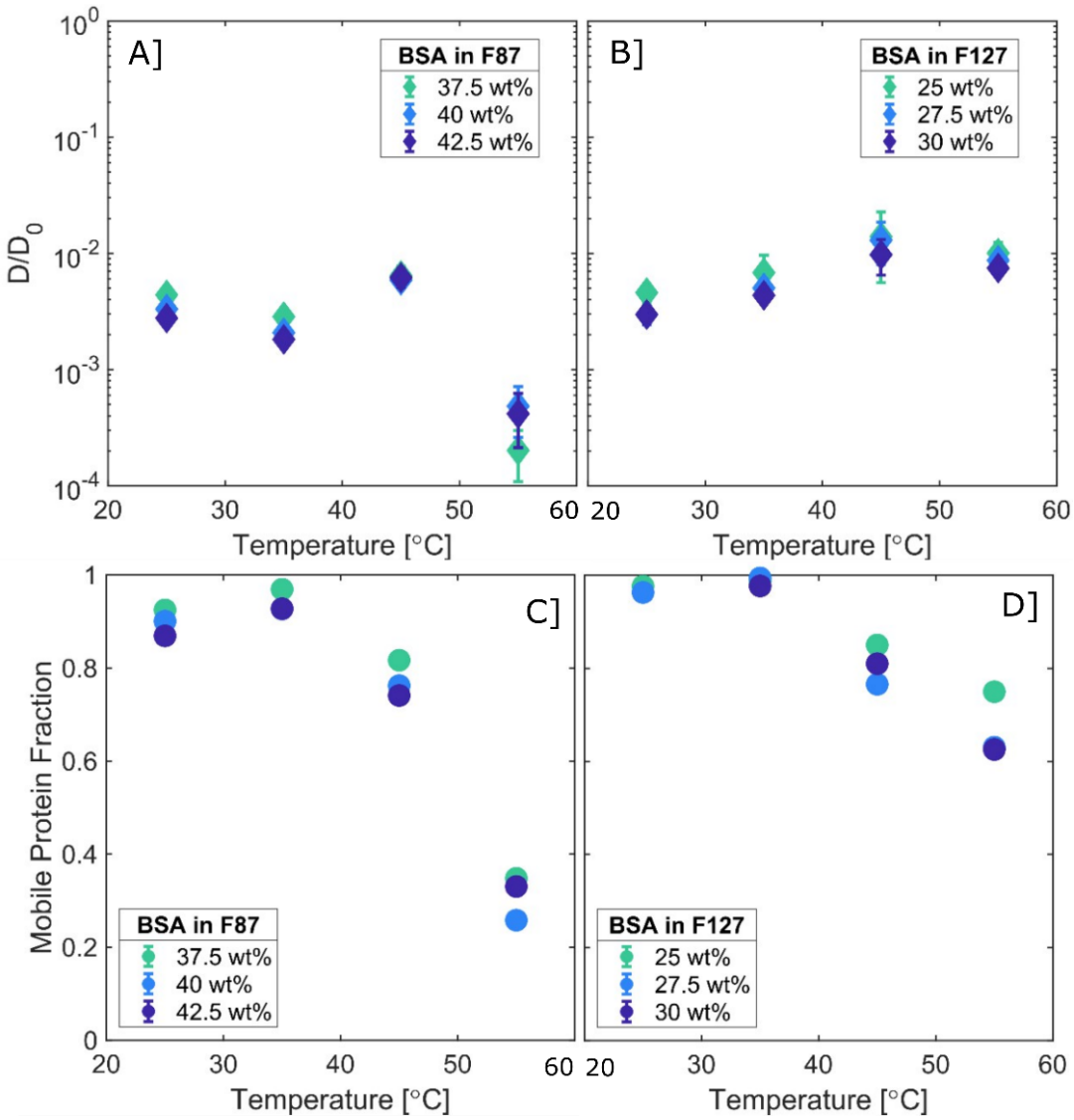

Figure 5.7: Normalized Diffusivity data for BSA in **[A]** Pluronic F87 and **[B]** F127. The data is normalized by the diffusivity of the proteins in polymer-free bicarbonate buffer at the temperature indicated. The mobile fraction of proteins as calculated during FRAP diffusivity fitting for BSA in **[C]** Pluronic F87 and **[D]** F127. Error bars are shown but are smaller than the marker size in most cases. *N* = 3.

To understand the importance of protein size on diffusivity through the cubic liquid crystals in F87 and F127, FRAP measurements were repeated with 4 proteins of varying size. These proteins span a range of ~2

– 5 nm in hydrodynamic radius, R_h (Table 1, Figure 5.3). From the SAXS data on the liquid crystalline phases (Figures 5.4 and 5.6), the radius of the octahedral interstitial site, R_{oct}, is calculated at each concentration and temperature for F87 and F127 where FRAP data was collected. (Tables 5.2-5.4). From this data, the size of the protein, R_h, *relative* to the size of the aqueous octahedral interstitial site, R_{oct}, is calculated. This comprehensive dataset is used to elucidate trends in D/D_0 and f_m with respect to $R_{h,protein}/R_{oct}$. This data is summarized in Figure 5.8.

In Figures 5.8A and 5.8B the diffusivity of the protein (D) normalized by its diffusivity in free solution (D_0) is shown versus increasing $R_{h,protein}/R_{oct}$ for F87 and F127. For both F87 and F127, as $R_{h,protein}/R_{oct}$ is increased above 0.2, the diffusivity of the protein decreases. As the radius of the protein begins to increase in size relative to the radius of the interstitial site, $R_{h,protein}/R_{oct}$ increases and a large decrease in diffusivity is observed. In F87 when $R_{h,protein}/R_{oct}$ is increased beyond one, a 2 order of magnitude decrease in D/D_0 from $1x10^{-2}$ to $2x10^{-4}$ is observed. In F127 D/D_0 slightly decreases with increasing $R_{h,protein}/R_{oct}$, however the dramatic decrease in diffusivity seen at high $R_{h,protein}/R_{oct}$ in F87 is not seen in F127.

In Figures 5.8C and 5.8D the mobile fraction of proteins, f_m, is shown as a function of increasing $R_{h,protein}/R_{oct}$ for F87 and F127. When $R_{h,protein}/R_{oct}$ is less than 0.7 in either system, f_m is nearly equal to one. A mobile fraction, f_m, close to one means that most protein particles are diffusing throughout the liquid crystalline lattices. As $R_{h,protein}/R_{oct}$ is increased in F87, we observe

a dramatic decrease in f_m to 0.22 as $R_{h,protein}/R_{oct}$ becomes equal to and greater than one. In F87, as the size of the protein $R_{h,protein}$ approaches the size of the interstitial site, R_{oct}, the mobile fraction drops to 0.22. We observe an anomalous decrease in mobile fraction near $R_{h,protein}/R_{oct} = 0.75$ in F87 for HSA at 55°C. It is possible that the corona brush density profile is reaching a regime that locks down HSA at these concentrations and temperatures.

The lowest protein mobility is observed with the protein hydrodynamic radius is closely matched to the interstitial site radius or about 10% larger than the interstitial site radius. The interstitial site radius is calculated with the assumption that the micelles are hard spheres, it is surprising that this approximation is as predictive as it appears. This assumption is useful but ignores the fact that the corona brushes in F87 and F127 have a radial distribution of PEO monomers. They are *not* hard spheres. In F87 samples, up to 78% of proteins are immobilized when $R_{h,protein}/R_{octahedral}$ is between 1 and 1.2. In F127, $R_{h,protein}/R_{octahedral} > 0.81$ is not achieved due to its larger unit cell, however a significant 40% decrease in protein mobile fraction, f_m, as $R_{h,protein}/R_{oct}$ approaches 0.8 in F127 was observed.

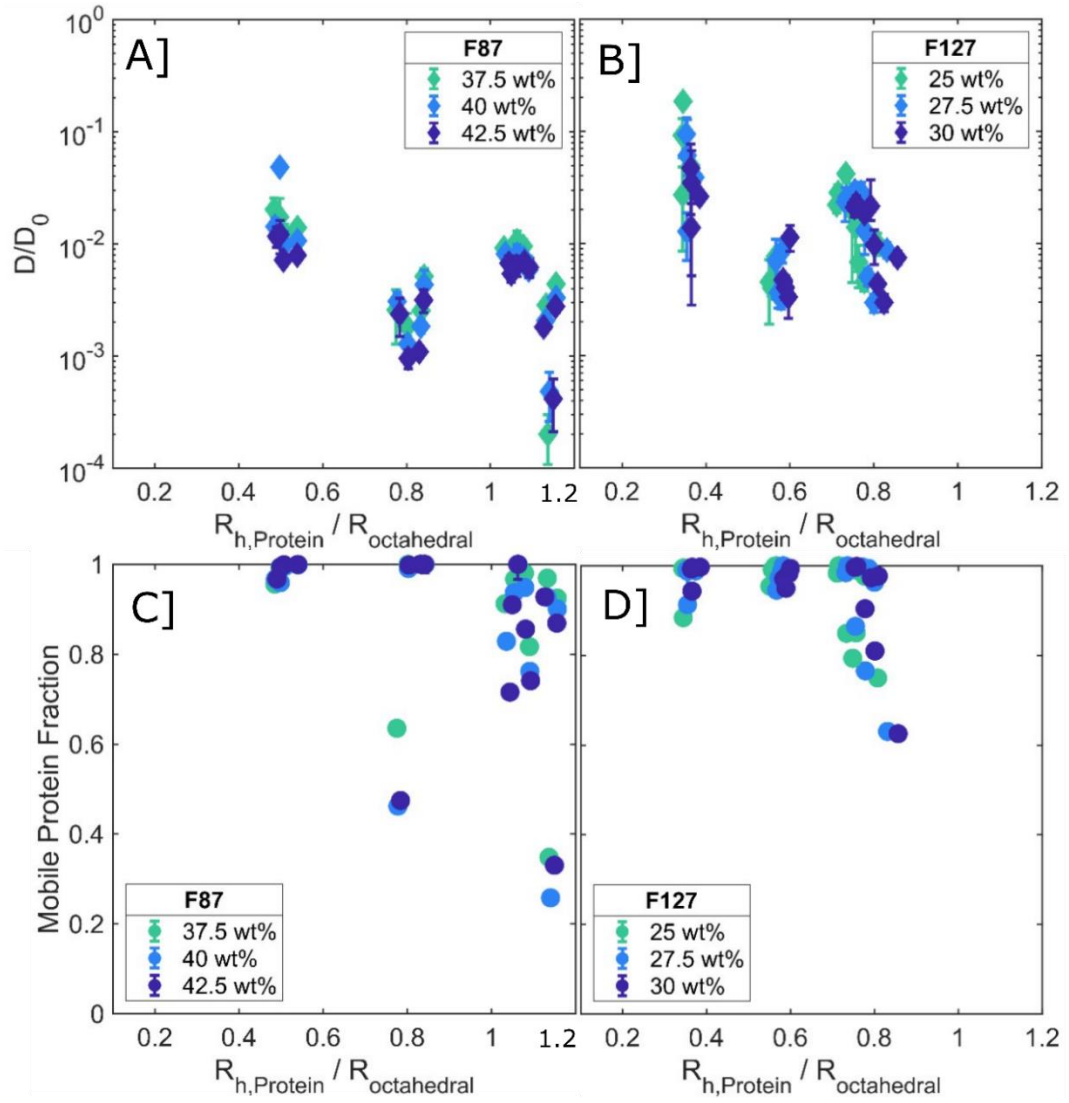

Figure 5.8: Diffusivity data for BSA in **[A, C]** Pluronic F87 and **[B, D]** F127 shown against the protein hydrodynamic radius normalized by the radius of the crystalline octahedral site. **[A, B]** The diffusive component **[C, D]** the mobile fraction of proteins. Up to 78% immobilization is observed in F87 as the protein size becomes larger than the octahedral radius. Error bars are shown but are smaller than the marker size in most cases. *N* = 3.

5.4 Understanding the local protein environment using trends in diffusivity data.

The size of the interstitial site is hypothesized to become a controlling parameter as the radius of the octahedral interstitial site, R_{oct}, approaches the hydrodynamic radius of the protein, $R_{h,protein.}$ Therefore, it is crucial to understand the changes in crystalline lattice size with concentration and temperature. Figure 5.9 shows the interior schematic of the interstitial site. As $R_{oct} \rightarrow R_{h,protein}$ in Figure 5.9B, the PEO coronas of the 6 micelles surrounding the interstitial site are expected to crowd the protein resulting in a drastic decrease in protein mobility. In addition to this crowding effect within the interstitial site the crystalline lattice will sterically hinder the proteins as they diffuse through the continuous aqueous environment. To understand the controlling factors of protein diffusivity in these hierarchical materials, it is crucial to have a quantitative understanding of the nano-scale structures which the protein is moving through.

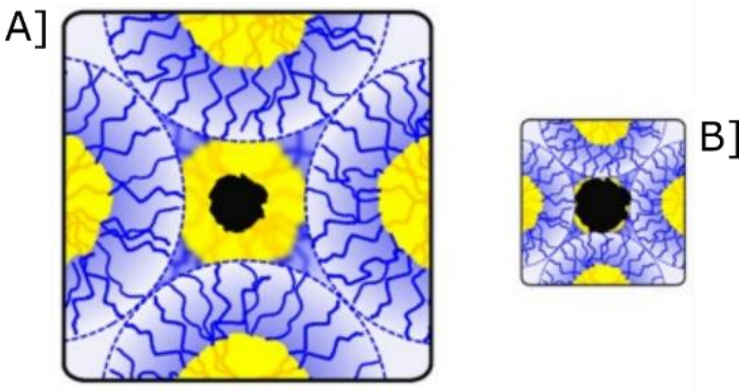

Figure 5.9: Illustrations of a protein confined into an octahedral crystalline site. Proteins are shown as black globules, PEO brushes are shown in blue and PPO cores shown in yellow. In both schematics, the protein is the same radius. Polymers are not drawn to scale. **[A]** $R_{h,protein}/R_{oct} < 1$. In this scenario the protein is free to bounce within the interstitial site, briefly colliding with the micellar PEO brushes **[B]** $R_{h,protein}/R_{oct} \sim 1$. In this scenario the protein is crowded on all sides by contact with the PEO brushes.

To quantify the impact of the aqueous crystalline environment on protein mobility, a simple diffusion model is proposed. The geometric parameters related to crystalline size have been quantitatively measured using SAXS. However other parameters such as PEO corona brush density, and protein movement within the interstitial site are difficult or impossible to measure directly. It is important to understand how these hard-to-measure parameters are changing. A natural framework to describe the protein movement throughout aqueous Pluronic crystals is interstitial hopping. This mechanism of diffusion is commonly seen in solid crystalline materials.[159] This model begins with a simple activated hopping model with only two terms,

$$D = \frac{\sigma\ r^2}{6} \tag{4}$$

Here, *r*, is the hop distance between interstitial sites. For a BCC crystal $r = a\sqrt{3}/4$ where *a* is the size of the unit cell. The second term, σ is the frequency of successful hops,

$$\sigma = Z\,\beta\,e^{-\frac{\Delta E}{kT}} \tag{5}$$

Here *Z* is the number of adjacent interstitial sites available to the protein. For a BCC octahedral site *Z = 4.* The first factor, *β,* is the frequency of hop attempts both successful and unsuccessful. Each protein is constantly bouncing around the interstitial cage. The second factor, $e^{-\frac{\Delta E}{kT}}$, represents the energetic mountain that must be overcome for the protein to successfully make the journey from one interstitial site to the next.

At this point it is important to understand that the octahedral site is not a uniform cage of PEO. It is an aqueous space that is surrounded by 6 spherical micelles. The path of least resistance out of the cage will be the gap on the triangular face of the octahedra, where there is a PEO-free gap. A small enough protein will be able to navigate this gap without any PEO interaction. However, a sufficiently larger protein will only be able to escape the interstitial site by deforming the PEO brushes of the 3 micelles surrounding the gap. The energetic barrier for interstitial hopping, *ΔE*, will be a function of the entropic and enthalpic energy required to deform these brushes so that the radius of the octahedral window is sufficiently large for

the protein to slip through. *ΔE* will therefore be primarily controlled by the radial brush-density profile of PEO in the micellar corona brushes.

The brush-density profile of a micelle within a crystalline structure is not characterized in our measurements. The energetic barrier, *ΔE,* is regarded as the required elastic energy of deformation exerted by the protein onto the brushes,

$$\Delta E \sim k\,\gamma\left(\frac{d_{protein}}{\xi}\right)^2 \tag{6}$$

Here $d_{protein}$ is the diameter of the protein, and ξ is the characteristic spacing of the PEO monomers within the brushes. In a good solvent the characteristic spacing of an unperturbed polymer network scales with concentration as $\xi \sim c^{-3/4}$.[160,161] However, the crystalline arrangement of micelles does not resemble a polymer network or mesh. The PEO density profile throughout the unit cell is not uniform but is instead highly structured in a relatively small corona volume. For a given micelle, the characteristic spacing of monomers in the corona is approximated as the volume of the coronal shell divided by the number of PEO monomers in that shell,

$$\xi \approx \sqrt[3]{\frac{V_{corona}}{\#\ of\ PEO\ monomers\ per\ micelle}} \approx \sqrt[3]{\frac{V_{micelle} - V_{core}}{2 * N_{agg} * PEO_m}} \tag{7}$$

Where the volume of the corona is the volume of the micelle subtracted from the volume of the core. The number of PEO monomers in the micelle is equal to the number of chains per micelle, N_{agg} , multiplied by the number

of PEO monomers per chain, $2PEO_m$. The volume of the micelle is estimated as a hard sphere, using the calculated radius of the micelle, $R_{micelle}$, from SAXS measurements of the crystalline unit cell size, a. For a BCC crystalline lattice, $R_{micelle} = \frac{\sqrt{3}}{4}a$. The volume of the micellar core is estimated as the volume of a sphere containing only PPO monomers. This is calculated as the number of chains per micelle, N_{agg} , multiplied by the volume of PPO monomers per chain, PPO_n. The aggregation number, N_{agg}, is calculated as the number of polymer chains within the crystalline unit cell, divided by the number of micelles, 2, in a BCC unit cell. Finally, we can cancel terms to describe the characteristic spacing of PEO monomers within the micellar coronas which compose the BCC crystalline lattice,

$$\xi \approx \sqrt[3]{\frac{4/3\,\pi\left(\frac{\sqrt{3}}{4}\right)^3 * a^3}{2 * PEO_m * \left(\frac{\rho * a^3 * c * N_{avg}}{2 * MW_{Pluronic}}\right)} - \frac{PPO_n * \rho_{PPO}}{2 * PEO_m}} = \sqrt[3]{\frac{\pi\,\sqrt[2]{3} * MW_{Pluronic}}{16 * PEO_m * \rho * N_{avg}} * \frac{1}{c} - \frac{PPO_n * \rho_{PPO}}{2 * PEO_m}} \quad . (8)$$

Where, $MW_{Pluronic}$ is the molecular weight of the triblock, PPO_n is the number of PPO monomers in the middle block, PEO_m is the number of PEO monomers in the tail blocks, N_{avg} is Avogadro's number, ρ_{PPO} is the volume of each PPO monomer, and ρ is the bulk density of the unit cell. The important scaling to note is that the characteristic spacing of PEO monomers that the protein must displace now scales with bulk concentration of the triblock as $\xi \sim c^{-1/3}$. This leads to a model for interstitial diffusion that relates in a meaningful way to the bulk concentration of the triblock polymer

$$D = a^2 \ \beta \ e^{-\frac{\gamma\left(\sqrt[3]{c} * d_{protein}\right)^2}{T}} \quad . \tag{9}$$

Here *a* is the unit cell parameter as measured via SAXS. This is a function of triblock choice, concentration, and temperature. $d_{protein}$ can be measured in free solution using DLS. β is the frequency of hop attempts and captures the mobility of the protein within the interstitial cage. γ captures the importance of the trend in activation energy with concentration. If γ → 0, increasing the brush density is no longer increasing the energetic barrier regarding hopping from one site to the next.

The diffusivity data for every protein studied here is fit to equation 9, where β and γ are the only fitted parameters. The equation was first linearized by taking the logarithm of both sides, resulting in a linear fit where the slope is proportional to γ and the y intercept is proportional to β. Figure 5.10 shows fits to the diffusivity data for BSA in F87. The quality of these fits is representative of the entire data set, see Figures 5.11 - 5.12 for fits with LYS, HSA, CHA, and BSA from 25-55°C in F87 and F127. In all cases, the proposed model captures the trends in diffusivity well. In Figures 5.10-5.12 we demonstrate that equation 9 is an appropriate functional form to capture trends in protein diffusivity across a range of polymer concentrations and temperatures.

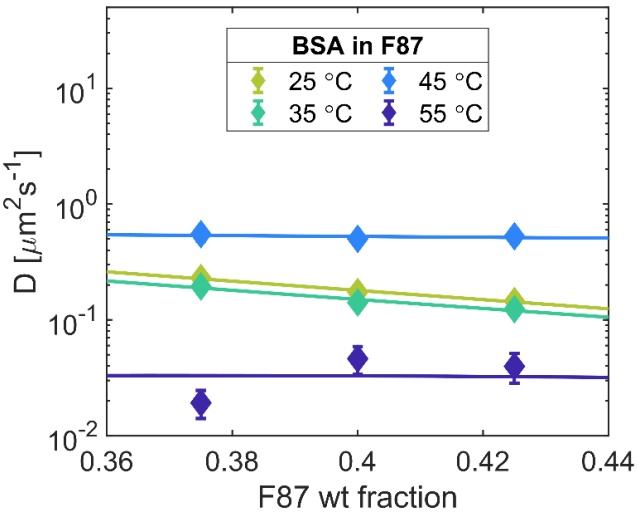

Figure 5.10: Diffusivity of BSA versus concentration of Pluronic F87 at 25, 35, 45, and 55°C. Lines of best fit to equation 9 are shown. Fits to all data are included in supporting information. Error bars are shown but are smaller than the marker size in most cases. *N* = 3.

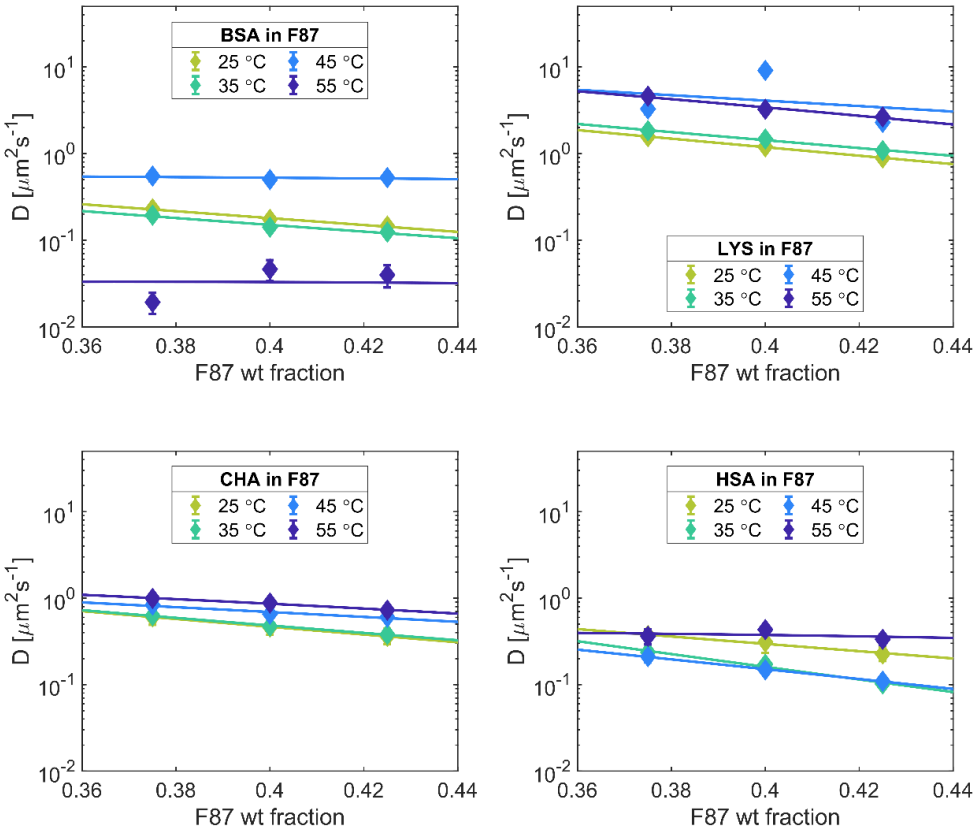

Figure 5.11: Diffusivity of protein v. wt fraction of Pluronic F87 at 25, 35, 45, and 55°C. Lines of best fit to equation 9 are shown. Error bars are shown but are smaller than the marker size in most cases. *N* = 3.

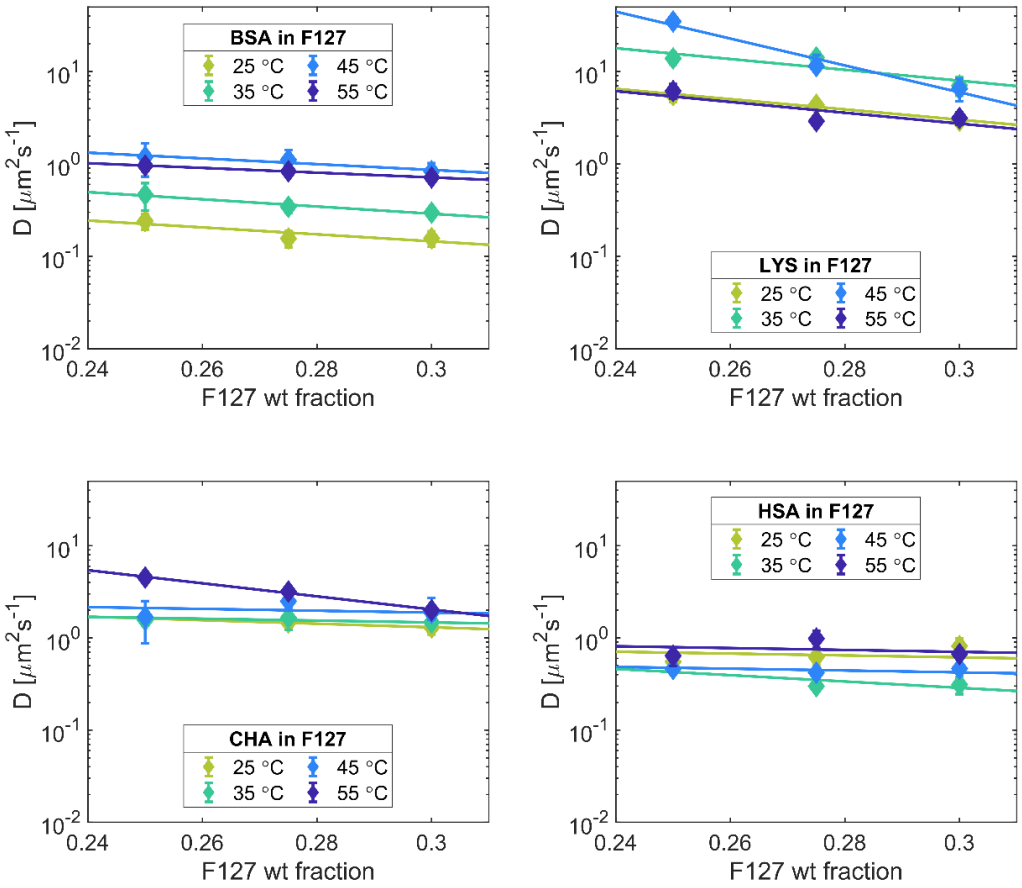

Figure 5.12: Diffusivity of protein v. wt fraction of Pluronic F127 at 25, 35, 45, and 55°C. Lines of best fit to equation 9 are shown. Error bars are shown but are smaller than the marker size in most cases. *N* = 3.

After fitting this interstitial diffusion model to the entire dataset, the impact of brush density on protein immobilization can be elucidated. Figure 5.13 shows the resulting fit parameters β and γ. β is the frequency of hop attempts and captures the mobility of the protein within the interstitial cage. γ captures the importance of the trend in activation energy with concentration.

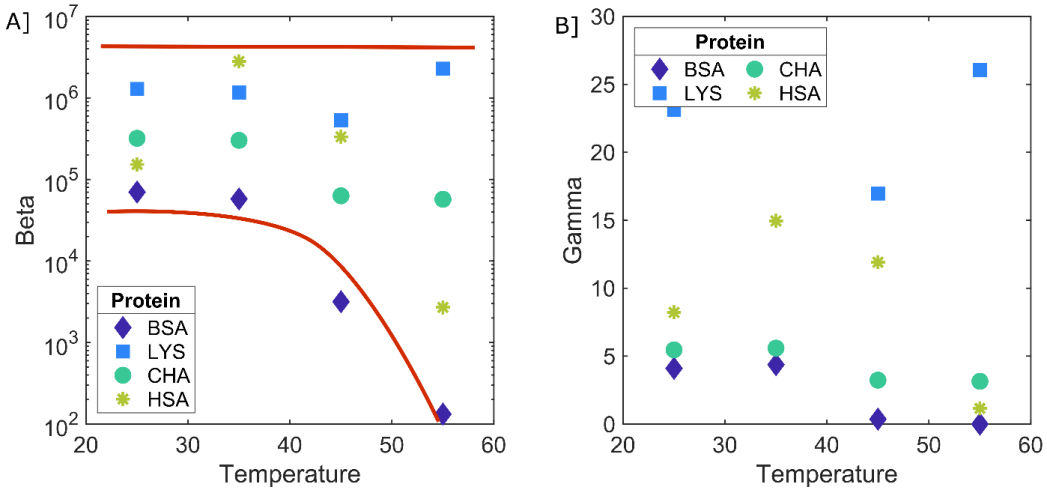

Figure 5.13: Interstitial diffusion hopping model parameters **[A]** $\boldsymbol{\beta}$ and **[B]** γ calculated for all proteins from 25-55 °C for Pluronic F87. $\boldsymbol{\beta}$ is the frequency of hop attempts and captures the mobility of the protein within the interstitial cage. γ captures the importance of the trend in activation energy with concentration. **[A]** Red lines drawn to guide the eye.

5.5 Conclusions

A methodology to quantify mobility of proteins in the continuous phase of self-assembled liquid crystals has been demonstrated. By building off the knowledge in Chapters 2-4, we are able to target block polymer systems with desirable crystalline structures of the proper size for protein dispersion. Rheological measurements facilitated the formulation of triblock systems with a workable order-to-disorder transition and a consistent modulus while in the solid-like state. Proteins were fluorescently labeled and dispersed throughout liquid crystalline systems showing favorable rheological properties. High-throughput fluorescence recovery after photobleaching (FRAP) experiment was used to measure the diffusion coefficient and mobile fraction of proteins dispersed in the aqueous continuous phase. A nearly four order of magnitude decrease of protein diffusivity within the liquid crystalline environment is observed in comparison to free solution. In F87 at 40 wt% up to 78% of proteins are immobilized at 55°C. During the ~24-hour long experiment, the 22% of proteins in this that were still mobile diffused over 1000x slower than in free solution. A substantial decrease in protein mobility is reported along with significantly enhanced protein confinement in F87 and F127 liquid crystals in comparison to free solution.

By changing the protein dispersed throughout the liquid crystal, the impact of protein radius on diffusivity was characterized. Structural data obtained via synchrotron small angle X-ray scattering (SAXS) was used to

normalize the size of the protein by the size of the aqueous interstitial site which the protein primarily resides in at all concentrations and temperatures. The size of the protein is found to be a controlling factor of protein mobility throughout liquid crystalline structures; however, one must consider the protein size *relative* to the size of the aqueous interstitial environment. This analysis requires thorough quantification of the nano-scale structure, which will be impacted by changes to formulation and storage conditions.

Further analysis of the diffusivity data can be used to gain insights into the interstitial pocket environment. An interstitial hopping model was applied to the diffusion coefficients measured in F127 and F87. Systems where β is significantly lowered are slowing protein mobility within the interstitial site by crowding. Increasing PEO corona brush density is an important way to increase the activation energy of hopping but only to a certain point. An unambiguous model was developed that shows that the shows the importance of the corona brushes for protein diffusivity. Liquid crystalline and particle meta-materials demonstrate macroscopic properties that arise from the nano-scale structure. Particle or proteins can be incorporated into the formulation of meta-materials either as cargo or tune the macroscopic material properties. It is paramount to accurately understand the geometry of the crystalline environment relative to the protein or particle size to understand the mechanism of diffusion through self-assembled liquid crystalline networks.

Chapter 6 Pluronic crystalline lattices to protect proteins from thermal denaturation

The global market for protein therapeutics is projected to reach $217 *billion* by 2023.[162] These protein drugs include vaccines, antivenins, cancer treatments, and monoclonal antibody therapies. Unfortunately, proteins are extremely prone to 1) aggregation and 2) thermal unfolding, which causes loss of functionality and detrimental side effects such as organ failure and anaphylaxis. Current technologies to stabilize proteins include spray/freeze drying, confinement in sugar glasses, and storage in solution but all require refrigeration or freezing. Without reliable power, maintaining cold storage can be prohibitively expensive or simply impossible in underdeveloped countries, war zones, and areas affected by natural disaster. Circumventing the need for cold storage will drastically increase access to these live changing treatments.

Proteins are stable at temperatures much higher than cold storage in the crowded intracellular environment, where concentrations of macromolecules can exceed 30-40 vol%.[141] To mimic this environment, confinement[141,142] and macromolecular crowding[145,146,163] have been investigated as protein protection mechanisms. The aqueous, polymer-dense interstitial spaces in self-assembled liquid crystalline meta-materials may be tuned to mimic the intracellular environment, which could enhance protein protection from thermal denaturation and aggregation. The proteins

can be readily dispersed throughout the liquid crystalline matrix via thermo-reversible melting of the matrix (Figure 6.1).

In Chapter 5 of this thesis the mobility of proteins throughout these self-assembled crystalline lattices matrices was thoroughly quantified. Fluorescence Recovery After Photobleaching, FRAP, was used to determine the diffusivity of proteins in the aqueous spaces that permeate the crystalline lattices formed by the triblock micelles. Our analysis of the FRAP dataset splits the observed recovery after photobleaching into two parts. The first part of the intensity recovery represents a diffusive component with a given timescale. The second part of the intensity recovery represent the immobile fraction of molecules. We observe up to 78% protein immobilization when BSA is incorporated into Pluronic F87 samples, at the end of the 24 hour long FRAP experiment the intensity within the photobleached region only recovered 22% of the original fluorescence intensity (Figure 6.2). This could represent an increase in confinement of the proteins to the interstitial sites.

This chapter is the culmination of the design approach outlined throughout this thesis to understand, process, and optimize materials with liquid crystalline structures. In Chapter 5 we determined the controlling parameters to enhance protein immobilization in Pluronic liquid crystalline matrices. Here we attempt to link the drastic decrease in protein mobility to protection from thermal denaturation using UV-Vis spectroscopy.

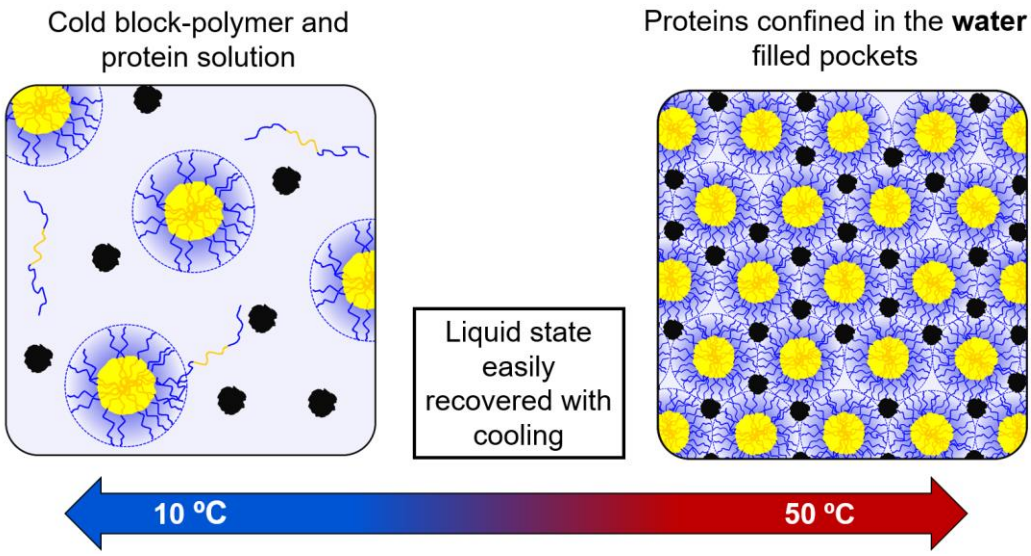

Figure 6.1: *Proteins captured in a spontaneously self-assembled structure.* Below the order-disorder transition temperature (~ 10°C), an aqueous dispersion of Pluronic® (PEO-PPO-PEO) and proteins (●) is formed. Upon heating the PPO blocks pack into hydrophobic cores (●) surrounded by aqueous PEO brushes. The micelles spontaneously arrange into crystalline phases. The proteins are guided to the aqueous pockets between micelles

Small angle X-ray scattering measurements were used to quantify the size of the aqueous interstitial site relative to the protein size. From this dataset we were able to determine the effect of protein size relative to the aqueous chamber size on protein diffusivity. As the radius of the protein meets and exceeds the hard-sphere radius of the interstitial site, a drastic decrease in diffusivity is observed. This could be evidence of enhanced macromolecular crowding and confinement in these systems.

6.1 A targeted denaturation study using our design principles.

During Fluorescence Recovery After Photobleaching studies (Chapter 5) we observed a marked decreases in BSA diffusivity when dispersed throughout the liquid crystalline lattices formed by Pluronic F87 micelles. Specifically, BSA diffusivity was observed to be between 300 and 9,000 times slower than free solution diffusivity in Pluronic F87 liquid crystalline lattices in concentrations ranging from 37.5 - 42.5wt%. This effect is temperature dependent. Between 25 and 45°C, the diffusivity was between 300 and 900 times slower than diffusivity in bicarbonate buffer alone. However, at 55°C we observed diffusivities between 4,000 and 9,000 times slower. Figure 6.2 highlights this distinct drop in protein mobility that is coupled with a corresponding drop in protein mobile fraction. We hypothesized that a marked decrease in protein diffusivity could indicate high levels of protein confinement and macromolecular crowding.

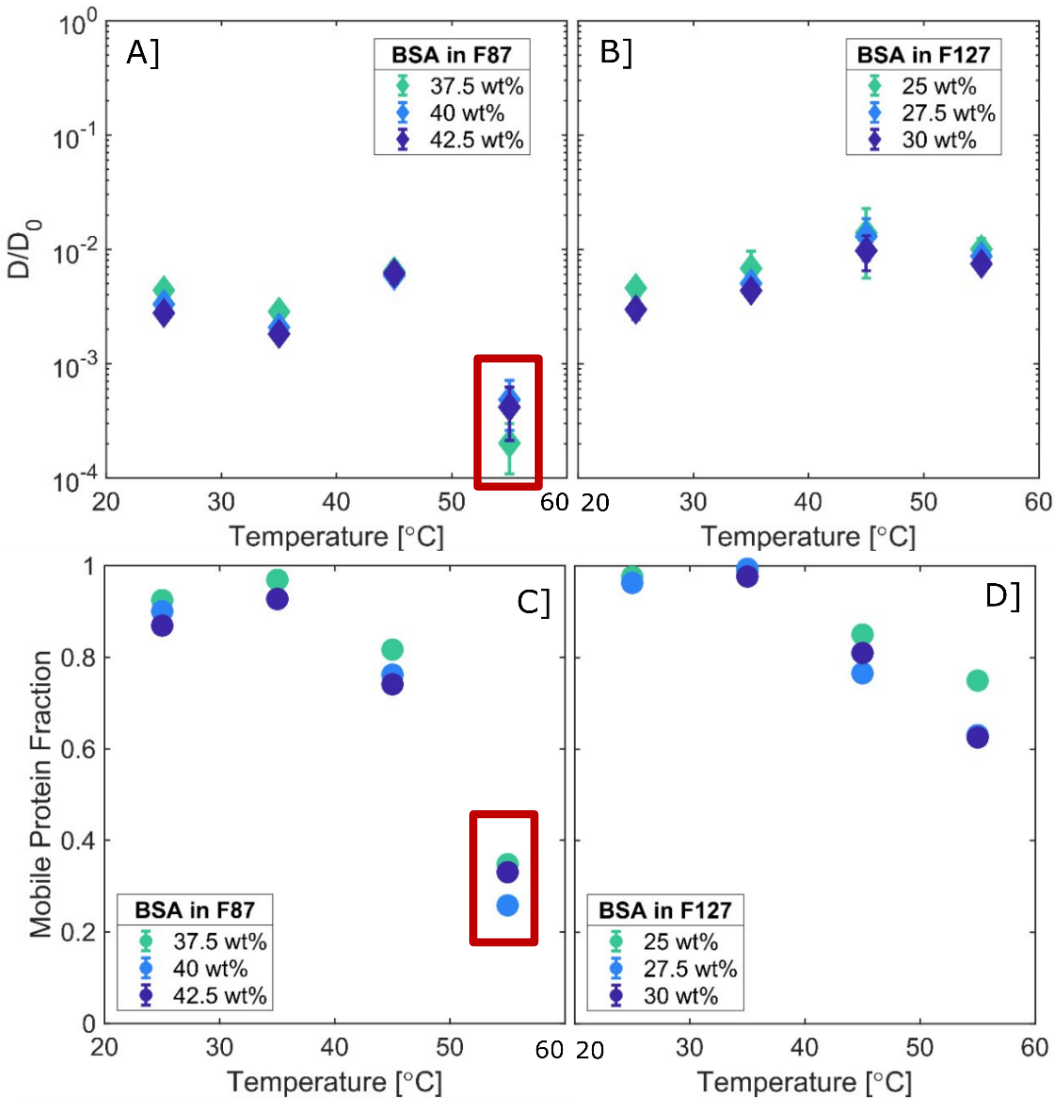

Figure 6.2: Normalized Diffusivity data for BSA in **[A]** Pluronic F87 and **[B]** F127. The data is normalized by the diffusivity of the proteins in polymer-free bicarbonate buffer at the temperature indicated. The mobile fraction of proteins as calculated during FRAP diffusivity fitting for BSA in **[C]** Pluronic F87 and **[D]** F127. Error bars are shown but are smaller than the marker size in most cases. Red boxes highlight the region of interest that we hypothesized could provide enhanced protection from thermal denaturation.

We seek to test the hypothesis that Pluronic liquid crystalline systems can be used to protect proteins from thermal denaturation by enhancing macromolecular crowding and confinement. Protein and polymer combinations showing the greatest changes in protein mobility are the best targets to observe any potential enhanced protection against thermal denaturation. The focus our denaturation studies is BSA dispersed throughout Pluronic F87 42.5 wt%, which showed the most dramatic decrease in protein diffusivity.

6.2 Observation of protein denaturation by UV-Vis spectroscopy

The Beer-Lambert law is a well-known relationship to establish the concentration of an absorbing species in solution. Absorbance is often wavelength dependent, so a calibration process must be carried out to establish the concentration dependence of absorbance *as a function of wavelength.* This process is widely used to quickly establish protein concentrations in solution with good accuracy.[164]

There exists a subset of absorbing species, which include certain proteins, where the absorbance of light also depends on the local solution environment. For these proteins, as the protein unfolds or denatures the absorbance spectrum will shift.[164–167] Irreversible denaturation will result in a permanently shifted absorption spectra. Three commonly seen aromatic amino acid side chains (tryptophan, tyrosine, and phenylalanine) all have absorption bands in the range of 250-320 nm. The wavelength dependent

absorption of these bands depend on the polarity of the local solvent environment.[168] These properties of the amino acid side chains allow study of protein denaturation by UV-Vis spectroscopy.[169]

UV-vis spectroscopy is a useful and widely available technique for protein denaturation studies. In theory – the absorbance of the amino acid side chains should follow the Beer-Lambert Law, along with the proteins containing them. Complications can arise when the concentration of the protein is too high, the sample is highly fluorescent, or the sample is chemically instable.

6.3 Materials and Methods

Pluronic F87 [PEO_{75}-PPO_{46}-PEO_{75}] (BASF, lot# 0008779132) was used as received. Bicarbonate buffer (pH = 9) was freshly made with purified 18.2 MΩ·cm water before sample preparation. Bovine serum albumin, BSA (Sigma Aldrich, lot# SLCC2453) was purchased and used as received. BSA was first dispersed into bicarbonate buffer at a concentration of 30 mg/mL. Aliquots of this solution were added to pre-weighed amounts of F87 triblock polymer in 2 mL vials. Extra bicarbonate buffer was added to obtain a protein concentration of 5x10-5 mmol/mL. This concentration was chosen to keep samples sufficiently dilute, there will always be less 1 protein per crystalline unit cell. The 2mL vials of protein and triblock solution were mixed end over end at 8°C for at least 24 hours to ensure sufficient dispersion and dissolution of the polymer. Samples were used for UV-Vis absorption measurements within 48 hours of preparation. Absorbance measurements were performed using a Cary 300 Scan UV–Visible Spectrophotometer. For all measurements reported, the absorbance of the solution or block polymer crystalline phase is subtracted from the absorbance spectra to obtain the absorbance spectra of the BSA proteins alone.

6.4 Effect of liquid crystalline matrix protection on protein denaturation

The UV absorption spectra of BSA dispersed into a crystalline matrix of Pluronic F87 micelles dramatically shifts during temperature ramps from 25°C to 75°C at a rate of 1°C/min (Figure 6.3A). At 25°C, BSA demonstrates a peak in absorbance at 240 nm, followed by a broader peak in absorbance between 270 and 290nm. These peaks in absorbance overlap to form a saddle pattern with a minimum between 250 and 255 nm. During the heating ramp, a 36% increase in absorbance of light in the 250-255 nm range is observed, which could signify a substantial change in the local environment around absorbing amino acids residing in the protein core. During subsequent cooling of the sample from 75°C to 25°C at a rate of 1 °C/min (Figure 6.3B), the absorbance does not return to the original spectra observed at 25°C. After heating the sample from 25°C to 75°C, we observe a slight flattening of the spectra between 240 and 290 nm during cooling. The thermal cycle from 25°C → 75°C→ 25°C irreversibly changes the absorbance spectra of BSA trapped in the aqueous interstitial spaces of Pluronic F87 liquid crystals. However, it should be noted that the BSA samples in Pluronic F87 remained optically transparent during and after the extended heating cycle – evidence supporting that the crystalline lattice prevents aggregation of BSA throughout the entire temperature range.

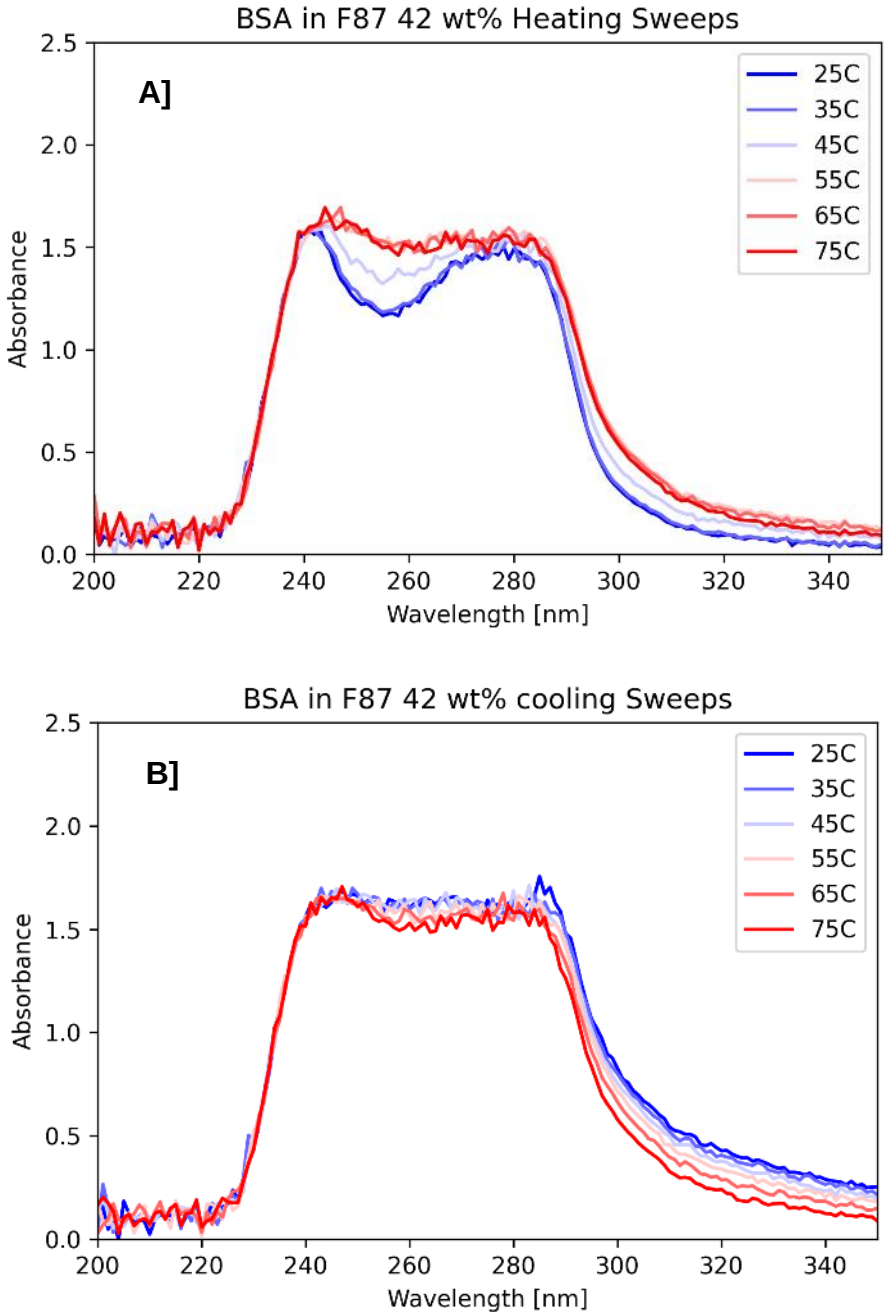

Figure 6.3: UV-Vis absorbance spectra of BSA in Pluronic F87 42wt% during **A]** heating from 25 to 75C at a rate of 1°C /min and **B]** subsequent cooling from 75 to 25°C at a rate of 1 °C/min.

The UV absorption spectra of BSA dispersed into bicarbonate buffer irreversibly shifts during temperature ramps from 25°C to 75°C at a rate of 1 °C/min (Figure 6.4A). At 25°C, BSA demonstrates a peak in absorbance at 240 nm, followed by a broader peak in absorbance between 270 and 290nm. These peaks in absorbance overlap to form a saddle pattern with a minimum between 250 and 255 nm. During the heating ramp an increase in absorbance of light in the 250-255 nm range is observed until the absorbance from 240-290 nm plateaus. This could signify a substantial change in the local environment of the amino acids residing in the protein core. During subsequent cooling of the sample from 75°C to 25°C at a rate of 1 °C/min (Figure 6.4B), the absorbance does not return to the original spectra observed at 25°C. After heating the sample from 25°C to 75°C, we observe a slight flattening of the spectra between 240 and 290 nm during cooling back to 25°C. However, the absorbance spectra of BSA does not return to the original spectra observed at 25°C. This is in agreement with observed structural changes in BSA in neutral buffer, which have shown to be reversible up to 45°C, and only partially reversible up to 65°C [170]. The thermal cycle from 25°C → 75°C→ 25°C irreversibly changes the absorbance spectra of BSA in bicarbonate buffer.

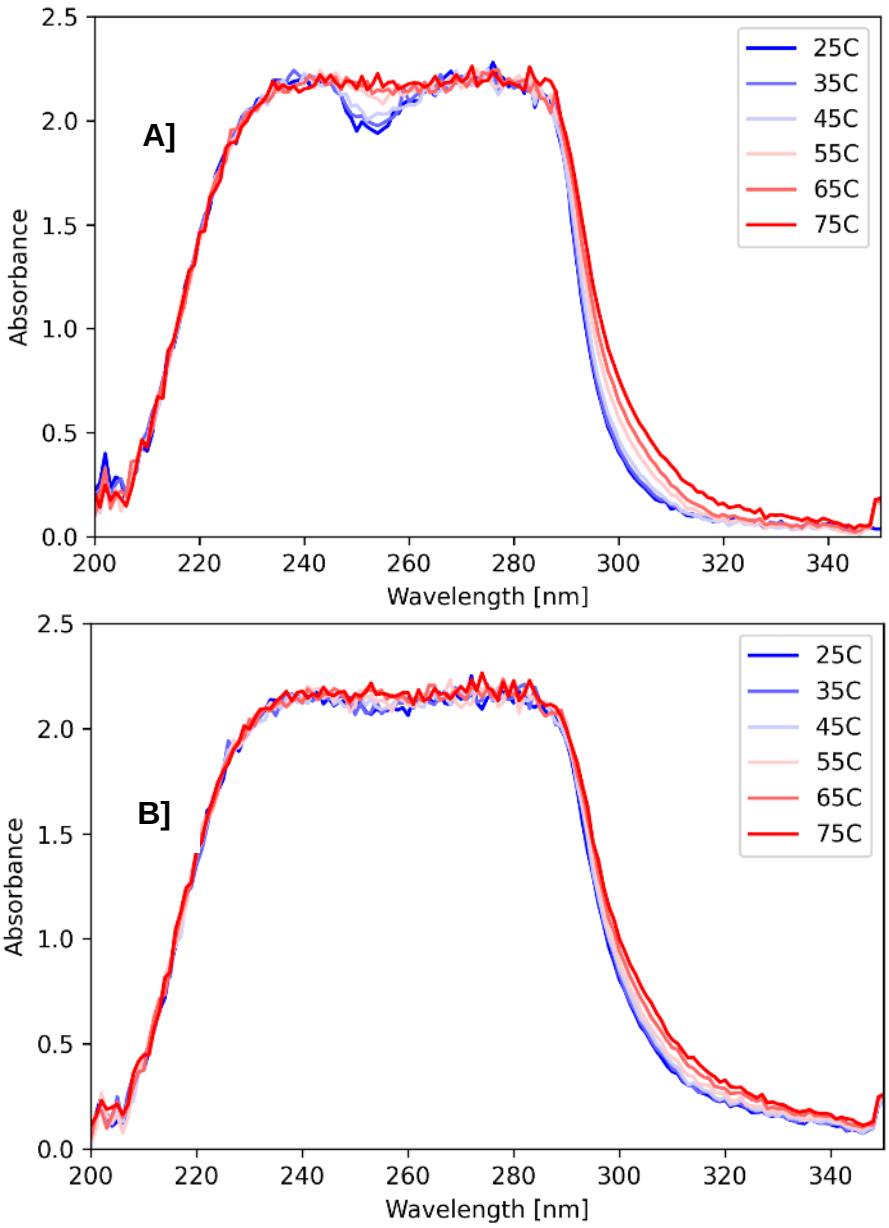

Figure 6.4: UV-Vis absorbance spectra of BSA in bicarbonate buffer during **A]** heating from 25 to 75C at a rate of 1°C/min and **B]** subsequent cooling from 75 to 25°C at a rate of 1°C /min.

The largest change in BSA absorbance during the temperature sweeps was observed between 250 and 255 nm. Figure 6.5 shows the mean absorbance between 250 and 255 nm during the thermal cycle from 25°C → 75°C → 25°C at a rate of 1°C/min. Red lines show data during the initial heating ramp from 25°C → 75°C. Blue lines show data from the subsequent cooling ramp from 75°C → 25°C. The solid lines show absorbance data for BSA in a 42 wt% Pluronic F87 liquid crystalline matrix. The dashed lines show absorbance data for BSA in bicarbonate buffer alone. For both samples, the absorbance remains altered after returning to 25°C. This could signify a substantial change in the local environment of the amino acids residing in the protein core. A denaturation of the protein's structure would expose the amino acid groups that originally resided in the protein core to the aqueous solvent surrounding the molecule.

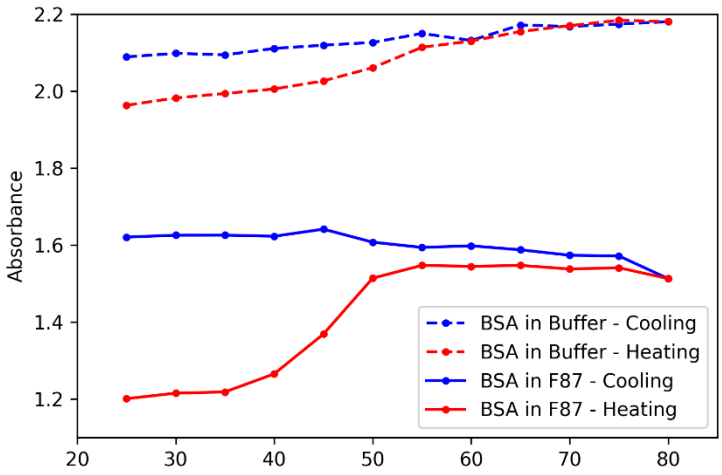

Figure 6.5: Mean absorbance of BSA from 250-255 nm in bicarbonate buffer (dashed lines) and in Pluronic F87 42.5 wt% (solid lines) during thermal cycling from 25°C → 75°C → 25°C at a rate of 1°C/min.

6.5 Conclusions

UV-Vis spectroscopy is used to evaluate the ability of a self-assembled liquid crystalline matrix to protect a globular protein from thermal denaturation. In chapter 5 of this thesis, it was found that BSA diffuses up to 9,000 times slower when dispersed into the aqueous spaces throughout self-assembled Pluronic F87 liquid crystals in comparison to diffusivity in bicarbonate solution alone. This drastic reduction in protein mobility was observed even at the high temperature of 55°C. To investigate if this reduction in mobility corresponds with increased protection from thermal denaturation, we use UV-Vis spectroscopy to track the absorption spectra of the amino acids composing BSA. Absorbance spectra were collected during thermal cycles from 25°C → 75°C → 25°C at a rate of 1°C/min for BSA in bicarbonate buffer alone, and BSA dispersed throughout a 42 wt% Pluronic F87 crystalline lattice.

We find that the Pluronic matrix does not enhance protection against thermal denaturation in comparison to bicarbonate buffer alone. However, the Pluronic matrix could be preventing widespread aggregation of the BSA proteins as evidenced by a lack of optical clouding. For both samples, the absorbance remains drastically altered after thermal cycling from 25°C to 75°C. This could signify a substantial change in the local environment of the amino acids residing in the protein core. A denaturation of the protein's structure would expose the amino acid groups that originally resided in the protein core to the aqueous solvent surrounding the molecule.

The drastic four orders of magnitude reduction in mobility of BSA in F87 with a corresponding 78% immobile fraction observed in Chapter 5 could indicate increased protein confinement and crowding. However, any possible enhancement of the protein confinement and crowding mechanisms do not translate to quantifiable protection from thermal denaturation as measured by UV-Vis spectroscopy. We observe a lack of optical clouding in the Pluronic F87 + BSA samples even after an extensive thermal cycle up to 75°C, which implies the lack of large aggregate formation. There exists the potential to use this technology to prevent thermally induced aggregation in protein samples.

Chapter 7 Conclusions

The goal of this work is to develop accessible methods to characterize the nanoscale structure and mechanical properties of lyotropic liquid crystals in diblock copolymer solutions. The result is a comprehensive set of methods to better characterize new materials with aqueous block polymer crystalline structures, understand thermal and shear history effects, and to guide formulation attempts to achieve desirable properties in the final material.

In Chapter 2, the limitations of predictive theories for block polymer crystalline phase formation are explored. A brief review of phase behavior of linear diblock (AB) and triblock (ABA) block polymers in solvents with preferential selectivity for one of the blocks shows significant complexity. Limitations predicting phase behavior even in simple binary polymer and solvent solutions warrant further experimental and theoretical study. We demonstrate the utility of existing literature data, which should be leveraged at the start of any material design effort. Techniques such as rheological characterization and small angle scattering are used to map the crystalline phase space of several block polymer systems. Rheological studies have provided enormous insights into the properties and flow mechanisms of these materials. When coupled with small angle scattering data, the nanoscale structures can be linked to these macroscopic properties. The liquid crystalline structures formed have an enormous impact on the possible flow mechanisms, which dictate the material's response to external

shear fields during processing. These methods will be useful for formulation attempts that leverage self-assembled crystalline lattices in block polymer systems to produce desirable macroscopic properties.

This base knowledge is then used in Chapter 3 to demonstrate a new method for fingerprinting Face Centered Cubic and Body Centered Cubic crystalline phases in a diblock polymer system. This technique uses widely available rheological methods to gain insights to the crystalline order. These methods are higher-throughput and widely available in comparison to small-angle scattering methods. Approaches like this can be used to rapidly probe new block polymer systems for regions of interest before delegating precious time and resources to small angle scattering experiments.

The low modulus of block polymer crystalline systems in comparison to metals unlocks a wide range of shear processing options. In chapter 4, we demonstrate that oscillatory shear processing can accelerate phase transitions at a tunable rate in block polymer systems. A phase transition that normally occurs on the timespan of months is successfully accelerated to occur within minutes. Shear processing accelerates the phase transition from BCC ➞ A15 by several orders of magnitude as compared to the quiescent case. At f = 1 and 9.9 Hz, increasing the shear rate increases the rate of A15 formation. In contrast, at the lowest applied frequency 0.1 Hz, increasing the shear rate slows the rate of A15 formation. This affect is dependent on the shear amplitude and frequency, providing a toolset for scientists to tune the speed of this transition via shear processing. The

shear-modulated control of these various transformations likely stems from complex changes in the frequencies of interparticle collisions, micelle rearrangements with minimal coronal overlap, intermicellar chain exchange, and activation of slip systems within the polycrystalline domains of the material. These findings illustrate the potential for shear processing to control the rates of phase transitions in self-assembled structures in soft matter. Processing techniques will be essential to many industrial and academic use cases where control of the nanoscale crystalline structure is crucial.

In Chapters 5 and 6, we demonstrate the application of our comprehensive approach to material design. These methods are successfully used to plan and carry out a set of experiments to quantify the mobility of proteins throughout cubic block polymer crystalline networks. The experimental design accounts for the desired properties of the final materials that will be used to study protein mobility within the block polymer crystalline structures. These methods are informed by the guiding principles for understanding block polymer crystalline structure and processing effects. To effectively explore this design space, the following constraints are introduced:

1. The material must experience a reversible order-disorder transition below room temperature but above the freezing point of the buffer solvent ($-5 < T_{ODT} < 15$ °C). This will facilitate the mechanism of protein dispersion outlined in Figure 5.1.

2. The ideal material will be a gel-like solid within the temperature range of interest (25-55°C) to facilitate protein storage.
3. There should not be phase transitions within the temperature range of interest, as this could disrupt protein confinement. Complications arising from crystalline order transitions are avoided, allowing the formulator to fine-tune the crystalline structure in a controllable manner.
4. The buffer chosen should be able to maintain a pH far from the isoelectric point of the protein. Avoiding the isoelectric point will increase protein stability and resistance to aggregation.

With these constraints in place, the design space is large but manageable. Working with block polymer crystalline materials is complicated – the addition of additives, temperature history, and shear processing can all drastically change the crystalline order. It is important to have well defined goals from the beginning to focus structural characterization and tuning efforts.

Rheological measurements facilitated the formulation of triblock systems with a workable order-to-disorder transition and a consistent modulus while in the solid-like state. Proteins were fluorescently labeled and dispersed throughout liquid crystalline systems showing favorable rheological properties. A high-throughput fluorescence recovery after photobleaching (FRAP) experiment was used to measure the diffusion coefficient and mobile fraction of proteins dispersed in the aqueous

continuous phase. A substantial decrease in protein mobility is reported along with significantly enhanced protein confinement in F87 and F127 liquid crystals in comparison to free solution. Structural data obtained via synchrotron small angle X-ray scattering (SAXS) was used to normalize the size of the protein by the size of the aqueous interstitial site which the protein primarily resides in at all concentrations and temperatures. The size of the protein is found to be a controlling factor of protein mobility throughout liquid crystalline structures; however, one must consider the protein size *relative* to the size of the aqueous interstitial environment. This analysis requires thorough quantification of the nano-scale structure, which will be impacted by changes to formulation, processing, and storage conditions.

Further analysis of the diffusivity data can be used to gain insights into the interstitial pocket environment. An interstitial hopping model was applied to the diffusion coefficients measured in F127 and F87. This unambiguous model shows the importance of the corona brushes for protein diffusivity. Increasing PEO corona brush density is an important way to increase the activation energy of hopping but only to a certain point. Liquid crystalline and particle meta-materials demonstrate macroscopic properties that arise from the nano-scale structure. Particle or proteins can be incorporated into the formulation of meta-materials either as cargo or tune the macroscopic material properties. It is paramount to accurately understand the geometry of the crystalline environment relative to the

protein or particle size to understand the mechanism of diffusion through self-assembled liquid crystalline networks

The coordinated FRAP studies in Chapter 5 were used to successfully identify block polymer and protein formulations that most impacted protein mobility, with the hypothesis that these samples would best protect proteins from denaturation. UV-Vis spectroscopy is then used to evaluate the ability of self-assembled liquid crystalline matrix to protect a globular protein from thermal denaturation. It was found that BSA diffuses up to 9,000 times slower when dispersed into the aqueous spaces throughout self-assembled Pluronic F87 liquid crystals in comparison to diffusivity in bicarbonate solution alone. This drastic reduction in protein mobility was observed even at the high temperature of 55°C. To investigate if this reduction in mobility corresponds with increased protection from thermal denaturation, we use UV-Vis spectroscopy to track the absorption spectra of the amino acids composing BSA.

We find that the Pluronic matrix does not enhance protection against thermal denaturation in comparison to bicarbonate buffer alone. However, the Pluronic matrix could be preventing widespread aggregation of the BSA proteins as evidenced by a lack of optical clouding. For both samples, the absorbance remains drastically altered after thermal cycling, which could signify a substantial change in the local environment of the amino acids residing in the protein core. A denaturation of the protein's structure would expose the amino acid groups that originally resided in the protein core to

the aqueous solvent surrounding the molecule. The drastic 4 orders of magnitude reduction in mobility of BSA in F87 with a corresponding 78% immobile fraction observed in Chapter 5 could indicate increased protein confinement and crowding. However, any possible enhancement of the protein confinement and crowding mechanisms do not translate to quantifiable protection from thermal denaturation as measured by UV-Vis spectroscopy. We observe a lack of optical clouding in the Pluronic F87 + BSA samples even after an extensive thermal cycle up to 75°C, which implies the lack of large aggregate formation. There exists the potential to use this technology to prevent thermally induced aggregation in protein samples.

Throughout this work, a set of protocols to characterize the nanoscale structure and mechanical properties of lyotropic liquid crystals in diblock copolymer solutions is established. The result is a comprehensive set of methods to better characterize new materials with aqueous block polymer crystalline structures, understand thermal and shear history effects, and to guide formulation attempts to achieve desirable properties in the final material. Materials with nanoscale structures composed of block polymer crystals are complex, and subject to new constraints in comparison to other polymeric materials. Engineers, scientists, and formulators working with block polymer crystals will need to expand their existing skillsets and knowledge to develop new materials that leverage the unique properties of these fascinating self-assembled structures.

References

(1) Hamley, I. Block Copolymers in Solution: Fundamentals and Applications. In *Chapter 3.9 Concentrated Solutions: Flow Alignment*; Wiley: Chichester, England, 2012; pp 149–158.

(2) Hyde, S. T. Identification of Lyotropic Liquid Crystalline Mesophases. *Handb. Appl. Surf. Colloid Chem.* **2001**, 299.

(3) Lodge, T. P.; Pudil, B.; Hanley, K. J. The Full Phase Behavior for Block Copolymers in Solvents of Varying Selectivity. *Macromolecules* **2002**, *35*, 4707–4717.

(4) Alexandridis, P. Poly(Ethylene Oxide)/Poly(Propylene Oxide) Block Copolymer Surfactants. *Curr. Opin. Colloid Interface Sci.* **1997**, *2*, 478–489.

(5) Sarkar, B.; Alexandridis, P. Block Copolymer-Nanoparticle Composites: Structure, Functional Properties, and Processing. *Progress in Polymer Science*. 2015.

(6) Pozzo, D. C.; Hollabaugh, K. R.; Walker, L. M. Rheology and Phase Behavior of Copolymer-Templated Nanocomposite Materials. *J. Rheol.* **2005**, *49*, 759–782.

(7) Dumortier, G.; Grossiord, J. L.; Agnely, F.; Chaumeil, J. C. A Review of Poloxamer 407 Pharmaceutical and Pharmacological Characteristics. *Pharm. Res.* **2006**, *23*, 2709–2728.

(8) Garti, N.; Mezzenga, R.; Somasundaran, P. *Self-Assembled Supramolecular Architectures: Lyotropic Liquid Crystals*; Garti, N., Somasundaran, P., Mezzenga, R., Eds.; Wiley: Hoboken, N.J, 2012.

(9) Lodge, T. P.; Pudil, B.; Hanley, K. J. The Full Phase Behavior for Block Copolymers in Solvents of Varying Selectivity. *Macromolecules* **2002**, *35*, 4707–4717.

(10) Park, M. J.; Bang, J.; Harada, T.; Char, K.; Lodge, T. P. Epitaxial Transitions among FCC, HCP, BCC, and Cylinder Phases in a Block Copolymer Solution. *Macromolecules* **2004**, *37*, 9064–9075.

(11) Walz, M.; Wolff, M.; Voss, N.; Zabel, H.; Magerl, A. Micellar Crystallization with a Hysteresis in Temperature. *Langmuir* **2010**, *26*, 14391–14394.

(12) Park, M. J.; Char, K.; Bang, J.; Lodge, T. P. Interplay between Cubic and Hexagonal Phases in Block Copolymer Solutions. *Langmuir* **2005**, *21*, 1403–1411.

(13) LaFollette, T. A.; Walker, L. M. Structural and Mechanical Hysteresis at the Order-Order Transition of Block Copolymer Micellar Crystals. *Polymers (Basel).* **2011**, *3*, 281–298.

(14) Frank, F. C.; Kasper, J. S. Complex Alloy Structures Regarded as Sphere Packings. II. Analysis and Classification of Representative Structures. *Acta Crystallogr.* **2002**, *12*, 483–499.

(15) Ungar, G.; Liu, Y.; Zeng, X.; Percec, V.; Cho, W. D. Giant Supramolecular Liquid Crystal Lattice. *Science.* **2003**, *299*, 1208–1211.

(16) Lee, S.; Bluemle, M. J.; Bates, F. S. Discovery of a Frank-Kasper σ Phase in Sphere-Forming Block Copolymer Melts. *Science.* **2010**, *330*, 349–353.

(17) Chanpuriya, S.; Kim, K.; Zhang, J.; Lee, S.; Arora, A.; Dorfman, K. D.; Delaney, K. T.; Fredrickson, G. H.; Bates, F. S. Cornucopia of Nanoscale Ordered Phases in Sphere-Forming Tetrablock Terpolymers. *ACS Nano* **2016**, *10*, 4961–4972.

(18) Huang, M.; Hsu, C.-H.; Wang, J.; Mei, S.; Dong, X.; Li, Y.; Li, M.; Liu, H.; Zhang, W.; Aida, T.; Zhang, W.-B.; Yue, K.; Cheng, S. Z. D. Selective Assemblies of Giant Tetrahedra via Precisely Controlled Positional Interactions. *Science.* **2015**, *348*, 424–428.

(19) Bates, C. M.; Bates, F. S. 50th Anniversary Perspective: Block Polymers-Pure Potential. *Macromolecules* **2017**, *50*, 3–22.

(20) Jo, G.; Ahn, H.; Park, M. J. Simple Route for Tuning the Morphology and Conductivity of Polymer Electrolytes: One End Functional Group Is Enough. **2013**.

(21) Mohan, P. H.; Bandyopadhyay, R. Phase Behavior and Dynamics of a Micelle-Forming Triblock Copolymer System. *Phys. Rev. E - Stat. Nonlinear, Soft Matter Phys.* **2008**, *77*.

(22) Mezzenga, R.; Meyer, C.; Servais, C.; Romoscanu, A. I.; Sagalowicz, L.; Hayward, R. C. Shear Rheology of Lyotropic Liquid Crystals: A Case Study. *Langmuir* **2005**, *21*, 3322–3333.

(23) Valentine, C. S.; Walker, L. M. Rheological Characterization of BCC and FCC Structures in Aqueous Diblock Copolymer Liquid Crystals. *Korea Aust. Rheol. J.* **2019**, *31*, 249–254.

(24) Mohan, P. H.; Bandyopadhyay, R. Phase Behavior and Dynamics of a Micelle-Forming Triblock Copolymer System. *Phys. Rev. E - Stat. Nonlinear, Soft Matter Phys.* **2008**, *77*.

(25) Eiser, E.; Molino, F.; Porte, G.; Pithon, X. Flow in Micellar Cubic Crystals. In *Rheologica Acta*; 2000; Vol. 39, pp 201–208.

(26) Sinturel, C.; Bates, F. S.; Hillmyer, M. A. High χ–Low *N* Block Polymers: How Far Can We Go? *ACS Macro Lett.* **2015**, *4*, 1044–1050.

(27) Park, M. J.; Char, K.; Bang, J.; Lodge, T. P. Interplay between Cubic and Hexagonal Phases in Block Copolymer Solutions. *Langmuir* **2005**, *21*, 1403–1411.

(28) Bang, J.; Lodge, T. P. Mechanisms and Epitaxial Relationships between Close-Packed and BCC Lattices in Block Copolymer Solutions. *J. Phys. Chem. B* **2003**, *107*, 12071–12081.

(29) Lodge, T. P.; Hanley, K. J.; Pudil, B.; Alahapperuma, V. Phase Behavior of Block Copolymers in a Neutral Solvent. *Macromolecules* **2003**, *36*, 816–822.

(30) Alexandridis, P.; Alan Hatton, T. Poly(Ethylene Oxide)Poly(Propylene Oxide)Poly(Ethylene Oxide) Block Copolymer Surfactants in Aqueous Solutions and at Interfaces: Thermodynamics, Structure, Dynamics, and Modeling. *Colloids Surfaces A Physicochem. Eng. Asp.* **1995**, *96*, 1–46.

(31) Ulbricht, W.; Wanka, G.; Hoffmann, H. *Phase Diagrams and Aggregation Behavior of Poly (Ox Yethy1ene)-Poly (Oxypropylene) -Poly(Oxyet Hylene) Triblock Copolymers in Aqueous Solutions*; 1994; Vol. 27.

(32) Alexandridis, P.; Zhou, D.; Khan, A. *Lyotropic Liquid Crystallinity in Amphiphilic Block Copolymers: Temperature Effects on Phase Behavior and Structure for Poly(Ethylene Oxide)-* b *-Poly(Propylene Oxide)-* b *-Poly(Ethylene Oxide) Copolymers of Different Composition*; 1996; Vol. 12.

(33) Svensson, M.; Alexandridis, P.; Linse, P. Phase Behavior and Microstructure in Binary Block Copolymer/ Selective Solvent Systems: Experiments and Theory. *Macromolecules* **1999**, *32*, 637–645.

(34) Alexandridis, P.; Zhou, D.; Khan, A. Lyotropic Liquid Crystallinity in Amphiphilic Block Copolymers: Temperature Effects on Phase Behavior and Structure for Poly(Ethylene Oxide)-b-Poly(Propylene Oxide)-b-Poly(Ethylene Oxide) Copolymers of Different Composition. *Langmuir* **1996**, *12*, 2690–2700.

(35) Meyrick, G.; Powell, G. W. Phase Transformations in Metals and Alloys. *Annu. Rev. Mater. Sci.* **1973**, *3*, 327–362.

(36) Hamley, I. W. The Effect of Shear on Ordered Block Copolymer Solutions. *Curr. Opin. Colloid Interface Sci.* **2000**, *5*, 341–349.

(37) Butler, P. Shear Induced Structures and Transformations in Complex Fluids. *Curr. Opin. Colloid Interface Sci.* **1999**, *4*, 214–221.

(38) Mezzenga, R.; Meyer, C.; Servais, C.; Romoscanu, A. I.; Sagalowicz, L.; Hayward, R. C. Shear Rheology of Lyotropic Liquid Crystals: A Case Study. *Langmuir* **2005**, *21*, 3322–3333.

(39) Li, L.; Aoki, Y. *Rheological Images of Poly(Vinyl Chloride) Gels. 3. Elasticity Evolution and the Scaling Law beyond the Sol−Gel Transition.Pdf*; 1998.

(40) Mours, M.; Winter, H. H. *Relaxation Patterns of Nearly Critical Gels*; 1996; Vol. 29.

(41) Chambon, F.; Winter, H. H. Linear Viscoelasticity at the Gel Point of a Crosslinking PDMS with Imbalanced Stoichiometry. *J. Rheol.* **1987**, *31*, 683–697.

(42) Martin, J. E.; Adolf, D.; Wilcoxon, J. P. *Viscoelasticity of Near-Critical Gels*; 1988; Vol. 61.

(43) Martin, J. E.; Ado, D. *The Sol-Gel Transition in Ci-Iemical Gels*; 1991; Vol. 42.

(44) Lau, B. K.; Wang, Q.; Sun, W.; Li, L. Micellization to Gelation of a Triblock Copolymer in Water: Thermoreversibility and Scaling. *J. Polym. Sci. Part B Polym. Phys.* **2004**, *42*, 2014–2025.

(45) Park, M. J.; Char, K.; Kim, H. D. *Phase Behavior of a PEO-PPO-PEO Triblock Copolymer*; 2002; Vol. 10.

(46) Dao, M. M.; Domach, M. M.; Walker, L. M. Impact of Dispersed Particles on the Structure and Shear Alignment of Block Copolymer Soft Solids. *J. Rheol.* **2017**, *61*, 237–252.

(47) Pozzo, D. C.; Walker, L. M. Macroscopic Alignment of Nanoparticle Arrays in Soft Crystals of Cubic and Cylindrical Polymer Micelles. *Eur. Phys. J. E* **2008**, *26*, 183–189.

(48) Pozzo, D. C.; Walker, L. M. Three-Dimensional Nanoparticle Arrays Templated by Self-Assembled Block-Copolymer Gels. *Macromol. Symp.* **2005**, *227*, 203–210.

(49) Nyström, B.; Walderhaug, H. *Dynamic Viscoelasticity of an Aqueous System of a Poly(Ethylene Oxide)-Poly(Propylene Oxide)-Poly(Ethylene Oxide) Triblock Copolymer during Gelation*; 1996; Vol. 100.

(50) Faulkner, D. M.; Sutton, S. T.; Hesford, J. D.; Faulkner, B. C.; Major, D. A.; Hellewell, T. B.; Laughon, M. M.; Rodeheaver, G. T.; Edlich, R. F. *A New Stable Pluronic® F68 Gel Carrier for Antibiotics in Contaminated Wound Treatment*; 1997; Vol. 15.

(51) Fakhari, A.; Corcoran, M.; Schwarz, A. Thermogelling Properties of Purified Poloxamer 407. *Heliyon* **2017**, *3*.

(52) Alexandridis, P.; Holzwarth, J. F. *Differential Scanning Calorimetry Investigation of the Effect of Salts on Aqueous Solution Properties of an Amphiphilic Block Copolymer (Poloxamer)*; 1997.

(53) Pandit, N. K.; Kisaka, J. Loss of Gelation Ability of Pluronic® F127 in the Presence of Some Salts. *Int. J. Pharm.* **1996**, *145*, 129–136.

(54) Anderson, B. C.; Cox, S. M.; Ambardekar, A. V.; Mallapragada, S. K. The Effect of Salts on the Micellization Temperature of Aqueous Poly(Ethylene Oxide)-b-Poly(Propylene Oxide)b-Poly(Ethylene Oxide) Solutions and the Dissolution Rate and Water Diffusion Coefficient in Their Corresponding Gels. *J. Pharm. Sci.* **2002**, *91*, 180–188.

(55) Cheng, V. A.; Walker, L. M. Transport of Nanoparticulate Material in Self-Assembled Block Copolymer Micelle Solutions and Crystals. *Faraday Discuss.* **2016**, *186*, 435–454.

(56) Ulbricht, W.; Wanka, G.; Hoffmann, H. *Phase Diagrams and Aggregation Behavior of Poly (Ox Yethy1ene)-Poly (Oxypropylene) -Poly(Oxyet Hylene) Triblock Copolymers in Aqueous Solutions*; 1994; Vol. 27.

(57) Prud'homme, R. K.; Wu, G.; Schneider, D. K. Structure and Rheology Studies of Poly(Oxyethylene−oxypropylene−oxyethylene) Aqueous Solution. *Langmuir* **1996**, *12*, 4651–4659.

(58) Valentine, C. S.; Walker, L. M. Rheological Characterization of BCC and FCC Structures in Aqueous Diblock Copolymer Liquid Crystals. *Rheol. J.* **2019**, *31*, 249–254.

(59) Eiser, E.; Molino, F.; Porte, G. Correlation between the Viscoelastic Properties of a Soft Crystal and Its Microstructure. *Eur. Phys. J. E* **2000**, *2*, 39–46.

(60) Eiser, E.; Molino, F.; Porte, G.; Pithon, X. Flow in Micellar Cubic Crystals. *Rheol. Acta* **2000**, *39*, 201–208.

(61) Speziale, C.; Ghanbari, R.; Mezzenga, R. Rheology of Ultraswollen Bicontinuous Lipidic Cubic Phases. *Langmuir* **2018**, *34*, 5052–5059.

(62) Jones, J. L.; McLeish, T. C. B. Rheological Response of Surfactant Cubic Phases. *Langmuir* **1995**, *11*, 785–792.

(63) Rodríguez-Abreu, C.; García-Roman, M.; Kunieda, H. Rheology and Dynamics of Micellar Cubic Phases and Related Emulsions. *Langmuir* **2004**, *20*, 5235–5240.

(64) May, A.; Aramaki, K.; Gutiérrez, J. M. Phase Behavior and Rheological Analysis of Reverse Liquid Crystals and W/I2and W/H2gel Emulsions Using an Amphiphilic Block Copolymer. *Langmuir* **2011**, *27*, 2286–2298.

(65) Jayaraman, A.; Zhang, D. Y.; Dewing, B. L.; Mahanthappa, M. K. Path-Dependent Preparation of Complex Micelle Packings of a Hydrated Diblock Oligomer. *ACS Cent. Sci.* **2019**, *5*, 619–628.

(66) Balsara, N. P.; Hammouda, B.; Kesani, P. K.; Jonnalagadda, S. V.; Straty, G. C. *In-Situ Small-Angle Neutron Scattering from a Block Copolymer Solution under Shear*; 1994; Vol. 27.

(67) Wang, H.; Kesani, P. K.; Balsara, N. P.; Hammouda, B. *Undulations and Disorder in Block Copolymer Lamellae under Shear Flow*; 1997; Vol. 30.

(68) Zryd, J. L.; Burghardt, W. R. *Steady and Oscillatory Shear Flow Alignment Dynamics in a Lamellar Diblock Copolymer Solution*; 1998; Vol. 31.

(69) Kell, M. *Structural Studies of Aqueous Solutions of PEO - PPO - PEO Triblock Copolymers, Their Micellar Aggregates and Mesophases; a Small-Angle Neutron Scattering Study*; 1996; Vol. 8.

(70) Berni, M. G.; Lawrence, C. J.; Machin, D. *A Review of the Rheology of the Lamellar Phase in Surfactant Systems*; 2002; Vol. 98.

(71) Hamley, I. W. Amphiphilic Diblock Copolymer Gels: The Relationship between Structure and Rheology. *Philos. Trans. R. Soc. A Math. Phys. Eng. Sci.* **2001**, *359*, 1017–1044.

(72) Jiang, J.; Burger, C.; Li, C.; Li, J.; Lin, M. Y.; Colby, R. H.; Rafailovich, M. H.; Sokolov, J. C. Shear-Induced Layered Structure of Polymeric Micelles by SANS. *Macromolecules* **2007**, *40*, 4016–4022.

(73) Castelletto, V.; Hamley, I. W.; Yang, Z. *Flow Mechanisms in the Face-Centred Cubic Micellar Gel of a Diblock Copolymer*; Springer-Verlag, 2001; Vol. 279.

(74) Berret, J. F.; Molino, F.; Porte, G.; Diat, O.; Lindner, P. *The Shear-Induced Transition between Oriented Textures and Layer-Sliding-Mediated Flows in*

a Micellar Cubic Crystal; 1996; Vol. 8.

(75) Diat, O.; Porte, G.; Berret, J. F. *Orientation and Twins Separation in a Micellar Cubic Crystal under Oscillating Shear*; 1996; Vol. 54.

(76) Eiser, E.; Molino, F.; Porte, G. *Correlation between the Viscoelastic Properties of a Soft Crystal and Its Microstructure*; 2000; Vol. 2.

(77) McConnell, G. A.; Lin, M. Y.; Gast, A. P. *Long Range Order in Polymeric Micelles under Steady Shear*; 1995; Vol. 28.

(78) Eiser, E.; Molino, F.; Porte, G.; Diat, O. Nonhomogeneous Textures and Banded Flow in a Soft Cubic Phase under Shear. *Phys. Rev. E - Stat. Physics, Plasmas, Fluids, Relat. Interdiscip. Top.* **2000**, *61*, 6759–6764.

(79) Hamley, I. W.; Pople, J. A.; Booth, C.; Yang, Y. W.; King, S. M. *Small-Angle Neutron-Scattering Study of Shear-Induced Ordering in the Cubic Phase of a Block Copolymer Gel*; 1998; Vol. 14.

(80) Hamley, I. W.; Pople, J. A.; Booth, C.; Derici, L.; Impéror-Clerc, M.; Davidson, P. *Shear-Induced Orientation of the Body-Centered-Cubic Phase in a Diblock Copolymer Gel*; 1998; Vol. 58.

(81) Torija, M. A.; Choi, S.-H.; Lodge, T. P.; Bates, F. S. Large Amplitude Oscillatory Shear of Block Copolymer Spheres on a Body-Centered Cubic Lattice: Are Micelles Like Metals? *J. Phys. Chem. B* **2011**, *115*, 5840–5848.

(82) Daniel, C.; Hamley, I. W.; Wilhelm, M.; Mingvanish, W. *Non-Linear Rheology of a Face-Centred Cubic Phase in a Diblock Copolymer Gel*; Springer-Verlag, 2001; Vol. 40.

(83) Pople, J. A.; Hamley, I. W.; Terrill, N. J.; Fairclough, J. P. A.; Ryant, A. J.; Yu, G. E.; Booth, C. Shear-Induced Orientational Order in the Hexagonal Phase of Oxyethylene/Oxybutylene Diblock Copolymer Gels. *Polymer (Guildf).* **1998**, *39*, 4891–4896.

(84) Hamley, I. W.; Pople, J. A.; Fairclough, J. P. A.; Ryan, A. J.; Booth, C.; Yang, Y. W. Shear-Induced Orientational Transitions in the Body-Centered Cubic Phase of a Diblock Copolymer Gel. *Macromolecules* **1998**, *31*, 3906–3911.

(85) Pople, J. A.; Hamley, I. W.; Fairclough, J. P. A.; Ryan, A. J.; Booth, C. Orientational Ordering of a Poly(Oxyethylene)-Poly(Oxybutylene) Diblock Copolymer Gel under Steady Shear Flow. *Macromolecules* **1998**, *31*, 2952–2956.

(86) Balogh, L.; Ribárik, G.; Ungár, T. Stacking Faults and Twin Boundaries in Fcc Crystals Determined by X-Ray Diffraction Profile Analysis. *J. Appl. Phys.* **2006**, *100*, 23512.

(87) Watanabe, H.; Kanaya, T.; Takahashi, Y. Equilibrium Elasticity of Diblock Copolymer Micellar Lattice. *Macromolecules* **2001**, *34*, 662–665.

(88) Divoux, T.; Fardin, M. A.; Manneville, S.; Lerouge, S. Shear Banding of Complex Fluids. *Annu. Rev. Fluid Mech* **2015**, *48*, 81–103.

(89) Holmqvist, P.; Daniel, C.; Hamley, I. W.; Mingvanish, W.; Booth, C.

Inhomogeneous Flow in a Micellar Solution of a Diblock Copolymer: Creep Rheometry Experiments; 2002; Vol. 196.

(90) Manneville, S. Recent Experimental Probes of Shear Banding. *Rheol. Acta* **2008**, *47*, 301–318.

(91) Mezzenga, R.; Seddon, J. M.; Drummond, C. J.; Boyd, B. J.; Schröder-Turk, G. E.; Sagalowicz, L. Nature-Inspired Design and Application of Lipidic Lyotropic Liquid Crystals. *Adv. Mater.* **2019**, *31*, 1–19.

(92) Hyde, S. T. Identification of Lyotropic Liquid Crystalline Mesophases. In *Handbook of Applied Surface and Colloid Chemistry*; Holmberg, K., Shah, D. O., Schwuger, M. J., Eds.; John Wiley & Sons, Ltd: West Sussex, 2002; Vol. 3, pp 299–327.

(93) Shearman, G. C.; Tyler, A. I. I.; Brooks, N. J.; Templer, R. H.; Ces, O.; Law, R. V.; Seddon, J. M. Ordered Micellar and Inverse Micellar Lyotropic Phases. *Liq. Cryst.* **2010**, *37*, 679–694.

(94) McConnell, G. A.; Gast, A. P.; Huang, J. S.; Smith, S. D. Disorder-Order Transitions in Soft Sphere Polymer Micelles. *Phys. Rev. Lett.* **1993**, *71*, 2102–2105.

(95) Hamley, I. W.; Pople, J. A.; Diat, O. A Thermally Induced Transition from a Body-Centred to a Face-Centred Cubic Lattice in a Diblock Copolymer Gel. *Colloid Polym. Sci.* **1998**, *276*, 446–450.

(96) Lodge, T. P.; Bang, J.; Park, M. J.; Char, K. Origin of the Thermoreversible Fcc-Bcc Transition in Block Copolymer Solutions. *Phys. Rev. Lett.* **2004**, *92*.

(97) Sakya, P.; Seddon, J. M.; Templer, R. H.; Mirkin, R. J.; Tiddy, G. J. T. Micellar Cubic Phases and Their Structural Relationships: The Nonionic Surfactant System C 12 EO 12 /Water . *Langmuir* **2002**, *13*, 3706–3714.

(98) Kim, S. A.; Jeong, K.-J.; Yethiraj, A.; Mahanthappa, M. K. Low-Symmetry Sphere Packings of Simple Surfactant Micelles Induced by Ionic Sphericity. *Proc. Natl. Acad. Sci.* **2017**, *114*, 4072–4077.

(99) Jayaraman, A.; Mahanthappa, M. K. Counterion-Dependent Access to Low-Symmetry Lyotropic Sphere Packings of Ionic Surfactant Micelles. *Langmuir* **2018**, *34*, 2290–2301.

(100) Perroni, D. V.; Mahanthappa, M. K. Inverse Pm3n Cubic Micellar Lyotropic Phases from Zwitterionic Triazolium Gemini Surfactants. *Soft Matter* **2013**, *9*, 7919–7922.

(101) Baez-Cotto, C. M.; Mahanthappa, M. K. Micellar Mimicry of Intermetallic C14 and C15 Laves Phases by Aqueous Lyotropic Self-Assembly Article. *ACS Nano* **2018**, *12*, 3234.

(102) Yue, K.; Huang, M.; Marson, R. L.; He, J.; Huang, J.; Zhou, Z.; Wang, J.; Liu, C.; Yan, X.; Wu, K.; Guo, Z.; Liu, H.; Zhang, W.; Ni, P.; Wesdemiotis, C.; Zhang, W.-B.; Glotzer, S. C.; Cheng, S. Z. D. Geometry Induced Sequence of Nanoscale Frank–Kasper and Quasicrystal Mesophases in Giant Surfactants. *Proc. Natl. Acad. Sci.* **2016**, *113*, 14195–14200.

(103) Lachmayr, K. K.; Wentz, C. M.; Sita, L. R. An Exceptionally Stable and Scalable Sugar–Polyolefin Frank–Kasper A15 Phase. *Angew. Chemie - Int. Ed.* **2020**, *59*, 1521–1526.

(104) Lindsay, A. P.; Lewis, R. M.; Lee, B.; Peterson, A. J.; Lodge, T. P.; Bates, F. S. A15, σ, and a Quasicrystal: Access to Complex Particle Packings via Bidisperse Diblock Copolymer Blends. *ACS Macro Lett.* **2020**, 197–203.

(105) Mueller, A. J.; Lindsay, A. P.; Jayaraman, A.; Lodge, T. P.; Mahanthappa, M. K.; Bates, F. S. Emergence of a C15 Laves Phase in Diblock Polymer/Homopolymer Blends. *ACS Macro Lett.* **2020**, *9*, 576–582.

(106) Kim, K.; Schulze, M. W.; Arora, A.; Lewis Iii, R. M.; Hillmyer, M. A.; Dorfman, K. D.; Bates, F. S. Thermal Processing of Diblock Copolymer Melts Mimics Metallurgy. *Science.* **2017**, *356*, 520–523.

(107) Bates, M. W.; Lequieu, J.; Barbon, S. M.; Lewis, R. M.; Delaney, K. T.; Anastasaki, A.; Hawker, C. J.; Fredrickson, G. H.; Bates, C. M. Stability of the A15 Phase in Diblock Copolymer Melts. *Proc. Natl. Acad. Sci.* **2019**, *116*, 13194–13199.

(108) Lee, S.; Leighton, C.; Bates, F. S. Sphericity and Symmetry Breaking in the Formation of Frank-Kasper Phases from One Component Materials. *Proc. Natl. Acad. Sci.* **2014**, *111*, 17723–17731.

(109) Rappolt, M.; Cacho-Nerin, F.; Morello, C.; Yaghmur, A. How the Chain Configuration Governs the Packing of Inverted Micelles in the Cubic Fd3m-Phase. *Soft Matter* **2013**, *9*, 6291–6300.

(110) McConnell, G. A.; Lin, M. Y.; Gast, A. P. Long Range Order in Polymeric Micelles under Steady Shear. *Macromolecules* **1995**, *28*, 6754–6764.

(111) Lee, H. H.; Jeong, W.-Y.; Kim, J. K.; Ihn, K. J.; Kornfield, J. A.; Wang, Z.-G.; Qi, S. Orientational Proliferation and Successive Twinning from Thermoreversible Hexagonal−Body-Centered Cubic Transitions. *Macromolecules* **2002**, *35*, 785–794.

(112) Wang, S.; Xie, R.; Vajjala Kesava, S.; Gomez, E. D.; Cochran, E. W.; Robertson, M. L. Close-Packed Spherical Morphology in an ABA Triblock Copolymer Aligned with Large-Amplitude Oscillatory Shear. *Macromolecules* **2016**, *49*, 4875–4888.

(113) López-Barrón, C. R.; Wagner, N. J.; Porcar, L. Layering, Melting, and Recrystallization of a Close-Packed Micellar Crystal under Steady and Large-Amplitude Oscillatory Shear Flows. *J. Rheol.* **2015**, *59*, 793–820.

(114) Koppi, K. A.; Tirrell, M.; Bates, F. S.; Almdal, K.; Colby, R. H. Lamellae Orientation in Dynamically Sheared Diblock Copolymer Melts. *J. Phys. II Fr.* **1992**, *2*, 1941–1959.

(115) Schulz, M. F.; Bates, F. S.; Almdal, K.; Mortensen, K. Epitaxial Relationship for Hexagonal-to-Cubic Phase Transition in a Block Copolymer Mixture. *Phys. Rev. Lett.* **1994**, *73*, 86–89.

(116) Koppi, K. A.; Tirrell, M.; Bates, F. S.; Almdal, K.; Mortensen, K. Epitaxial

Growth and Shearing of the Body Centered Cubic Phase in Diblock Copolymer Melts. *J. Rheol.* **1994**, *38*, 999–1027.

(117) Pozzo, D. C.; Walker, L. M. Shear Orientation of Nanoparticle Arrays Templated in a Thermoreversible Block Copolymer Micellar Crystal. *Macromolecules* **2007**, *40*, 5801–5811.

(118) Okamoto, S.; Saijo, K.; Hashimoto, T. Dynamic SAXS Studies of Sphere-Forming Block Copolymers under Large Oscillatory Shear Deformation. *Macromolecules* **1994**, *27*, 3753–3758.

(119) Bang, J.; Lodge, T. P.; Wang, X.; Brinker, K. L.; Burghardt, W. R. Thermoreversible, Epitaxial Fcc <-> Bcc Transitions in Block Copolymer Solutions. *Phys. Rev. Lett.* **2002**, *89*, 215505.

(120) Zana, R. *Dynamics of Surfactant Self-Assembleys: Micelles, Microemulsions, Vesicles and Lyotropic Phases*, 1st ed.; Zana, R., Ed.; CRC Press: Boca Raton, 2005.

(121) Phoon, C. L.; Higgins, J. S.; Allegra, G.; Van Leeuwen, P.; Staples, E. Shear Induced Crystallization and Melting of a Micellar Solution. *Proc. R. Soc. London. Ser. A Math. Phys. Sci.* **1993**, *442*, 221–230.

(122) Fischer, S.; Exner, A.; Zielske, K.; Perlich, J.; Deloudi, S.; Steurer, W.; Lindner, P.; Förster, S. Colloidal Quasicrystals with 12-Fold and 18-Fold Diffraction Symmetry. *Proc. Natl. Acad. Sci.* **2011**, *108*, 1810–1814.

(123) Liu, Y.; Nie, H.; Bansil, R.; Steinhart, M.; Bang, J.; Lodge, T. P. Kinetics of Disorder-to-Fcc Phase Transition via an Intermediate Bcc State. *Phys. Rev. E - Stat. Nonlinear, Soft Matter Phys.* **2006**, *73*, 1–6.

(124) Avrami, M. Kinetics of Phase Change. I General Theory. *J. Chem. Phys.* **1939**, *7*, 1103–1112.

(125) Avrami, M. Kinetics of Phase Change. II Transformation-Time Relations for Random Distribution of Nuclei. *J. Chem. Phys.* **1940**, *8*, 212–224.

(126) Avrami, M. Granulation, Phase Change, and Microstructure Kinetics of Phase Change. III. *J. Chem. Phys.* **1941**, *9*, 177–184.

(127) DeGraef, M.; McHenry, M. *Structure of Materials: An Introduction to Crystallography, Diffraction, and Symmetry*, 2nd ed.; Cambridge University Press: Cambridge, 2012.

(128) Kim, K.; Arora, A.; Lewis, R. M.; Liu, M.; Li, W.; Shi, A.-C.; Dorfman, K. D.; Bates, F. S. Origins of Low-Symmetry Phases in Asymmetric Diblock Copolymer Melts. *Proc. Natl. Acad. Sci.* **2018**, *115*, 847–854.

(129) Ziherl, P.; Kamien, R. D. Soap Froths and Crystal Structures. *Phys. Rev. Lett.* **2000**, *85*, 3528–3531.

(130) Reddy, A.; Buckley, M. B.; Arora, A.; Bates, F. S.; Dorfman, K. D.; Grason, G. M. Stable Frank-Kasper Phases of Self-Assembled, Soft Matter Spheres. *Proc. Natl. Acad. Sci.* **2018**, *115*, 10233–10238.

(131) Callister, W. D.; Rethwisch, D. G. *Materials Science and Engineering: An*

Introduction, 8th ed.; John Wiley & Sons NY, 2011.

(132) Wright, R. N.; Bok, K. A. A15 Compound Deformation and Secondary Slip in V3Si. *Metall. Trans. A, Phys. Metall. Mater. Sci.* **1988**, *19 A*, 1125–1127.

(133) Xuan, J. J.; Balakrishnan, P.; Oh, D. H.; Yeo, W. H.; Park, S. M.; Yong, C. S.; Choi, H. G. Rheological Characterization and in Vivo Evaluation of Thermosensitive Poloxamer-Based Hydrogel for Intramuscular Injection of Piroxicam. *Int. J. Pharm.* **2010**, *395*, 317–323.

(134) Zhang, K.; Shi, X.; Lin, X.; Yao, C.; Shen, L.; Feng, Y. Drug Delivery Poloxamer-Based in Situ Hydrogels for Controlled Delivery of Hydrophilic Macromolecules after Intramuscular Injection in Rats Poloxamer-Based in Situ Hydrogels for Controlled Delivery of Hydrophilic Macromolecules after Intramuscular Injecti. *Drug Deliv* **2015**, *22*, 375–382.

(135) Giuliano, E.; Paolino, D.; Fresta, M.; Cosco, D. Mucosal Applications of Poloxamer 407-Based Hydrogels: An Overview. *Pharmaceutics* **2018**, *10*, 1–26.

(136) Pozzo, D. C.; Walker, L. M. Macroscopic Alignment of Nanoparticle Arrays in Soft Crystals of Cubic and Cylindrical Polymer Micelles. *Eur. Phys. J. E* **2008**, *26*, 183–189.

(137) Sarkar, B.; Alexandridis, P. Block Copolymer-Nanoparticle Composites: Structure, Functional Properties, and Processing. *Prog. Polym. Sci.* **2015**, *40*, 33–62.

(138) Sajid, M.; Akash, H.; Rehman, K.; Li, N.; Gao, & J.-Q.; Sun, H.; Chen, S. Sustained Delivery of IL-1Ra from Pluronic F127-Based Thermosensitive Gel Prolongs Its Therapeutic Potentials.

(139) Anderson, B. C.; Pandit, N. K.; Mallapragada, S. K. Understanding Drug Release from Poly(Ethylene Oxide)-b-Poly(Propylene Oxide)-b-Poly(Ethylene Oxide) Gels. *J. Control. Release* **2001**, *70*, 157–167.

(140) Sun, W.; Vallooran, J. J.; Mezzenga, R. Enzyme Kinetics in Liquid Crystalline Mesophases: Size Matters, but Also Topology. *Langmuir* **2015**, *31*, 4558–4565.

(141) Eggers, D. K. Molecular Confinement Influences Protein Structure and Enhances Thermal Protein Stability. *Protein Sci.* **2001**, *10*, 250–261.

(142) Menaa, B.; Herrero, M.; Rives, V.; Lavrenko, M.; Eggers, D. K. Favourable Influence of Hydrophobic Surfaces on Protein Structure in Porous Organically-Modified Silica Glasses. *Biomaterials* **2008**, *29*, 2710–2718.

(143) Zhou, H.-X.; Rivas, G.; Minton, A. P. Macromolecular Crowding and Confinement: Biochemical, Biophysical, and Potential Physiological Consequences. *Annu. Rev. Biophys.* **2008**, *37*, 375–397.

(144) Zhou, H. X.; Dill, K. A. Stabilization of Proteins in Confined Spaces. *Biochemistry* **2001**, *40*, 11289–11293.

(145) Ping, G.; Yuan, J. M.; Sun, Z.; Wei, Y. Studies of Effects of Macromolecular Crowding and Confinement on Protein Folding and Protein Stability. *J. Mol.*

Recognit. **2004**, *17*, 433–440.

(146) Ellis, R. J. Macromolecular Crowding: Obvious but Underappreciated. *Trends in Biochemical Sciences*. 2001, pp 597–604.

(147) Domach, M. M.; Walker, L. M. Stabilizing Biomacromolecules in Nontoxic Nano-Structured Materials. *JALA - J. Assoc. Lab. Autom.* **2010**, *15*, 136–144.

(148) Pozzo, D. C.; Walker, L. M. Small-Angle Neutron Scattering of Silica Nanoparticles Templated in PEO-PPO-PEO Cubic Crystals. *Colloids Surfaces A Physicochem. Eng. Asp.* **2007**, *294*, 117–129.

(149) Yang, L.; Alexandridis, P.; Steytler, D. C.; Kositza, M. J.; Holzwarth, J. F. Small-Angle Neutron Scattering Investigation of the Temperature-Dependent Aggregation Behavior of the Block Copolymer Pluronic L64 in Aqueous Solution. *Langmuir* **2000**, *16*, 8555–8561.

(150) Thurn, T.; Couderc, S.; Sidhu, J.; Bloor, D. M.; Penfold, J.; Holzwarth, J. F.; Wyn-Jones, E. Study of Mixed Micelles and Interaction Parameters for ABA Triblock Copolymers of the Type EOm−POn−EOm and Ionic Surfactants: Equilibrium and Structure. *Langmuir* **2002**, *18*, 9267–9275.

(151) Pozzo, D. C.; Walker, L. M. Shear Orientation of Nanoparticle Arrays Templated in a Thermoreversible Block Copolymer Micellar Crystal. *Macromolecules* **2007**, *40*, 5801–5811.

(152) Park, H. J.; Treich, G. M.; Helming, Z. D.; Morgan, J. E.; Ryu, C. Y.; Hwang, H. S.; Jung, G. Y. Micellar Packing of Pluronic Block Copolymer Solutions: Polymeric Impurity Effects. *Macromol. Res.* **2015**, *23*, 13–20.

(153) Bedrov, D.; Ayyagari, C.; Smith, G. D. Multiscale Modeling of Poly(Ethylene Oxide)-Poly(Propylene Oxide)-Poly(Ethylene Oxide) Triblock Copolymer Micelles in Aqueous Solution. *J. Chem. Theory Comput.* **2006**, *2*, 598–606.

(154) The, T. H.; Feltkamp, T. E. W. Conjugation of Fluorescein Isothiocyanate to Antibodies. *Immunology* **1970**, *18*, 875–881.

(155) The, T. H.; Feltkamp, T. E. Conjugation of Fluorescein Isothiocyanate to Antibodies. II. A Reproducible Method. *Immunology* **1970**, *18*, 875–881.

(156) Barbero, N.; Barolo, C.; Viscardi, G. Bovine Serum Albumin Bioconjugation with FITC. *World J. Chem. Educ. Vol. 4, 2016, Pages 80-85* **2016**, *4*, 80–85.

(157) Edelstein, A. D.; Tsuchida, M. A.; Amodaj, N.; Pinkard, H.; Vale, R. D.; Stuurman, N. Advanced Methods of Microscope Control Using MManager Software. *J. Biol. Methods* **2014**, *1*, e10.

(158) Edelstein, A.; Amodaj, N.; Hoover, K.; Vale, R.; Stuurman, N. Computer Control of Microscopes Using Manager. *Curr. Protoc. Mol. Biol.* **2010**, No. SUPPL. 92.

(159) Balluffi, R. W.; Allen, S. M.; Carter, W. C. Kinetics of Materials. In *Kinetics of Materials*; 2005; pp 1–645.

(160) Halperin, A.; Tirrell, M.; Lodge, T. P. *Tethered Chains in Polymer Microstructures. In: Macromolecules: Synthesis, Order and Advanced Properties. Advances in Polymer Science, Vol 100/1*; Springer, Berlin, Heidelberg, 1992.

(161) Rubinstein, M.; Colby, R. H. *Polymer Physics*; Oxford University Press, 2003.

(162) Sumant, O.; Shaikh, S. *Protein Therapeutics Market by Product and Application - Global Opportunity Analysis and Industry Forecast, 2017-2023*; 2017.

(163) Ellis, R. J.; Minton, A. P. Protein Aggregation in Crowded Environments. *Biol. Chem* **2006**, *387*, 485–497.

(164) Mach, H.; Volkin, D. B.; Burke, C. J.; Middaugh, C. R. Protein Stability and Folding. Methods in Molecular Biology. In *Methods in molecular biology (Clifton, N.J.)*; Humana Press, 1995; Vol. 40, pp 91–114.

(165) Poklar, N.; Vesnaver, G. Thermal Denaturation of Proteins Studied by UV Spectroscopy. *J. Chem. Educ.* **2000**, *77*, 380–382.

(166) Pinho Melo, E.; Aires-Barros, M. R.; Costa, S. M. B.; Cabral, J. M. S. Thermal Unfolding of Proteins at High PH Range Studied by UV Absorbance. *J. Biochem. Biophys. Methods* **1997**, *34*, 45–59.

(167) Rezaei-Tavirani, M.; Moghaddamnia, S. H.; Ranjbar, B.; Amani, M.; Marashi, S. A. Conformational Study of Human Serum Albumin in Pre-Denaturation Temperatures by Differential Scanning Calorimetry, Circular Dichroism and UV Spectroscopy. *J. Biochem. Mol. Biol.* **2006**, *39*, 530–536.

(168) Wetlaufer, D. B. Ultraviolet Spectra Of Proteins and Amino Acids. *Adv. Protein Chem.* **1963**, *17*, 303–390.

(169) Glazer, A. N.; McKenzie, H. A.; Wake, R. G. The Denaturation of Proteins. II. Ultraviolet Absorption Spectra of Bovine Serum Albumin and Ovalbumin in Urea and in Acid Solution. *BBA - Biochim. Biophys. Acta* **1963**, *69*, 240–248.

(170) Takeda, K.; Wada, A.; Yamamoto, K.; Moriyama, Y.; Aoki, K. Conformational Change of Bovine Serum Albumin by Heat Treatment. *J. Protein Chem.* **1989**, *8*, 653–659.